Doctoral thesis

Natural Locomotion Families

Reduced recurrence, mechanical exchange, and resonantly maintained motion in constrained locomotors

Mirado Mortel

Thesis director:	Luc Jaulin
Co-supervisors:	Lionel Lapierre and Simon Rohou
Institution:	[official institution]
Doctoral school:	[official doctoral school]
Discipline:	[official discipline]
Defence date:	[date]

Résumé

Cette thèse cherche quels mouvements répétables un locomoteur articulé peut produire à partir de sa propre dynamique, avant de lui prescrire une trajectoire articulaire complète. Pour des modèles plans non holonomes, la pose du corps est séparée de l'état mécanique réduit. Un cycle de locomotion naturelle est ici une solution non triviale des équations conservatives non forcées dont l'état réduit revient exactement, tandis que la pose reconstruite peut accumuler un déplacement non nul. Le terme *naturel* désigne donc la compatibilité avec le champ mécanique déclaré; il n'implique ni stabilité, ni optimalité. Les modes linéaires ne fournissent que des germes locaux. La correction et la continuation laissent la fréquence, la forme d'onde et les relations de phase évoluer avec l'amplitude.

Le modèle à deux segments rend la construction explicite depuis un mouvement rectiligne jusqu'à des cycles relatifs d'amplitude finie. Une comparaison dans $\mathrm{SE}(2)$ montre que ces cycles modulent généralement une dérive rectiligne dominante, plutôt qu'ils ne créent à eux seuls toute la translation. Le résultat analytique principal provient ensuite d'une décomposition entre champ fermé et champ ouvert du canal porteur. L'élimination des vitesses du porteur définit un champ transverse conservatif auxiliaire; lorsque le couplage original est rétabli, la puissance d'échange est exactement la dérivée du stockage transverse. Sur une section scalaire orientée où ce stockage est injectif, et après fermeture des autres coordonnées, l'échange intégré nul équivaut au retour de la dernière vitesse de section. Avec trois segments, une seule valeur de stockage ne détermine plus le point final: le retour vectoriel complet reste nécessaire, puis des mesures modales classent séparément des familles mobiles en phase et en opposition de phase.

En présence de pertes, le travail injecté doit compenser la dissipation sur chaque cycle. Une homotopie conservant la même mécanique relie numériquement un cycle conservatif à une branche locale de réponses synchronisées maintenues. Une archive distincte, calculée pour un autre vecteur de paramètres, forme une carte de locomotion résonante présentant plis, coexistence et changements de forme d'onde. Le bilan travail–pertes y est exact pour toute réponse périodique; la quadrature n'est qu'un repère local sur une partie du domaine échantillonné. Enfin, une boucle de phase rapide et une régulation plus lente de la vitesse moyenne parcourent localement cette carte. L'ensemble fournit ainsi une chaîne explicite allant de la qualification de cycles conservatifs à l'accompagnement local de réponses dissipatives, avec des frontières distinctes entre théorème, construction numérique et démonstration de commande.

Mots-clés. locomotion mécanique; dynamique non linéaire; orbite périodique relative; modes non linéaires; contraintes non holonomes; réponse forcée; résonance; boucle à verrouillage de phase.

Abstract

This thesis asks which repeatable motions an articulated locomotor can generate from its own dynamics before a complete joint trajectory is prescribed. For planar nonholonomic models, body pose is separated from the reduced mechanical state. A natural-locomotion cycle is defined here as a nontrivial solution of the unforced conservative equations whose reduced state returns exactly while the reconstructed pose may accumulate a nonidentity displacement. *Natural* therefore means compatibility with the declared mechanical field; it implies neither stability nor optimality. Linear modes provide only local seeds. Correction and continuation allow frequency, waveform, and phase relations to change with amplitude.

The two-segment model makes the construction explicit from straight motion to finite-amplitude relative cycles. A matched comparison in $\mathrm{SE}(2)$ shows that these cycles usually modulate a dominant straight drift rather than generate all translation by themselves. The main analytical result then follows from a carrier closed–open decomposition. Eliminating the carrier velocities defines an auxiliary conservative transverse field; when the original coupling is restored, exchange power is exactly the derivative of transverse storage. On an oriented scalar section where that storage is injective, and after the other coordinates have returned, zero integrated exchange is equivalent to return of the remaining crossing speed. With three segments, one storage value no longer determines the endpoint: full vector return remains necessary, after which modal metrics separately classify moving in-phase and anti-phase families.

With losses, input work must replace dissipation over every cycle. A same-mechanics homotopy numerically connects one conservative cycle to a local branch of synchronized maintained responses. A separate archive, computed for a different parameter vector, forms a Resonant Locomotion Map with folds, coexisting responses, and waveform changes. Work–loss balance is exact for every periodic response; quadrature is only a local marker on part of the sampled domain. Finally, a fast phase loop and slower mean-speed regulation navigate this map locally. The thesis thus provides an explicit chain from the qualification of conservative cycles to the local accompaniment of dissipative responses, while keeping theorem, numerical construction, and control demonstration at distinct evidence levels.

Keywords. mechanical locomotion; nonlinear dynamics; relative periodic orbit; nonlinear modes; nonholonomic constraints; forced response; resonance; phase-locked loop.

Contents

Notation at a glance

The same symbols recur across several mechanical models. This page gives the minimum vocabulary needed to enter the argument; model-specific coefficients are defined where they first appear.

Symbol or term	Meaning
$g = (x, y, \theta) \in \mathrm{SE}(2)$	planar body pose; it may drift over a reduced cycle
δ or $\boldsymbol{\delta}$	one joint angle, or the vector of internal joint angles
v, ω, σ	body-forward speed, body yaw rate, and joint rate
$\bar{v}$	cycle-mean body-forward speed
Δg	pose increment reconstructed after one returned reduced cycle
Δg_{inc}	matched-straight residual transform, not a causal decomposition
Σ	oriented Poincaré section used to remove time shift
$E_{\perp}$	transverse mechanical storage exposed by closing the carrier channel
$P_{\mathrm{ex}}, I_{\mathrm{ex}}$	exchange power and its integral along a cycle
AP / IP	anti-phase / in-phase organization of the two internal joints
$A_{\mathrm{exc}}, T_{\mathrm{exc}}$	forcing amplitude and forcing period
$\phi_{\delta\tau}$	phase of joint deformation relative to applied joint torque
PLL	phase-locked loop used for local traversal of a computed response family
NLM	historical name of the natural-locomotion programme; results are families or branches
RLM	Resonant Locomotion Map: observable image of period-matched forced responses

2SEG and 3SEG denote the two- and three-segment models. "Returned" always refers to the reduced mechanical state; locomotion additionally requires $\Delta g \neq e_G$. The chapters state the parameter domain and regularity supported for each conservative family or RLM chart.

Part I

Understanding the object

Chapter 1

Natural locomotion as a family-selection problem

A controller can make a mechanical system follow many feasible joint trajectories. This is useful when the desired choreography is already known. It leaves a prior question unanswered: before prescribing that choreography, which repeatable motions are organized by the mechanism's own dynamics?

This thesis studies that question for planar articulated locomotors. The aim is not to identify one privileged sinusoid. It is to construct families of motions whose frequency, waveform, and coordination are allowed to vary with their mechanical state. In the conservative models, each member must solve the unforced equations, return to the same reduced mechanical state, and accumulate a declared pose increment. In the dissipative model, periodic forcing replaces the energy lost over a cycle, and feedback regulates a small number of observable family coordinates instead of prescribing every harmonic.

The central difficulty is that several established theories answer different parts of this question. Linear modes describe infinitesimal oscillations. Nonlinear modes organize finite-amplitude periodic motions. Symmetry reduction and reconstruction separate repeatable internal dynamics from body transport. Shooting and continuation compute cycles and follow them through parameter space. Forced-response analysis and phase-locked loops maintain and navigate responses in the presence of losses. The thesis connects these roles without treating any one of them as the complete answer.

1.1 Four insufficiencies that determine the object

The object studied here can be reached through four successive observations. Each observation keeps a useful classical idea and identifies the additional information required by locomotion.

A linear mode is not a finite-amplitude choreography. Near an equilibrium, a linear eigenvector gives a direction and its eigenvalue gives a natural frequency. At finite amplitude, however, nonlinear forces can change the frequency, bend the trajectory, alter phase relations between coordinates, and generate harmonics. A fixed sinusoidal template therefore cannot represent a whole natural family. Nonlinear modal families provide the appropriate finite-amplitude organization, but they do not yet distinguish oscillation from locomotion.

Full-state periodicity closes the very directions needed for transport. For an ordinary oscillator, returning the full configuration and velocity after one period is the natural event. A locomotor must instead repeat its internal mechanical event while allowing its position and orientation to change. If the full pose also returned, the net rigid-body displacement would be the identity by definition. The relevant object is therefore a *relative-periodic* motion: reduced state closes; pose remains open.

A transporting loop is not necessarily a natural motion. Geometric reconstruction can determine the body displacement produced by a given internal loop. Infinitely many loops may produce translation or rotation. Reconstruction is conditional: it does not establish that the loop, with its timing and velocities, solves the unforced mechanical equations. The candidate studied here is a time-parameterized trajectory in reduced state, not only a curve drawn in joint space.

Conservative recurrence does not survive losses without input. An exact conservative cycle can repeat without maintained work if the system is initialized exactly on it. Damping makes free oscillations decay. A periodic response of a dissipative mechanism must instead receive, over one cycle, the work dissipated over that cycle. This changes both the field and the return problem. One numerical homotopy below follows a single two-segment cycle while damping and synchronized forcing are introduced without changing its mechanics. It is a local bridge, not persistence of the whole conservative family. The larger forced-response archive uses a parameter-distinct model and remains a related response study rather than a continuation of that family.

These four observations give the narrative in one sentence: replace a fixed choreography by a dynamically generated oscillatory family; close the reduced state rather than the pose; require the timed trajectory to solve the stated field; and, when losses are present, maintain and navigate the resulting forced responses through a few measured coordinates.

1.2 The object studied in the conservative models

Let the configuration split into planar pose and internal shape,

$$q = (g, r), \qquad g \in \mathrm{SE}(2), \tag{1.1}$$

and let z denote the reduced mechanical state. Besides shape, z contains the rates and admissible carrier velocities needed to determine the motion. Pose symmetry removes absolute position and orientation from the reduced field,

$$\dot{z} = f(z), \qquad \dot{g} = g\,\xi(z), \tag{1.2}$$

where the second equation reconstructs pose from the reduced solution. For the planar models used below, it is equivalent to integrating body-forward speed and yaw rate.

A conservative natural-locomotion cycle is the following mathematical target:

$$\dot{z} = f_{\mathrm{cons}}(z), \qquad z(T) = z(0), \qquad \Delta g = g(0)^{-1}g(T) \neq e. \tag{1.3}$$

The reduced orbit is required to be nontrivial, under a stated phase or minimal-period convention. A straight relative equilibrium, for which z is constant while the body drifts, is a seed or boundary of the families rather than a periodic orbit manufactured by choosing an arbitrary value of T. The word *natural* means only that the nontrivial cycle is an exact solution of the stated unforced conservative equations. It does not imply attraction, stability, optimality, robustness, or biological inevitability.

Equation (1.3) also separates two outputs that must not be conflated. A nonidentity Δg establishes a moving relative-periodic solution. It does not, by itself, establish that internal oscillation generated the observed translation: part of the displacement may be the drift of the matched straight relative equilibrium. Any claim about an oscillation-induced increment therefore requires an explicit group-level or body-frame comparison with that reference motion.

It is useful to separate *qualification* from *organization.* A candidate qualifies when it solves the specified field, has a nontrivial exact reduced return, and produces the declared locomotor output.

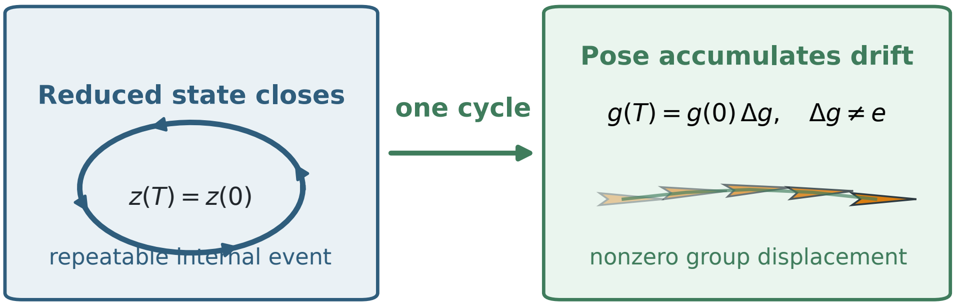

Figure 1.1: The repeatable locomotor event. The reduced state includes the internal coordinates, their rates, and the required carrier velocities; it returns after one cycle. Pose reconstruction remains open and accumulates a group displacement. This picture states the return structure, not stability or the dynamical origin of the displacement.

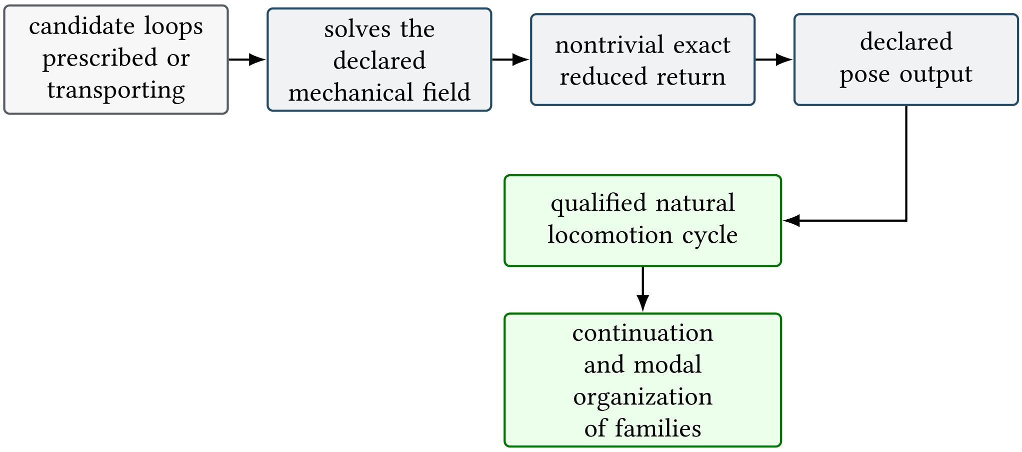

Figure 1.2: Reconstruction or prescription can supply many candidate loops; the conservative field, exact reduced return, and the declared pose output filter them before continuation or modal organization. In the scalar two-segment theorem, integrated exchange replaces one return row only after the other return rows and section hypotheses have been imposed.

Continuation then places qualified cycles on connected branches, while modal metrics can classify their internal coordination. These latter operations reveal the structure of a family; they are not additional conditions of naturality.

The historical name *Natural Locomotion Manifold* (NLM) refers in this thesis to the overall programme. The results themselves are called families or continuation branches unless a manifold structure is explicitly defined and proved. This distinction avoids loading a numerical union of cycles with unproved global smoothness, invariance, uniqueness, or stability.

1.3 What the established theories provide

The thesis lies at the intersection of several mature communities. Their roles are complementary rather than competing.

Natural dynamics and passive gait families. Conservative and passive locomotion studies already show that a fixed mechanism can support continua of gaits, different gait types, and transitions organized by energy, design, and bifurcation structure (Remy, 2011; Gan et al., 2018; Raff et al., 2022). Natural-motion-manifold control further shows how families of passive motions can become control targets (Calzolari et al., 2025). The present work does not claim the first natural gait family. It asks how reduced return can be constructed and mechanically interpreted in the declared nonholonomic articulated models.

Linear and nonlinear modal organization. Linear modes provide tangent directions near equilibrium. Nonlinear normal modes extend coherent oscillatory motions to finite amplitude, where frequency, waveform, and coordinate relations can change (Rosenberg, 1966; Shaw and Pierre, 1993; Kerschen et al., 2009; Peeters et al., 2009). This theory supplies the oscillatory organization and spectral seeds used here. Locomotion adds open pose directions and a reduced-return condition that an ordinary full-state NNM does not express.

Symmetry, reconstruction, and relative periodicity. Geometric mechanics separates shape from pose and reconstructs rigid-body motion from reduced dynamics or prescribed shape changes (Kelly and Murray, 1995; Ostrowski and Burdick, 1998; Bloch, 2015). Relative-periodic orbits provide the correct return language when symmetry directions drift (Fasso et al., 2020; Eldering and Jacobs, 2016). The present construction uses exact pose reconstruction after solving the reduced dynamics; it does not infer dynamical compatibility from the geometry of a prescribed loop.

Periodic-orbit and forced-response computation. Shooting and pseudo-arclength continuation are established ways to correct periodic solutions and follow their branches through folds (Peeters et al., 2009; Kuznetsov, 2004). In damped systems, conservative backbones, cycle work balance, forced responses, and phase resonance are also well-developed concepts (Cenedese and Haller, 2020a,b; Peeters et al., 2011; Kuether et al., 2015). Phase-locked and control-based continuation methods already track nonlinear responses in simulation and experiments (Peter et al., 2016; Peter and Leine, 2017; Denis et al., 2018; Renson et al., 2016; Barton, 2017; Abeloos et al., 2022). The forced contribution below is a locomotor integration of these ideas, with mean speed added as a second local observable; it is not a claim that PLL continuation itself is new.

The closest antecedents therefore establish most of the individual tools. The specific analytical delta of the thesis is narrower: under explicit scalar section hypotheses, the exchange of a derived transverse storage has exactly the same zero set as the last unresolved return coordinate. The principal multi-degree numerical delta is the construction and classification of coexisting moving IP and AP branch-chain sectors at one fixed model-parameter vector. The other results build and test the surrounding workflow on the two declared locomotor architectures.

1.4 Contributions and evidence levels

The five contribution groups form one sequence, but they do not have the same logical status. Table 1.1 states both the result and the evidence that supports it.

Table 1.1: Contribution hierarchy and evidence domain. Numerical population sizes measure archive coverage; they are not arguments for novelty or theorem status.

Contribution group	**Result established**	**Evidence and boundary**
Two-segment family	A transverse spectral seed is corrected and continued into finite-amplitude moving relative-periodic cycles; their nonlinear choreography and pose are reconstructed.	Model-specific numerical precursor. Straight drift is the family boundary; a matched $\mathrm{SE}(2)$ comparison shows that straight drift typically dominates total translation away from near-zero speed.
Closed–open construction and scalar theorem	Carrier elimination exposes a transverse storage and an auxiliary carrier-closed field. On the declared oriented scalar section, zero integrated exchange is equivalent to the last return row once the other rows close.	Main analytical result under finite-speed, transversality, orientation, and storage-injectivity hypotheses, with a finite numerical realization. It is not a general existence theorem.
Three-segment modal families	Full vector return and independent modal metrics produce coexisting moving IP and AP branch-chain sectors at one fixed numerical parameter vector.	Strongest numerical construction. The explicitly audited rows support return, reconstruction, and modal claims; they do not provide a population-wide closed-support genealogy, stability result, or hardware validation.
Resonant locomotion map	A local same-mechanics homotopy deforms one conservative cycle into a maintained response. Separately, a damped, periodically driven two-segment archive is organized by forcing, phase, waveform, mean speed, and reconstructed pose.	Numerical bridge for one synchronized branch, plus an independent response computation for a parameter-distinct model. No whole-family persistence, stability, connection between the two data sets, or global quadrature optimality is established.
Local phase–speed navigation	A fast frequency PLL and a slower mean-speed loop traverse a tested segment of the observable forced-response chart.	Nominal simulation from two initializations, with sampled reduced-order linearizations. The archive exercises no rejected-trial recovery and does not prove exact-plant or global stability.

The conservative construction proceeds from the simpler to the more informative model. The two-segment mechanism makes a one-dimensional transverse return visible. The closed–open chapter then proves what an exchange balance can replace in precisely that scalar setting. Adding a second internal coordinate exposes the dimensional boundary: one storage value no longer identifies the returned point, so vector return and modal classification must remain separate. The forced and control chapters subsequently change the energy regime and answer how a related locomotor response chart can be maintained and navigated locally.

Parts of this sequence have appeared in associated co-authored outputs. The two-segment family is related to the Mechatronics study (Rajaomarosata et al., 2025a); the forced-response model is related to the OCEANS study (Rajaomarosata et al., 2025b); and the closed–open and three-segment strands are related to the public preprint (Mortel et al., 2026). The dissertation rederives the common mechanics in one notation, narrows claims according to the reproducibility audits, and makes the scalar-versus-vector return boundary explicit. These outputs are cited at the point where their results are used; figure-specific data provenance is recorded in the repository ledger.

1.5 Models, scope, and three-day reading path

The two mechanisms are normalized planar articulated systems with ideal no-side-slip constraints. The conservative models contain elastic storage but no damping or maintained actuator input. The local bridge retains one conservative model's mechanics while adding a declared damping law and periodic joint torque; the large forced-response archive uses a different numerical parameter vector. These are analytical and numerical mechanisms, not calibrated hardware replicas, biological models, or optimized designs. Forward translation is the primary locomotor observable, while the complete reconstructed output remains a pose increment in $\mathrm{SE}(2)$.

The main text is designed as a three-day path. Detailed coefficient algebra, solver protocols, and archive audits remain available in the appendices and repository without interrupting the central argument.

Table 1.2: Three-day reading path and comprehension target.

Day	Chapters	The reader should be able to explain
1	Chapters 1–3	Why a nonlinear natural family is not a fixed sine wave; why locomotion uses reduced rather than full-state periodicity; why reconstruction is not a dynamics test; and how the first two-segment family is computed.
2	Chapters 4–5	What is closed and reopened; why exchange replaces one scalar return row in the two-segment theorem; why it cannot replace vector return in three segments; and how IP/AP families are classified.
3	Chapters 6–8	How input work maintains dissipative responses; why work balance is exact but quadrature is local; why phase and speed are both used for navigation; and which links remain a research programme.

Chapter 2 now supplies the minimum cross-community foundations needed to follow this path without an external textbook. It begins with natural nonlinear oscillations, then adds modal organization, open pose, relative periodicity, and the numerical construction of cycle families. The result chapters can then focus on what the thesis establishes rather than reintroducing each tool at the point of use.

Chapter 2

From natural oscillations to repeatable locomotion

This chapter constructs the minimum common language needed by the rest of the thesis. It begins with a one-degree oscillator, where amplitude, waveform, and frequency already vary along a family of natural motions. It then adds internal degrees of freedom, opens the locomotor pose variables, and separates three questions that are often conflated: whether a trajectory solves the mechanical equations, whether its reduced state returns, and what pose increment is reconstructed from it.

2.1 A natural oscillation is a family, not a sine wave

A small-amplitude mass–spring oscillator suggests a familiar picture of natural motion: one sinusoid with one natural frequency. That picture is local. A pendulum released through a large angle is still moving freely under its own conservative mechanics, but it slows markedly near its turning points, moves fastest through the bottom of the well, and takes longer to complete a cycle as the release angle increases. Periodicity survives; a fixed sinusoidal waveform and a frequency independent of amplitude do not.

2.1.1 Closed energy loops

Consider one local oscillator coordinate x, with momentum $p = M(x)\dot{x}$, positive inertia $M(x)$, and potential $U(x)$. Its Hamiltonian is

$$H(x,p) = \frac{p^2}{2M(x)} + U(x) = E. \tag{2.1}$$

Energy conservation confines a free trajectory to a level set of H. In a regular potential well, an energy below the escape level intersects the potential at two turning points. The positive- and negative-momentum branches join there to form a closed curve in the phase plane. One circuit of that curve is one natural oscillation.

The family, rather than one waveform, is the useful object. Each regular energy value selects another loop, and the time needed to traverse the loop is

$$T(E) = 2\int_{x_-(E)}^{x_+(E)} \sqrt{\frac{M(x)}{2\{E - U(x)\}}}\,\mathrm{d}x, \qquad \Omega(E) = \frac{2\pi}{T(E)}. \tag{2.2}$$

The integrand becomes large near an ordinary turning point because the velocity vanishes there. This unequal time of flight is precisely why the physical coordinate is generally not a cosine. With constant inertia, a quadratic potential is the special case for which the period is independent of E and the waveform is sinusoidal.

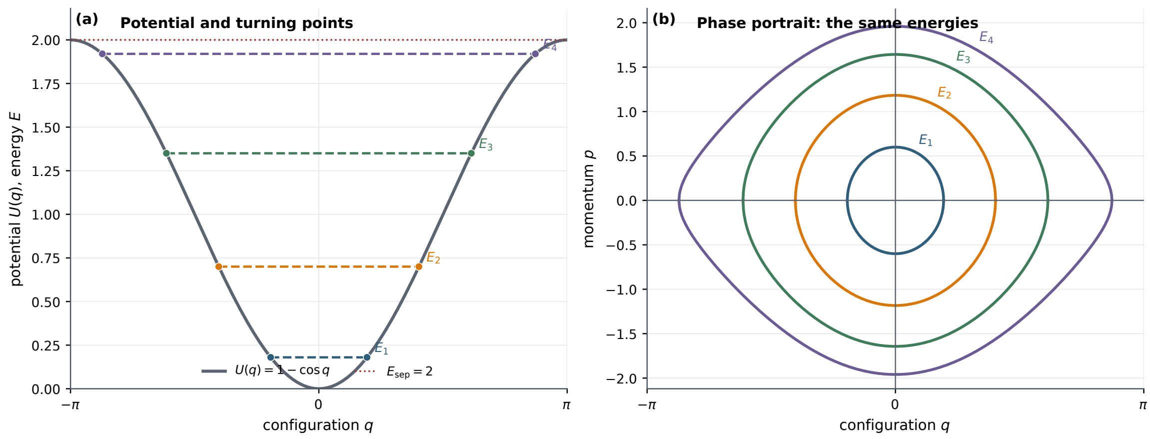

Figure 2.1: Energy organizes a family of bounded pendulum oscillations. Left: each energy below the separatrix intersects the potential at two turning points. Right: the corresponding momentum branches form a closed phase-space loop. Increasing the energy changes both the loop and its period. The q in this pedagogical figure is a local pendulum coordinate, not the full locomotor configuration used later.

2.1.2 Action labels the loop; angle clocks the motion

Energy is a physical family label. Action provides a canonical geometric label for the same loop:

$$J(E) = \frac{1}{2\pi} \oint_{H=E} p \, \mathrm{d}x. \tag{2.3}$$

The contour integral is the oriented area enclosed in the phase plane divided by 2π. It measures the size of the whole state-space cycle, rather than only the largest displacement. On a regular annulus of such loops, E can locally be written as $H(J)$. An angle φ can then be chosen as a uniform clock along each member:

$$\dot{J} = 0, \qquad \dot{\varphi} = \Omega(J) = \frac{\mathrm{d}H}{\mathrm{d}J} = \frac{2\pi}{T(J)}. \tag{2.4}$$

Thus J says which oscillation is taking place and φ says where the state lies on it. These are the Hamiltonian analogues of radius and polar angle, but the analogy must not be pushed too far: the radius-like quantity is a phase-space area, and the physical loop need not be circular (Arnold, 1989).

Uniform phase also does not make the measured coordinate sinusoidal. The inverse map has the form

$$x(t) = X(J_0, \varphi_0 + \Omega(J_0)t)\,, \tag{2.5}$$

where $X(J, \varphi)$ is periodic in φ but may contain several harmonics. The nonlinearity has been moved into this map; it has not been removed.

2.1.3 The pendulum makes the amplitude dependence visible

Let ϑ be the pendulum angle, I its inertia, and $\omega_0 = \sqrt{g/l}$ its small-amplitude frequency. The exact Hamiltonian is

$$H(\vartheta, p_\vartheta) = \frac{p_\vartheta^2}{2I} + I\omega_0^2(1 - \cos\vartheta). \tag{2.6}$$

For a libration of maximum angle $a < \pi$, set $k = \sin(a/2)$. Its period and frequency are

$$T(a) = \frac{4}{\omega_0}\,\mathrm{K}(k), \qquad \Omega(a) = \frac{\pi\omega_0}{2\,\mathrm{K}(k)}, \tag{2.7}$$

where K is the complete elliptic integral of the first kind. Near the stable equilibrium, Ω tends to ω_0. As a approaches the upright separatrix, the period diverges and the frequency tends to zero.

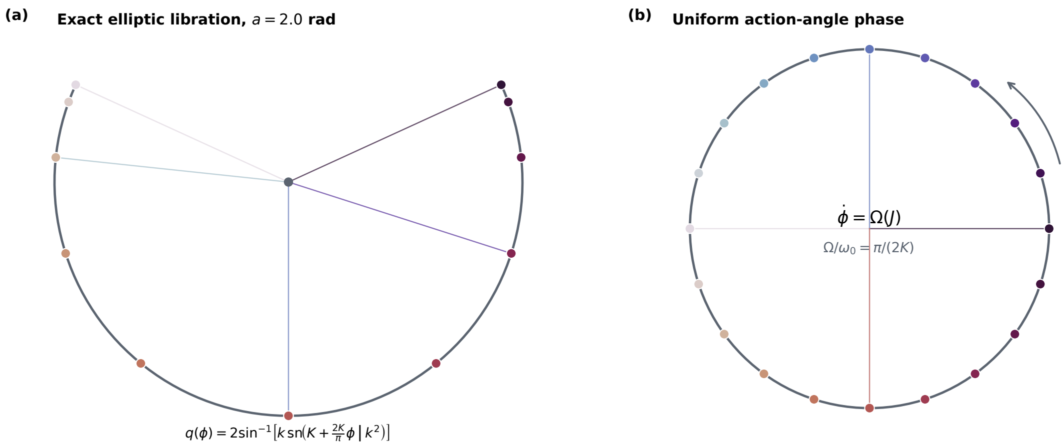

Figure 2.2: The same finite-amplitude pendulum libration viewed in physical configuration and in action–angle phase. The pendulum spends more time near its turning points, whereas the angle variable advances uniformly around the abstract circle. Uniform phase therefore coexists with a non-sinusoidal physical waveform.

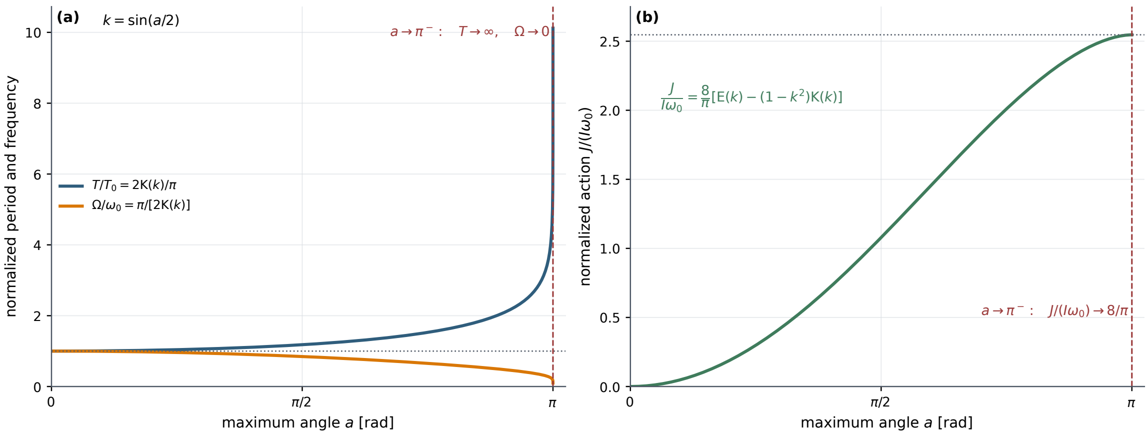

Figure 2.3: Finite-amplitude organization of pendulum librations. The period grows and the frequency decreases with maximum angle, while the action grows with the area enclosed by the phase-space loop. The dashed boundary is the separatrix limit; it is not part of the regular action–angle annulus.

The same mechanism therefore carries a continuum of natural frequencies, one for each member of the libration family.

This construction is deliberately local. It applies on an annulus filled by regular compact energy loops. The action–angle chart is singular at the equilibrium and at the separatrix and does not provide one coordinate system across both librations and rotations. Nor does the one-degree argument imply global action–angle coordinates for a general multi-degree system. Its useful message is narrower: a nonlinear natural oscillation has a family label, an orbit-dependent frequency, and a uniform phase even when its physical choreography is not sinusoidal.

With several oscillatory degrees of freedom, energy no longer identifies one closed loop. A further organizing object is then required before this one-family-label/one-phase picture can be recovered locally.

2.2 Why total energy no longer selects one motion

The scalar construction works because a regular energy level in a two-dimensional phase plane can itself be a closed orbit. For a conservative system with n degrees of freedom, the phase space has dimension $2n$, and a regular energy level has dimension

$$\dim H^{-1}(E) = 2n - 1. \tag{2.8}$$

With two degrees of freedom, one energy value therefore leaves a three-dimensional surface. That surface may contain distinct periodic motions, quasi-periodic trajectories, exchanges of energy between coordinates, and resonant or irregular dynamics. Conservation of energy remains necessary, but it does not select one coherent oscillation. In particular, not every free trajectory on an energy surface is a mode.

2.2.1 Linear modes are local seeds

Near a stable equilibrium, let $\boldsymbol{u}$ denote a small displacement. The linearized equations are

$$M_0\ddot{\boldsymbol{u}} + K_0\boldsymbol{u} = 0, \qquad K_0\boldsymbol{\phi}_j = \omega_j^2 M_0\boldsymbol{\phi}_j. \tag{2.9}$$

Each eigenvector $\boldsymbol{\phi}_j$ gives a configuration-space direction, and the corresponding displacement–velocity pair spans a two-dimensional modal plane in the linearized state space. Motion initialized in that plane is sinusoidal and remains there under the linear equations.

The symmetric double pendulum supplies a concrete picture. Its small-angle model has a lower-frequency in-phase seed, for which the link angles have the same sign, and a higher-frequency anti-phase seed, for which they have opposite signs. In the nondimensional example shown in Figure 2.4, the modal directions are proportional to $(1, \sqrt{2})^\mathsf{T}$ and $(1, -\sqrt{2})^\mathsf{T}$, respectively.

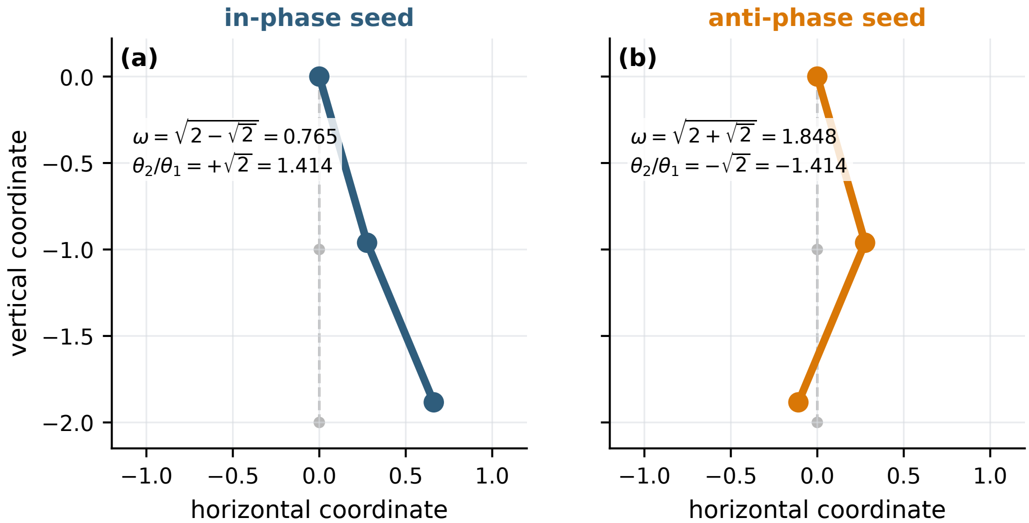

Figure 2.4: The two small-angle modal seeds of the symmetric double pendulum. The in-phase direction moves both links to the same side; the anti-phase direction moves them to opposite sides. These are tangent directions at the downward equilibrium, not finite-amplitude trajectories. The angle symbols in the source figure are local to this example.

The word *local* is essential. A linear eigenvector describes the first variation of the dynamics at one equilibrium. Increasing its amplitude while keeping the same proportional sine waves does not generally solve the nonlinear equations.

2.2.2 Why the linear modal plane bends

Write the nonlinear equations in linear modal coordinates η_j:

$$\ddot{\eta}_j + \omega_j^2\eta_j = N_j(\boldsymbol{\eta}, \dot{\boldsymbol{\eta}}), \tag{2.10}$$

where N_j collects the nonlinear inertia, stiffness, and coupling terms. In the linear model the right-hand side vanishes. In the nonlinear model, setting all modes except mode k to zero need not make

$N_j = 0$ for $j \neq k$. The vector field then points out of the flat linear modal plane. The plane is a correct tangent approximation, but it is not an exact finite-amplitude carrier of motion.

A nonlinear modal family corrects this failure. Starting from a small orbit near one linear seed, the full nonlinear equations determine the changes in period, relative amplitudes, phase relations, and harmonics required for exact closure. Continuing the corrected orbit produces a family rather than one amplified eigenvector. In practical conservative modal analysis, this family of periodic motions is a standard representation of a nonlinear normal mode (Rosenberg, 1966; Shaw and Pierre, 1993; Kerschen et al., 2009; Peeters et al., 2009).

Under suitable local regularity and non-resonance assumptions, the same organization can be described geometrically by a two-dimensional invariant surface tangent to the selected linear modal plane and filled locally by periodic orbits. Existence, uniqueness, and smoothness of such invariant objects require hypotheses; they do not follow merely from plotting a continued branch (Haller and Ponsioen, 2016). The term *family* is used below whenever only the periodic-orbit organization is needed.

2.2.3 Finite-amplitude modes change their choreography

The double-pendulum families in Figure 2.5 make the correction visible. Near the downward equilibrium, the shape-space cycles lie close to the two straight linear modal directions. At larger energy they bend away from those lines, and their phase projections cease to be ellipses. The links remain coherently organized as an in-phase or anti-phase family, but coherence no longer means proportional sinusoids.

This is the useful meaning of *unison* here: the motion has one independent oscillatory clock, so all physical coordinates are functions of one phase along the selected family. It does not require fixed amplitude ratios, simultaneous turning points, or one sinusoid copied into every coordinate.

A backbone curve summarizes the same family by plotting its frequency

$$\Omega_j = \frac{2\pi}{T_j} \tag{2.11}$$

against an orbit label such as energy, action, or amplitude. The linear eigenfrequency is only the zero-amplitude limit, $\Omega_j \to \omega_j$. Moving along the backbone can change the period and the complete waveform, including the harmonics and phase relation between coordinates. A backbone organizes the computed modal family; it neither classifies every free motion nor establishes stability by itself.

2.2.4 Action and phase only after the modal family is chosen

The one-degree action–angle picture can be recovered locally on a selected two-dimensional conservative modal surface. Intersecting that surface with a regular energy level gives a closed periodic member. An action labels nearby members and an angle clocks motion along each one, so locally

$$\dot{J}_j = 0, \qquad \dot{\varphi}_j = \Omega_j(J_j). \tag{2.12}$$

This statement does not assert global integrability of the full multi-degree system. The nonlinear mode first identifies where the coherent oscillation lives; action and phase then describe the regular cycles on that selected object.

The distinction prepares the locomotor construction. The carrier-closed 3SEG model has two effective transverse coordinates and therefore needs modal organization analogous to the in-phase and anti-phase double-pendulum families. Those modes organize candidate internal supports; they do not by themselves establish return of the full opened locomotor state or a nonidentity pose increment. The next step is therefore to separate the periodic internal state from the pose that locomotion must leave open.

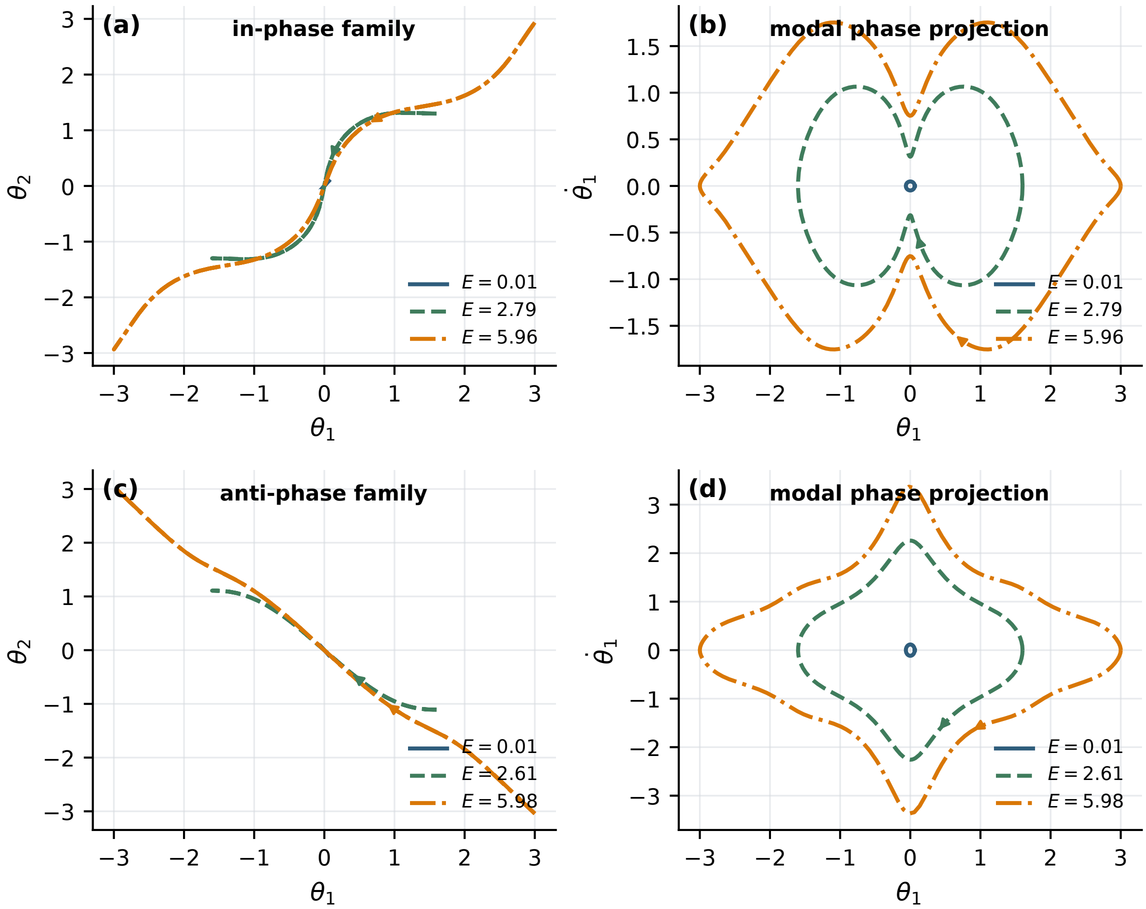

Figure 2.5: Representative corrected periodic members of the in-phase (top) and anti-phase (bottom) double-pendulum families. The left panels show the joint choreography in shape space; the right panels show a phase projection. The smallest cycles approach the linear modal seeds, whereas finite-amplitude cycles deform and become non-elliptic. These selected members do not exhaust the energy surface and do not establish a global invariant manifold.

2.3 Reduced periodicity leaves the pose open

An articulated locomotor can repeat its internal motion without returning to the same place. There is no contradiction: internal deformation and placement in the world are different variables, and they obey different closure conditions. The distinction is most transparent when the configuration is written as

$$q = (g, r), \qquad g \in G, \qquad r \in \mathcal{R}. \tag{2.13}$$

Here g is the body pose and r is the internal shape. For planar locomotion, $G = \mathrm{SE}(2)$: a pose contains two translations and one rotation. The shape contains joint angles or other coordinates measured relative to the body. Changing g moves the whole mechanism; changing r deforms it.

This split is useful when the mechanical laws are unchanged by a common rigid displacement of the mechanism. Absolute position and heading can then be removed from the equations that determine the internal motion. They are recovered afterwards by reconstruction, a standard separation in geometric and nonholonomic locomotion (Kelly and Murray, 1995; Ostrowski and Burdick, 1998; Bloch, 2015).

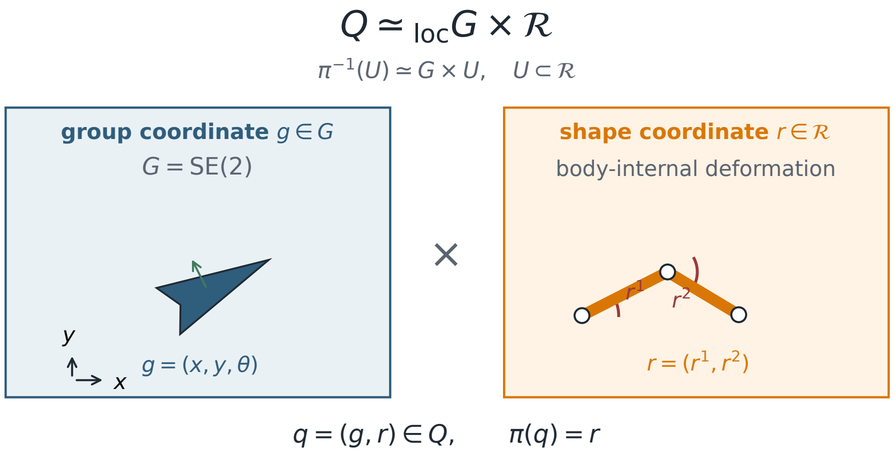

Figure 2.6: The configuration separates into a body pose $g \in G$ and an internal shape $r \in \mathcal{R}$. Pose describes placement in the world; shape describes deformation relative to the body. A locomotor cycle may close in its internal variables while remaining open in pose.

2.3.1 Reduced dynamics and pose reconstruction

Velocity on the pose group is expressed in a body-attached frame. If ξ denotes this body velocity, then

$$\widehat{\xi} = g^{-1}\dot{g}, \qquad \dot{g} = g\widehat{\xi}. \tag{2.14}$$

The first equality converts the world motion into a body velocity; the second reconstructs the pose from that velocity. On $\mathrm{SE}(2)$, the components of ξ are the two body-frame translation rates and the yaw rate. Because rotations and translations do not commute, the final pose depends on the ordered history of these velocities, not merely on their separate scalar integrals.

The reduced mechanical state is denoted by z. It contains every variable needed to advance the pose-independent dynamics: shape, shape rates and, when required, admissible carrier velocities or reduced momenta. In the unforced conservative setting, reduction and reconstruction have the schematic form

$$\dot{z} = f_0(z), \qquad \xi = \Xi(z), \qquad \dot{g} = g\widehat{\Xi(z)}. \tag{2.15}$$

The first equation decides which timed reduced trajectories are mechanically possible. The last two decide where one such trajectory carries the body. Reconstruction is therefore kinematic bookkeeping driven by a mechanical solution; it is not an additional force law.

In a purely kinematic model, the middle relation may reduce to a local connection, $\xi = -A(r)\dot{r}$. That compact formula is not universal. In an inertial or nonholonomic locomotor, Ξ can also depend on carrier velocity, momentum or other components of z. This is why the returned object used in this thesis is a loop in reduced *state* space rather than merely a curve in shape space.

2.3.2 Exact reduced return and nontrivial group displacement

Let a solution of Equation (2.15) start from (g_0, z_0). It is a transporting relative-periodic motion if, for some $T > 0$,

$$z(T) = z_0, \qquad \Delta g := g_0^{-1} g(T) \neq e_G, \tag{2.16}$$

where e_G is the identity pose. The first equality is exact reduced return: after one period the mechanism has the same internal configuration and the same reduced velocities. The second condition states that reconstruction has accumulated a nonidentity pose increment. This is relative periodicity: the motion is periodic after quotienting the pose symmetry, but not in the full configuration (Fasso et al., 2020).

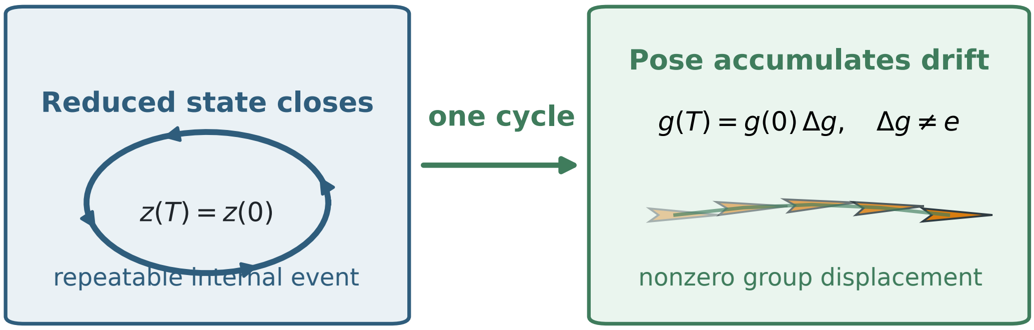

Figure 2.7: Relative periodicity separates two endpoint tests. The timed reduced state returns after one cycle, whereas reconstruction changes the body pose by Δg. Closure of the reduced loop does not require closure of the pose.

Full-state periodicity would instead impose both $z(T) = z_0$ and $g(T) = g_0$. It would therefore force $\Delta g = e_G$: the mechanism could move during the cycle, but it would return to its initial pose and produce no net transport per cycle. Ordinary full-state periodicity is consequently the wrong endpoint condition for a transporting gait. Pose must be removed from the return residual and evaluated as an output of reconstruction.

When the same reduced cycle is repeated, symmetry makes the body-frame increment repeat as well. The poses at complete cycles satisfy

$$g(nT) = g_0(\Delta g)^n. \tag{2.17}$$

A translational increment produces repeated advance; an increment containing rotation composes into a turning motion. The group product, rather than vector addition of world displacements, preserves the order in which translations and rotations are accumulated.

2.3.3 How planar pose increments are compared

Only a small part of the SE(2) algebra is needed later. Write a planar pose as a rotation and a world position, $g = (R, p)$. Composition and inversion are

$$(R_1, p_1)(R_2, p_2) = (R_1R_2,\; p_1 + R_1p_2), \qquad (R, p)^{-1} = (R^\mathsf{T}, -R^\mathsf{T}p). \tag{2.18}$$

The rotation of the first pose therefore acts on the translation of the second. This is why two world-coordinate displacement vectors cannot simply be subtracted when their headings differ.

A constant body velocity $\xi = (v_x, v_y, \omega)$ acting for time T produces the group increment

$$\Delta g = \mathrm{Exp}\Big(T\widehat{\xi}\Big)\,. \tag{2.19}$$

Conversely, the principal logarithm $\mathrm{Log}(\Delta g)$ expresses an increment as one local twist vector. Its rotational component uses the principal angle, so the branch convention must be declared when a rotation approaches $\pm\pi$. The increments used below remain on the audited principal branch.

For example, comparing a cycle with a reference motion means composing group elements,

$$\Delta g_{\mathrm{inc}} = \Delta g_{\mathrm{base}}^{-1}\Delta g_{\mathrm{cycle}}, \tag{2.20}$$

and then, if a vector summary is useful, taking $\mathrm{Log}(\Delta g_{\mathrm{inc}})$. This produces a reference-dependent residual transform. It is neither an additive energy partition nor a causal attribution of propulsion.

The equality $z(T) = z_0$ is stronger than $r(T) = r(0)$. Returning the joint angles while reversing a joint rate lands at the opposite crossing of the same oscillation. Returning the shape while changing a carrier velocity does not reproduce the same mechanical event either. A repeatable locomotor motion therefore requires a *timed* reduced-state trajectory, including the velocities needed by the model, and not only the geometric trace of the shape.

2.3.4 Reconstruction does not certify dynamical compatibility

Given a prescribed loop $r(t)$ and a reconstruction law, geometric locomotion can compute a pose increment. Many different loops can yield nonidentity increments, and they can be drawn by hand, optimized for distance, imposed by actuators or produced by feedback. This makes reconstruction a powerful tool for gait analysis and design. It does not show that a loop would occur as an unforced motion of the mechanism.

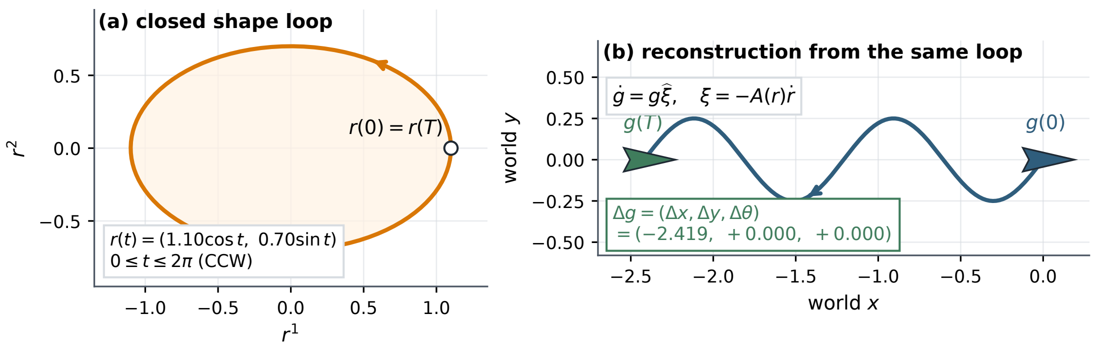

Figure 2.8: Conditional reconstruction: a closed shape loop can produce an open pose path. The diagram establishes how closure in shape and drift in pose can coexist. It does not establish that the displayed loop solves the unforced dynamics, nor that shape alone is the complete reduced state.

Timing is part of this distinction. The same geometric curve traversed with a different time law has different shape velocities and accelerations. In an inertial system it generally requires different forces and need not satisfy the same equations. Even a closed curve in $(r, \dot r)$ is only a candidate until its tangent agrees with the reduced vector field at every point.

The conservative locomotor test therefore has three logically separate rows:

$$\underbrace{\dot z(t) = f_0(z(t))}_{\text{dynamical compatibility}}, \qquad \underbrace{z(T) = z(0)}_{\text{exact reduced return}}, \qquad \underbrace{\Delta g \neq e_G}_{\text{nontrivial transport}}. \tag{2.21}$$

The first row distinguishes a natural conservative motion from an arbitrarily prescribed choreography. The second makes the motion repeatable in the reduced mechanics. The third distinguishes locomotion from oscillation in place. Family or modal organization then relates neighboring solutions; it does not replace any of these three tests.

The next section turns reduced return into a computable residual. Its phase and continuation conditions choose numerical representatives of cycles and families; they do not add physical constraints to Equation (2.21).

2.4 From a returned cycle to a corrected family

A reduced periodic orbit is a closed trajectory, not a distinguished point. Choosing its initial condition only chooses where the clock reads zero. A numerical method must remove this arbitrary phase before it can distinguish a failure to close from a harmless shift along the same orbit. It must then follow neighboring corrected cycles even when a familiar physical parameter ceases to be a good coordinate. Sections, shooting and pseudo-arclength continuation address these two geometric difficulties.

2.4.1 An oriented section turns a cycle into a fixed point

Consider a reduced autonomous system

$$\dot{z} = f(z; \lambda), \tag{2.22}$$

where λ is a model or family parameter and $\Phi^t_\lambda(z_0)$ denotes the flow. Rather than observing a periodic orbit at every instant, choose a codimension-one surface $h(z) = 0$ that the flow crosses transversely. Keeping one direction of crossing gives the oriented section

$$\Sigma^+ = \{z : h(z) = 0,\ \mathrm{D}h(z) f(z; \lambda) > 0\}\,. \tag{2.23}$$

The strict sign has two roles. It excludes tangency, where the return event is poorly conditioned, and it discards the crossing in the opposite direction. For an oscillator, a section such as $r = 0$ is usually crossed once with $\dot{r} > 0$ and once with $\dot{r} < 0$. Retaining both can confuse a half-cycle with a full return.

Let $\tau(z)$ be the first positive return time to Σ^+. The return map is

$$P_\lambda(z) = \Phi^{\tau(z)}_\lambda(z), \qquad z \in \Sigma^+. \tag{2.24}$$

A cycle becomes the fixed-point equation $P_\lambda(z_*) = z_*$. The section does not create periodicity; it selects one representative event on the cycle and expresses all remaining closure information transversely (Kuznetsov, 2004).

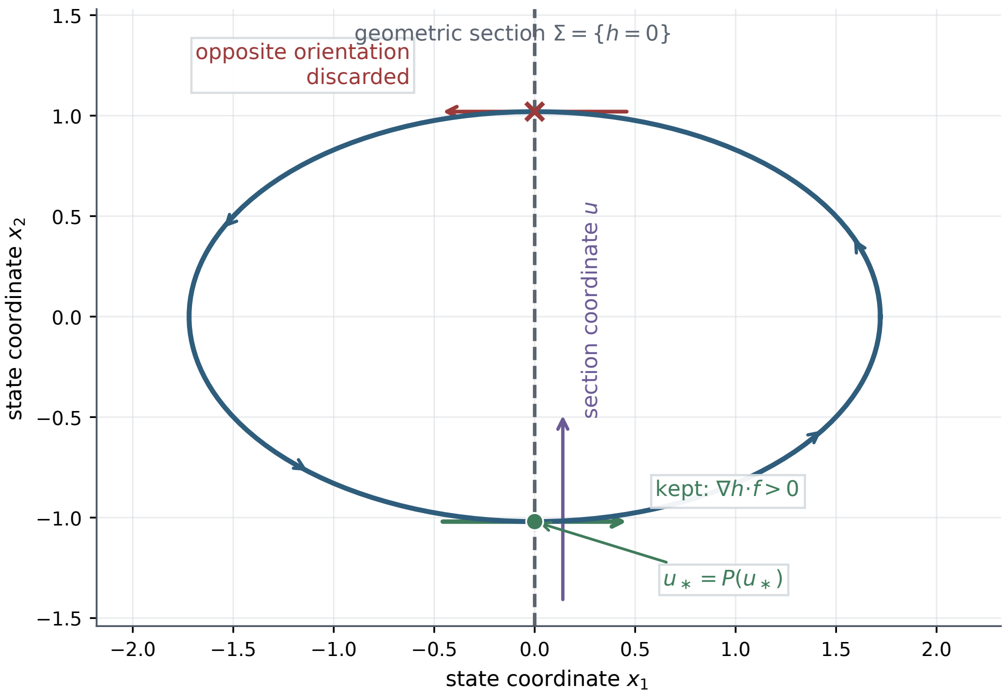

Figure 2.9: An oriented Poincaré section samples one crossing per complete cycle. The continuous orbit becomes a fixed point of the return map; the crossing with the opposite orientation is discarded.

For a relative-periodic locomotor, the map acts on the reduced state. The pose is reconstructed over the accepted return segment and is not included in the fixed-point equality. Including absolute pose in the return vector would replace relative periodicity by full-state periodicity and force the net pose increment to the identity.

2.4.2 Shooting corrects closure and a phase row fixes the clock

A section is convenient when a clean event is available. A more general description treats the initial state z_0 and the period T as unknowns. Single shooting integrates once around the proposed cycle and forms

$$R(z_0, T, \lambda) = \Phi_\lambda^T(z_0) - z_0. \tag{2.25}$$

The equation $R = 0$ closes the trajectory, but it has no preferred time origin: if $z_*(t)$ is periodic, every shifted point $z_*(t + s)$ represents the same orbit. This neutral tangent direction makes a Newton correction underdetermined unless one scalar phase condition is added. A common local choice is

$$\psi(z_0) = \langle z_0 - z_{\text{ref}}, f(z_{\text{ref}}; \lambda)\rangle = 0. \tag{2.26}$$

It asks the new initial point to lie in a hyperplane transverse to a nearby reference orbit. Other pointwise or integral phase conditions serve the same purpose. The corrected cycle solves

$$\mathcal{F}(z_0, T, \lambda) = \begin{bmatrix} R(z_0, T, \lambda) \\ \psi(z_0) \end{bmatrix} = 0. \tag{2.27}$$

The phase row is a gauge: it chooses the clock origin but exerts no force and does not imply stability. An oriented section and a phase condition are two representations of the same need. The former chooses the sampling event geometrically; the latter pins a representative inside a shooting or boundary-value unknown.

Correction is local. A linear mode, a small-amplitude orbit or a neighboring corrected solution can provide a seed close to a root. Newton iterations then adjust the initial state and period until the scaled closure and phase residuals meet their declared tolerances. The seed supplies a tangent or an initial guess; it is not the finite-amplitude solution. This distinction is especially important for nonlinear modal families, whose waveform and period can depart substantially from the linear seed (Peeters et al., 2009).

2.4.3 Pseudo-arclength follows the curve through a fold

After one corrected orbit has been obtained, neighboring orbits are represented as roots of a residual

$$F(u, \lambda) = 0, \tag{2.28}$$

where u collects the orbit unknowns, including its period and phase-fixed representation. Stepping λ and correcting u works while the branch is a graph $u(\lambda)$. At a fold, the solution curve remains smooth in the full (u, λ) space but turns in its projection onto λ. The physical parameter has failed as a local branch coordinate; the family has not necessarily ended.

Pseudo-arclength continuation follows the curve itself. With $y = (u, \lambda)$, let t_j be a unit tangent at a known root y_j. A predictor and its corrected point satisfy

$$y_{\text{p}} = y_j + \Delta s\, t_j, \qquad F(y) = 0, \qquad t_j^{\mathsf{T}}(y - y_{\text{p}}) = 0. \tag{2.29}$$

The first expression advances along the tangent. The last equation restricts the correction to the hyperplane normal to that tangent. It replaces the failed choice of λ by a local branch gauge and can pass a simple fold. A branch point is different: several local branches meet and additional information is required to decide whether and how to switch branches.

Continuation therefore follows the residual it is given. It can organize a family, expose folds and supply neighboring initial guesses, but it cannot decide by itself whether the solutions are natural, transporting, modal or stable. Those meanings depend on the vector field, the return rows, reconstruction and the claim-specific tests attached to each solution.

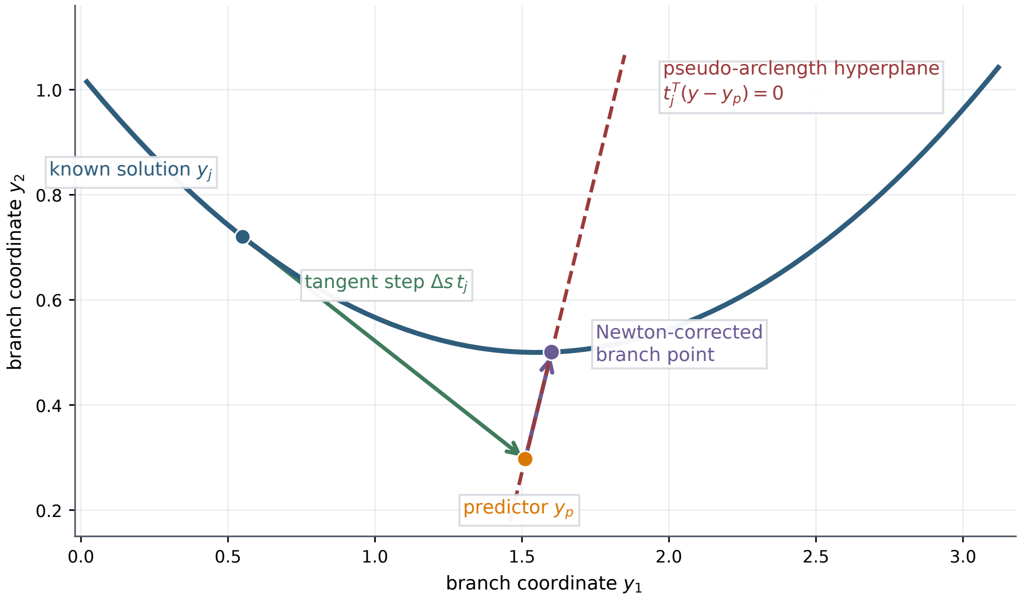

Figure 2.10: Pseudo-arclength predictor–corrector geometry. A tangent predicts a nearby point on the solution curve; correction then solves the physical residual together with a hyperplane gauge. The gauge enables continuation through a fold in the plotted parameter but adds no mechanical equation.

2.4.4 Candidate, corrected solution and audited result

Three statuses keep the numerical construction separate from its mechanical interpretation.
Candidate. A seed, predictor or approximate cycle lies near the expected branch. Exact closure, dynamical accuracy and claim-specific meaning have not yet been established.
Corrected solution. The declared orbit residual, phase row and numerical acceptance gates pass with stated scaling and tolerances. This does not establish stability, uniqueness, global continuation or the mechanical claim attached to the branch.
Audited result. The corrected solution also passes the documented independent checks: raw-field consistency, parameter identity, reduced closure, reconstruction and the relevant energy, exchange or modal rows. The result is not thereby a theorem, an exhaustive classification, a robustness statement or an experimental validation.

A smooth branch plot can contain candidates that have not passed the return test, and a small shooting residual can belong to the wrong physical parameter set or omit a necessary mechanical row. Conversely, an audited finite archive is still a numerical construction rather than a proof of a global manifold. The status attached to a result must therefore follow the checks actually performed, not the visual smoothness or size of the branch.

The conservative chapters use this hierarchy in a fixed order: obtain a seed, correct exact reduced return, continue neighboring solutions, reconstruct their pose increments and finally apply the dimensional exchange or modal tests appropriate to the model. The numerical gauges make the family computable; the mechanics gives it meaning.

2.5 What losses change

The constructions introduced so far concern an unforced conservative field. If a state is initialized exactly on one of its periodic or relative-periodic solutions, no maintained input is required to compensate an energy loss that the model does not contain. This statement does not make the orbit attractive: a perturbed initial condition can remain on a neighbouring motion or depart from the family.

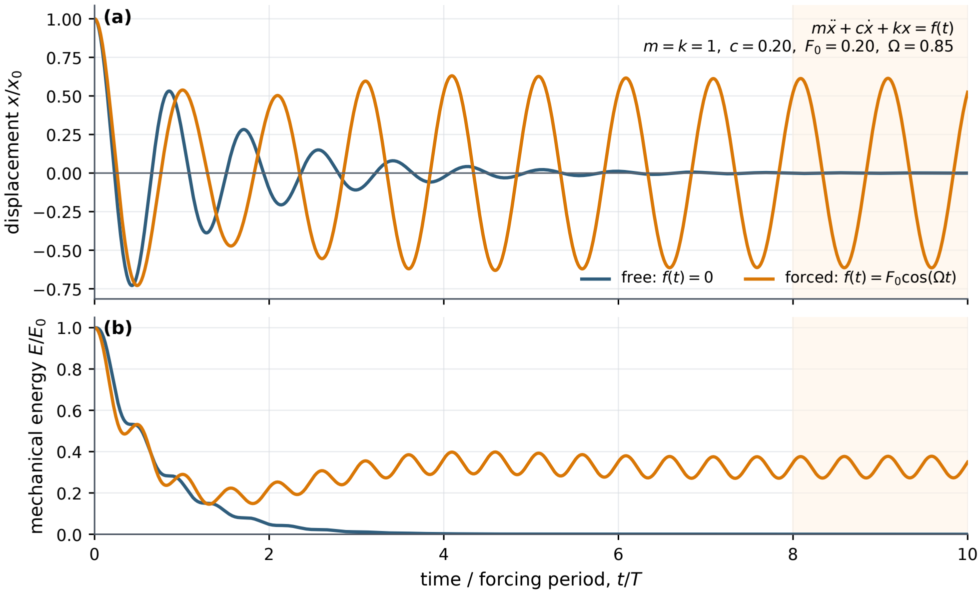

Figure 2.11: Changing the energy regime changes the repeatable object. A conservative oscillation can persist at fixed energy, a damped free motion decays, and a maintained periodic response requires input work. The last case is forced rather than passive, even when the forcing accompanies the response instead of prescribing its full waveform.

Damping changes the accounting before it changes the numerical method. Let E denote the mechanical energy, P_{in} the instantaneous power supplied by an actuator, and $P_{\text{diss}} \geq 0$ the power removed by the declared loss model. Then

$$\dot{E} = P_{\text{in}} - P_{\text{diss}}. \tag{2.30}$$

With no input, a non-equilibrium motion loses energy and its oscillation decays. A period-matched forced response can return to the same state only if the energy supplied during one period replaces the dissipated energy:

$$z(T) = z(0) \quad \Longrightarrow \quad \int_0^T P_{\text{in}}\,\mathrm{d}t = \int_0^T P_{\text{diss}}\,\mathrm{d}t. \tag{2.31}$$

This equality is an exact necessary accounting identity for a periodic response. It is not sufficient to determine the waveform, phase, stability, or even existence of that response; those still follow from the complete forced equations and return conditions.

In a lightly damped linear oscillator, an output–input phase near quadrature has a transparent power interpretation: the applied force is approximately in phase with velocity. In a nonlinear multi-coordinate mechanism, harmonics, several loss channels, and folds make phase a signal-dependent local marker rather than a universal energetic criterion. Chapter 6 therefore keeps two statements separate: cycle work balance is exact, whereas the observed alignment between quadrature and a speed ridge holds only on the reported part of the computed response chart.

The same distinction guides feedback. Accompanying a response family does not require prescribing every harmonic when a few observables locate the desired portion of the chart. In the controller studied here, the deformation–torque phase adjusts forcing frequency on a fast loop, and mean forward speed adjusts forcing amplitude on a slower loop. This is a local navigation result for the forced model, not energy control or stabilization of the conservative family.

2.6 Qualification before organization

The foundations can now be assembled into the sequence used throughout the thesis. A curve is not promoted from one step to the next merely because it looks oscillatory or reconstructs a displacement.

1. **Dynamical compatibility.** The time-parameterized reduced trajectory, including velocities, must solve the specified mechanical field. A linear eigenvector, a guessed sinusoid, or a prescribed shape loop is only a candidate.
2. **Nontrivial exact reduced return.** The corrected trajectory must return to the same reduced state under a declared phase or minimal-period convention. Straight relative equilibria supply useful seeds and boundaries but are not converted into cycles by an arbitrary choice of return time.
3. **Declared locomotor output.** Pose reconstruction evaluates the group increment. A nonidentity increment qualifies a moving relative-periodic motion; attributing an additional propulsive effect to internal oscillation requires comparison with a matched straight-drift reference.
4. **Family organization and modal classification.** Continuation follows connected branches of corrected solutions. When several internal coordinates are present, cycle-level metrics can distinguish organizations such as in-phase and anti-phase motion. These labels organize qualified cycles; they are not extra naturality conditions.

The closed–open exchange construction enters at a precise location inside the second step. In the scalar two-segment problem, once the other return rows are imposed, the integrated exchange of a derived transverse storage can replace and interpret the last return row under the theorem's section hypotheses. In the three-segment problem, one storage value cannot identify a point on the higher-dimensional section. Full vector return remains necessary; exchange then becomes a balance identity and a finite-tolerance diagnostic, while modal metrics classify the returned cycle.

This ordering prevents three common shortcuts. Reconstruction is not a test of the mechanical field. Zero exchange is not an independent condition added after complete return. Modal identity is not a substitute for return. With these roles fixed, Chapter 3 can introduce the first locomotor family by following one object from a straight relative-equilibrium seed to a corrected finite-amplitude cycle and its reconstructed pose.

What the reader can now explain

The reader should now be able to distinguish an energy-labelled oscillation family from a fixed sinusoid, a full periodic orbit from a relative-periodic locomotor motion, and geometric reconstruction from dynamical admissibility. The same distinctions determine the order of the conservative construction in Chapters 3–5.

Part II

Conservative construction

Chapter 3

Two-segment natural-locomotion families

Conservative gait continua and nonlinear-modal continuation already establish that a mechanical system can support families of periodic motions rather than one prescribed waveform (Remy, 2011; Raff et al., 2022; Kerschen et al., 2009; Peeters et al., 2009). The boundary of those antecedents for the present problem is the locomotor return structure: the internal and carrier velocities must repeat while planar pose remains open. This chapter's delta is model-specific. It derives that structure for the two-segment nonholonomic mechanism, corrects a transverse spectral seed into finite-amplitude relative-periodic cycles, follows their branch, and separates their pose increment from a matched straight-drift reference.

The result is a numerical family, not an existence, stability, or global manifold theorem. The archived continuation stage contains 379 samples in the displayed speed window, but it does not provide an independent full-residual recomputation for every sample. The straight relative equilibria below are seeds and boundaries of the nontrivial family; they are not counted as periodic cycles by choosing an arbitrary return time.

3.1 Mechanical model

3.1.1 Configuration, constraint, and reconstruction

The 2SEG system consists of a planar chassis and one internal rigid segment joined by a torsional spring. Its configuration is

$$q = (g, \delta), \qquad g = (x, y, \theta) \in \mathrm{SE}(2), \tag{3.1}$$

where δ is the relative joint angle. The chassis can roll along its heading but cannot move sideways at its contact point:

$$A(\theta)\dot{q} = 0, \qquad A(\theta) = \begin{bmatrix} -\sin\theta & \cos\theta & 0 & 0 \end{bmatrix}. \tag{3.2}$$

This is called a *nonholonomic* constraint: it restricts instantaneous velocities and cannot, in general, be integrated into a fixed relation among x, y, and θ. An admissible velocity can be written as

$$\dot{q} = H(\theta)\eta, \qquad H(\theta) = \begin{bmatrix} \cos\theta & 0 & 0 \\ \sin\theta & 0 & 0 \\ 0 & 1 & 0 \\ 0 & 0 & 1 \end{bmatrix}, \qquad \eta = \begin{bmatrix} v & \omega & \sigma \end{bmatrix}^{\mathsf{T}}, \tag{3.3}$$

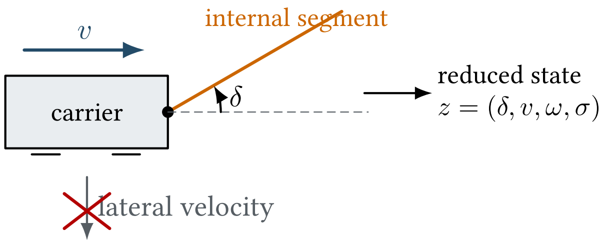

Figure 3.1: The two-segment mechanism and its reduced variables. The ideal wheel-like constraint removes lateral contact velocity; it does not remove forward speed or yaw. The spring-mounted internal segment is described by joint angle δ and joint rate σ.

with longitudinal speed v, yaw rate $\omega = \dot{\theta}$, and joint rate $\sigma = \dot{\delta}$. Because $A(\theta)H(\theta) = 0$, this representation enforces the lateral constraint by construction (Bloch, 2015; Rajaomarosata et al., 2025a).

The geometry is summarized in Figure 3.1; the distinction between exact reduced return and pose drift was introduced in Figure 1.1.

The dynamics are solved in the four-dimensional state

$$z = (\delta, v, \omega, \sigma)^{\mathsf{T}}. \tag{3.4}$$

The planar pose is then reconstructed from

$$\dot{x} = v\cos\theta, \qquad \dot{y} = v\sin\theta, \qquad \dot{\theta} = \omega. \tag{3.5}$$

Consequently, a closed trajectory in z need not close in (x, y, θ). That distinction is the elementary mechanism by which exact reduced return and locomotion coexist.

3.1.2 Compact reduced dynamics

The computations use the dimensionless parameterization

$$\alpha = \varepsilon, \qquad \beta = \mu = 1 - \varepsilon, \qquad j_1 = \gamma\alpha^3, \qquad j_2 = \gamma\beta^3, \tag{3.6}$$

and the passive joint potential

$$U(\delta) = \frac{1}{2}k_2\delta^2 + \frac{1}{4}k_4\delta^4. \tag{3.7}$$

The reference values are

$$\varepsilon = 0.681, \qquad \gamma = 2.504, \qquad k_2 = 1, \qquad k_4 = 10. \tag{3.8}$$

Projection of the Lagrange–d'Alembert equation onto the admissible velocities eliminates the ideal contact reaction and gives the compact balance

$$M(\delta)\dot{\eta} + c(\delta, \eta) + \begin{bmatrix} 0 & 0 & U'(\delta) \end{bmatrix}^{\mathsf{T}} = 0. \tag{3.9}$$

Here c contains the velocity-quadratic inertial terms and

$$M(\delta) = \begin{bmatrix} 1 & -\rho & -\rho \\ -\rho & B_{11} & B_{12} \\ -\rho & B_{12} & B_{22} \end{bmatrix}, \tag{3.10}$$

with

$$\rho(\delta) = \mu\beta\sin\delta, \tag{3.11a}$$

$$B_{11}(\delta) = j_1 + j_2 + \alpha^2 + \mu\beta^2 + 2\mu\alpha\beta\cos\delta, \tag{3.11b}$$
$$B_{12}(\delta) = j_2 + \mu\beta^2 + \mu\alpha\beta\cos\delta, \tag{3.11c}$$
$$B_{22} = j_2 + \mu\beta^2. \tag{3.11d}$$

The dimensional derivation, the explicit inertial vector, and the scaling dictionary are given in Chapter A. In physical terms, ρ couples translation to the two angular rates when the joint is deflected, while the terms proportional to $v\omega$ couple a moving chassis to its yaw and internal dynamics.

Where $M(\delta)$ is nonsingular, define

$$a(\delta,\eta) = -M(\delta)^{-1}\left(c(\delta,\eta) + \begin{bmatrix}0 & 0 & U'(\delta)\end{bmatrix}^{\mathsf{T}}\right) = \begin{bmatrix}a_v & a_\omega & a_\sigma\end{bmatrix}^{\mathsf{T}}. \tag{3.12}$$

The reduced dynamics are then

$$\dot{z} = f(z) = \begin{bmatrix}\sigma & a_v & a_\omega & a_\sigma\end{bmatrix}^{\mathsf{T}}. \tag{3.13}$$

With no forcing or damping, the mechanical energy

$$E(z) = \frac{1}{2}\eta^{\mathsf{T}}M(\delta)\eta + U(\delta) \tag{3.14}$$

is conserved.

3.2 Straight motion and the oscillatory seed

For every constant speed $\bar{v}$, the reduced state

$$z_{\mathrm{re}}(\bar{v}) = \begin{bmatrix}0 & \bar{v} & 0 & 0\end{bmatrix}^{\mathsf{T}} \tag{3.15}$$

satisfies

$$f\big(z_{\mathrm{re}}(\bar{v})\big) = 0. \tag{3.16}$$

Indeed, the spring force, the translation–rotation coupling, and every velocity-quadratic term vanish at $\delta = \omega = \sigma = 0$. In the plane, however, this state produces

$$x(t) = x_0 + \bar{v}t\cos\theta_0, \qquad y(t) = y_0 + \bar{v}t\sin\theta_0, \qquad \theta(t) = \theta_0. \tag{3.17}$$

It is therefore a straight translation, or relative equilibrium, rather than a motionless configuration. The family parameter also generates the exact neutral tangent

$$Df\big(z_{\mathrm{re}}(\bar{v})\big)\begin{bmatrix}0 & 1 & 0 & 0\end{bmatrix}^{\mathsf{T}} = 0. \tag{3.18}$$

Internal oscillations are sought transverse to that tangent, in $\xi_\perp = (\delta_1, \omega_1, \sigma_1)^{\mathsf{T}}$. Linearization gives

$$\dot{\xi}_\perp = J_\perp(\bar{v})\xi_\perp. \tag{3.19}$$

At zero carrier speed, the reference design has the oscillatory eigenpair

$$\lambda_\pm(0) = \pm 3.30569i. \tag{3.20}$$

The associated eigenvector fixes the relative amplitudes and phases of joint angle, yaw rate, and joint rate. At nonzero speed the corresponding pair need not remain exactly imaginary; it initializes the nonlinear solve, which then determines the finite-amplitude cycle (Shaw and Pierre, 1993; Kerschen et al., 2009).

If $\lambda = \alpha_\lambda + i\Omega$ and $p = p_r + ip_i$ denote that pair and a transverse eigenvector at a selected $\bar{v}_0$, embed p as $\widehat{p} = (p_\delta, 0, p_\omega, p_\sigma)^{\mathsf{T}}$. The initial loop is

$$z_{\mathrm{seed}}(t) = z_{\mathrm{re}}(\bar{v}_0) + A\big(\widehat{p}_r\cos\Omega t - \widehat{p}_i\sin\Omega t\big), \qquad A > 0. \tag{3.21}$$

Newton correction supplies the omitted nonlinear deformation, including the variation of v around its mean.

3.3 Shooting and continuation

Let $\Phi_T(z_0)$ be the flow of Equation (3.13). A reduced cycle is a state and period satisfying

$$\Phi_T(z_0) - z_0 = 0. \tag{3.22}$$

Because shifting the initial time gives the same orbit, one phase equation is added, for example

$$(z_0 - z_{\text{ref}})^{\mathsf{T}} f(z_{\text{ref}}) = 0. \tag{3.23}$$

Shooting integrates the model over one candidate period and corrects z_0 and T until these return and phase residuals vanish.

The conservative cycles form a branch rather than isolated attracting limit cycles. The numerical formulation therefore introduces an auxiliary isotropic term $\kappa\eta$ in Equation (3.9). With $X = (z_0, T, \kappa)$, a tangent predictor is corrected together with the scalar pseudo-arclength condition

$$\tau_k^{\mathsf{T}} (X - X_k) = \Delta s. \tag{3.24}$$

This permits the solver to follow folds without choosing period, energy, or mean speed as a global branch parameter (Peeters et al., 2009; Kuznetsov, 2004). The physical system is the slice $\kappa = 0$; on the retained branch the computed values satisfy

$$|\kappa| \leq 7.8 \times 10^{-12}. \tag{3.25}$$

3.4 The continued family and its locomotor meaning

For a cycle of period T, define its mean longitudinal speed by

$$\bar{v} = \frac{1}{T} \int_0^T v(t)\ \mathrm{d}t. \tag{3.26}$$

The continued branch is sampled at 379 points in $-200 \leq \bar{v} \leq 200$. It is shown directly in Figure 3.2, rather than represented only by its numerical ranges.

The two panels expose two different nonlinear changes. Period varies along the branch, and the relative participation of the carrier and internal segment also changes: the joint keeps a finite excursion while chassis yaw becomes small at large $|\bar{v}|$. Scaling one harmonic seed therefore cannot generate the displayed family.

The timing change can be stated independently of the arbitrary point at which a cycle is cut. Write a returned coordinate as $q(t) = \sum_k \widehat{q}_k \exp(2\pi i k t/T)$. For $k \geq 1$, the heading coefficient reconstructed from yaw rate is

$$\widehat{\theta}_k = \frac{T}{2\pi i k} \widehat{\omega}_k. \tag{3.27}$$

The first-harmonic phase difference and yaw-rate harmonic distortion are then

$$\phi_{\delta\theta} = \arg\left(\frac{\widehat{\delta}_1}{\widehat{\theta}_1}\right), \qquad \mathrm{THD}_\omega = \frac{\left(\sum_{k\geq 2} |\widehat{\omega}_k|^2\right)^{1/2}}{|\widehat{\omega}_1|}. \tag{3.28}$$

A time shift rotates both first-harmonic coefficients by the same angle, so $\phi_{\delta\theta}$ does not depend on the chosen section point. An exact single-frequency yaw motion would instead have $\mathrm{THD}_\omega = 0$.

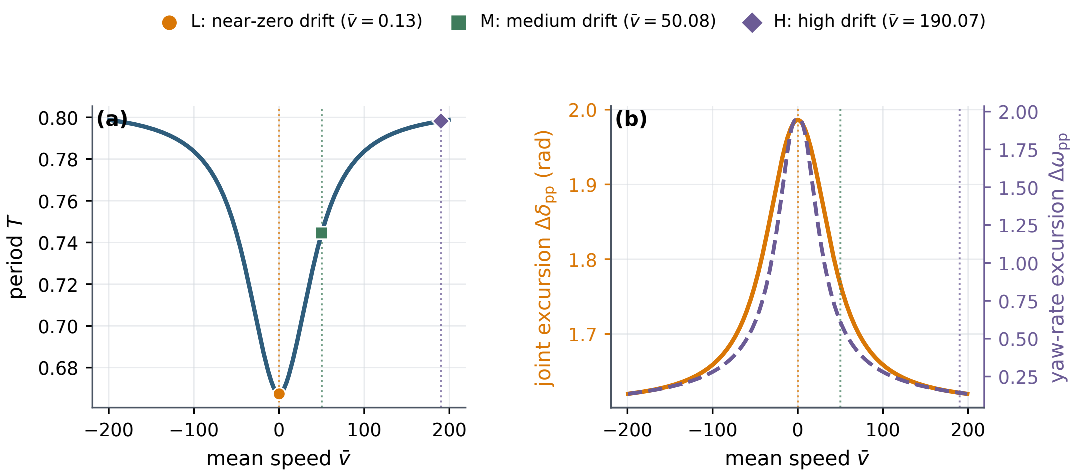

Figure 3.2: Archived 379-cycle family. (a) The corrected period changes from 0.6674 near zero mean speed to about 0.799 at the displayed ends. (b) Joint excursion remains between 1.62 and $1.99\,\mathrm{rad}$ while yaw-rate excursion falls from about 1.94 to 0.135. L, M, and H identify the members used in Figure 3.3. These are archived diagnostics, not a new full-residual or global-manifold certificate.

Near zero speed the joint and heading fundamentals are nearly opposite; by the high-speed representative their unwrapped lag has changed by about $85\,\mathrm{deg}$. At the same time the yaw-rate waveform contains a growing higher-harmonic component. A controller that prescribed one sine wave with a fixed frequency and fixed phase relation would therefore miss two features of the unforced conservative solutions: their speed-dependent clock and their speed-dependent coordination.

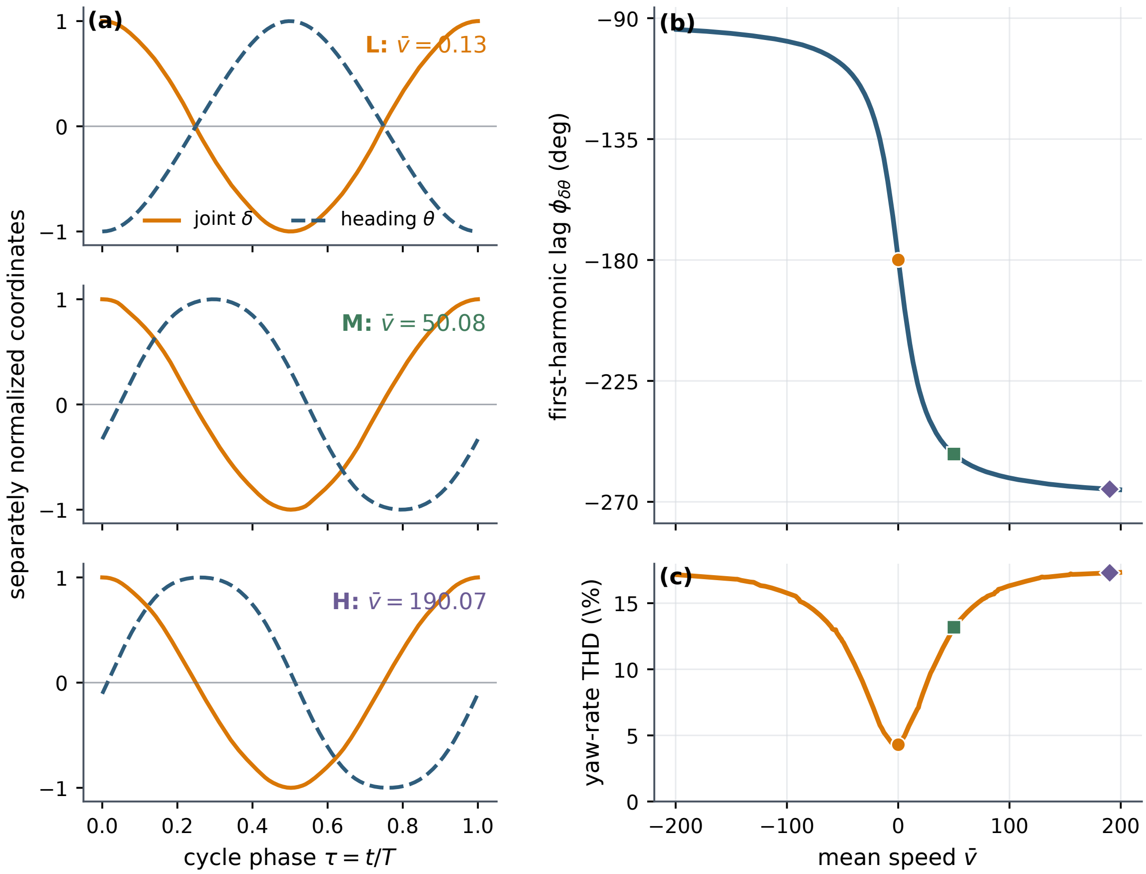

Figure 3.3: The family does not repeat one fixed sinusoidal choreography. (a) Joint angle and reconstructed heading for the L, M, and H members, each shifted to maximum joint angle and normalized separately so that timing can be compared without hiding the amplitude change already reported in Figure 3.2. (b) The continuously unwrapped first-harmonic lag changes across the family; values separated by $360\,\mathrm{deg}$ describe the same wrapped phase. (c) The yaw-rate THD rises from 4.30% for L to 13.18% for M and 17.30% for H. Thus both inter-coordinate phase and harmonic content are branch quantities. The conclusion is specific to this archived 2SEG family and is not a comparison with all possible controlled trajectories.

The pose increment is obtained after the reduced solve:

$$\Delta\theta = \int_0^T \omega(t)\ \mathrm{d}t, \tag{3.29a}$$

$$\Delta x = \int_0^T v(t)\cos\theta(t)\ \mathrm{d}t, \tag{3.29b}$$

$$\Delta y = \int_0^T v(t)\sin\theta(t)\ \mathrm{d}t. \tag{3.29c}$$

Thus reduced return and planar closure are distinct questions. The reported cycles return internally while their reconstructed positions change; for the representative rectilinear motions, the heading increment is close to zero and successive periods extend the same macroscopic direction of travel.

To separate this moving-family statement from a stronger propulsion claim, each cycle is compared with the straight relative equilibrium having the same sampled mean speed and period. With both poses expressed from the same initial carrier frame, define

$$\Delta g_{\mathrm{base}} = \mathrm{Exp}(T[\bar{v}, 0, 0])\,, \qquad \Delta g_{\mathrm{inc}} = \Delta g_{\mathrm{base}}^{-1}\Delta g_{\mathrm{cycle}}. \tag{3.30}$$

The principal group logarithm $\rho_{\mathrm{inc}} = \mathrm{Log}(\Delta g_{\mathrm{inc}})$ records the translation and rotation left after this matched composition. This is a well-defined counterfactual comparison on $\mathrm{SE}(2)$; unlike subtracting $\bar{v}T$ from a world-coordinate path, it remains meaningful when a cycle contains rotation.

Among the 377 rows satisfying $|\bar{v}| \geq 1$, the median translational-log ratio is 0.2603%, its 95th percentile is 7.868%, and 75.33% of the rows lie below 1%; the maximum is 10.88%. Thus, away from near-zero drift, the matched straight contribution typically dominates the archived translation, with speed-dependent exceptions. Near $\bar{v} = 0$ the normalized ratio is deliberately omitted and the absolute increment must be read instead. The result is therefore a family of oscillatory motions riding on and modulating straight translation, not evidence that internal oscillation is the main source of its total displacement.

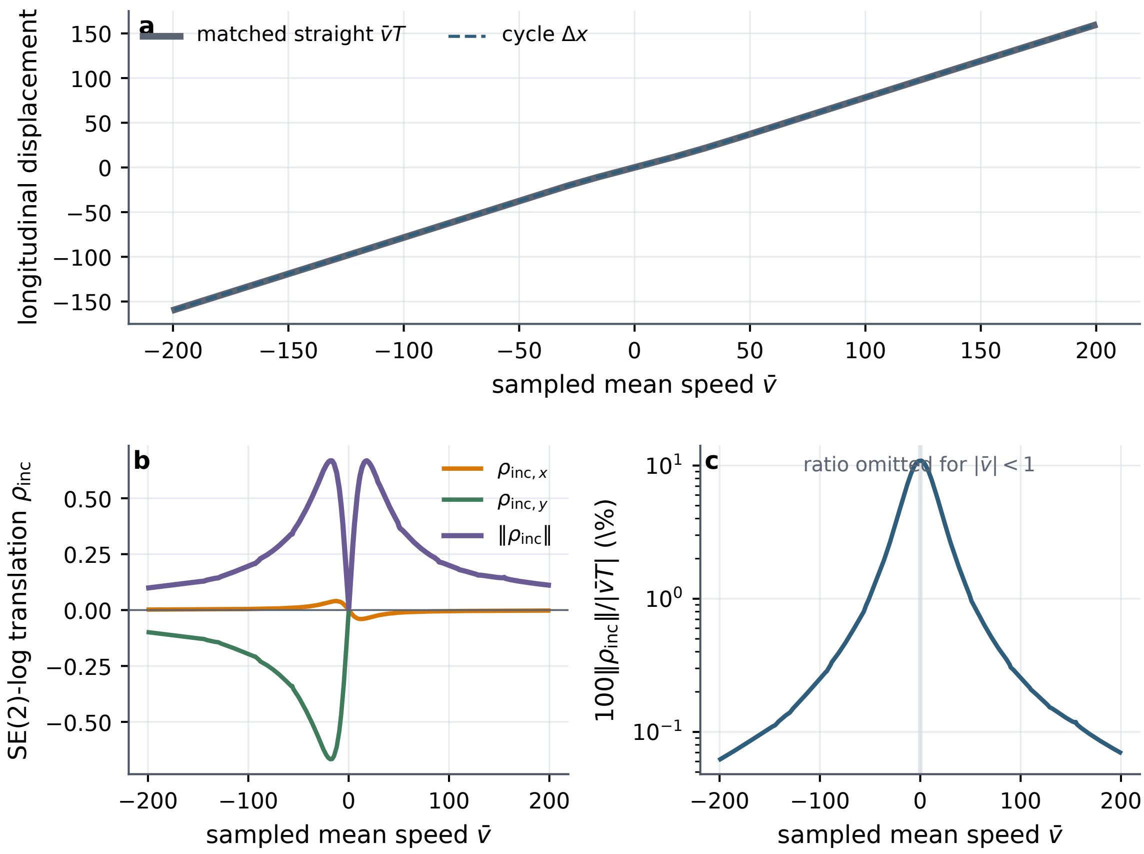

Figure 3.4: Matched-straight pose decomposition over the 379-cycle displayed window. (a) Cycle longitudinal displacement and the matched straight displacement are visually close. (b) The translation of the principal SE(2) logarithm ρ_{inc} resolves their group residual. (c) The normalized residual is reported only for $|\bar{v}| \geq 1$, because a ratio to a vanishing baseline has no useful interpretation. The residual is a reference-dependent modulation, not a unique causal or energetic measure of propulsion.

Chapter 4 independently certifies closure on 29 solved cycles from this family.

3.5 The scalar return coordinate

The full return equation closes four reduced coordinates. Its scalar structure becomes visible on the oriented section

$$\Sigma^+ = \{z : \ \delta = 0, \ \sigma > 0\}. \tag{3.31}$$

Let

$$z_0 = (0, v_0, \omega_0, \sigma_0), \qquad z^+ = (0, v^+, \omega^+, \sigma^+) \tag{3.32}$$

be consecutive crossings of Σ^+. Once the event and the two carrier coordinates satisfy

$$v^+ = v_0, \qquad \omega^+ = \omega_0, \tag{3.33}$$

the remaining return equation is

$$\sigma^+ - \sigma_0 = 0. \tag{3.34}$$

The sign in the section distinguishes the two zero crossings of δ in one oscillation. Chapter 4 shows when this crossing-speed equation is equivalent to zero integrated mechanical exchange, rather than an additional condition imposed on an already closed cycle.

What the reader can now explain

After symmetry reduction, straight translations are reduced equilibria. Their transverse oscillatory eigenpair seeds a finite-amplitude branch of returned states whose period, carrier participation, intercoordinate phase, and harmonic content vary along the family. This is why one scaled sinusoidal choreography cannot replace nonlinear correction and continuation. Their reconstructed poses remain open. A matched group comparison shows that their total translation is usually dominated by straight drift away from the near-zero-speed region, while the oscillatory cycle supplies a smaller, speed-dependent modulation. On the positive joint-crossing section, the only unresolved scalar return is the crossing speed; Chapter 4 derives its exchange interpretation.

Chapter 4

Closed–open exchange and exact scalar return

Energy coordinates on regular scalar sections, nonlinear modal supports, and periodic-orbit return maps are established tools (Arnold, 1989; Shaw and Pierre, 1993; Kuznetsov, 2004). Their boundary for the present locomotor is mechanical interpretation: after the carrier variables are coupled back to the transverse oscillator, what does the last unresolved return coordinate mean? The chapter's precise analytical delta is an exchange–return equivalence on one declared oriented scalar section. It is not a general existence theorem for natural locomotion.

The construction first eliminates the carrier velocities from the kinetic energy and defines a derived auxiliary conservative field. It then restores the original carrier-coupled field. The difference between those two fields changes the transverse storage, and that derivative defines exchange power. Closing is therefore a field replacement after carrier elimination; it is not a physical clamp and not the assignment of one carrier velocity to zero. The ideal no-slip constraint performs no total work, so exchange describes redistribution within the chosen decomposition rather than energy supplied by the constraint.

On the oriented Poincaré section, transverse storage is strictly increasing in the remaining positive crossing speed. Zero integrated exchange and return of that scalar coordinate therefore have exactly the same zero set once the two carrier rows close. The proof is followed by 29 finite-speed numerical realizations and an independent comparison with the continued family of Chapter 3. In higher transverse dimension, one storage value leaves a level set rather than identifying a returned state.

4.1 The return coordinate to be replaced

Recall the pose-reduced state

$$z = (\delta, v, \omega, \sigma), \qquad \sigma = \dot{\delta}, \tag{4.1}$$

where v is the body-forward speed and ω is the carrier yaw rate. The body pose $g = (x, y, \theta) \in \mathrm{SE}(2)$ is reconstructed from

$$\dot{x} = v\cos\theta, \qquad \dot{y} = v\sin\theta, \qquad \dot{\theta} = \omega. \tag{4.2}$$

A relative-periodic locomotor motion closes z after a period T while allowing $g(T) = g(0)\Delta g$ with $\Delta g \neq e$. The group displacement is an output of the returned reduced motion; it is not included in the return residual.

A Poincaré formulation removes the arbitrary time origin of a periodic orbit (Kuznetsov, 2004). On the section $\delta = 0$, the first return has three nontrivial coordinates. The residual used here imposes direct return of the two carrier coordinates and replaces the crossing-speed defect by an exchange integral, after fixing the section orientation, storage, and carrier-coupled field.

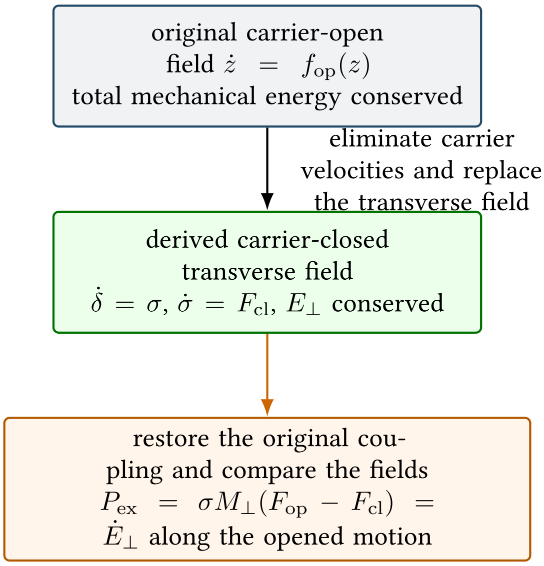

Figure 4.1: Mechanical meaning of the closed–open construction. The closed field is a derived auxiliary conservative field, not a clamped version of the mechanism. Exchange is the transverse-storage change caused by restoring the original coupling; total mechanical energy remains conserved in the opened ideal model.

Shooting and pseudo-arclength continuation find zeros of a supplied residual (Peeters et al., 2009). The analytical result below identifies the power-balance row with one coordinate of the section return for this scalar transverse problem.

4.2 Closing the carrier channel

Figure 4.1 gives the complete logic before the coefficient-level derivation. The opened locomotor conserves its total mechanical energy, but the derived transverse share need not remain constant. The auxiliary closed field is defined so that this transverse storage is conserved. Reopening restores exactly the coupling whose field difference accounts for its change.

4.2.1 Schur-complement storage

In admissible velocities $\eta = (v, \omega, \sigma)^\mathsf{T}$, the kinetic energy of the dimensionless two-segment model is

$$K(\delta, \eta) = \frac{1}{2}\eta^\mathsf{T} M(\delta)\eta, \tag{4.3}$$

with

$$M(\delta) = \begin{bmatrix} 1 & -\rho & -\rho \\ -\rho & B_{11} & B_{12} \\ -\rho & B_{12} & B_{22} \end{bmatrix}. \tag{4.4}$$

The functions $\rho(\delta)$, $B_{11}(\delta)$, and $B_{12}(\delta)$, and the constant B_{22}, were derived in Chapter 3. For the reference design,

$$B_{11} = j_1 + j_2 + \alpha^2 + \mu\beta^2 + 2\mu\alpha\beta\cos\delta, \tag{4.5}$$

$$B_{12} = j_2 + \mu\beta^2 + \mu\alpha\beta\cos\delta, \tag{4.6}$$

$$B_{22} = j_2 + \mu\beta^2, \qquad \rho = \mu\beta\sin\delta. \tag{4.7}$$

The complete dimensional derivation and parameter table are collected in Appendix A.

Partition the velocities into the carrier pair $y = (v, \omega)^{\mathsf{T}}$ and the scalar shape rate σ:

$$M = \begin{bmatrix} M_{cc} & m_{c\sigma} \\ m_{c\sigma}^{\mathsf{T}} & B_{22} \end{bmatrix}, \quad M_{cc} = \begin{bmatrix} 1 & -\rho \\ -\rho & B_{11} \end{bmatrix}, \quad m_{c\sigma} = \begin{bmatrix} -\rho \\ B_{12} \end{bmatrix}. \tag{4.8}$$

When

$$\Delta(\delta) = \det M_{cc} = B_{11} - \rho^2 > 0, \tag{4.9}$$

the carrier block can be eliminated at fixed (δ, σ). Minimizing K over y gives $y_* = -M_{cc}^{-1} m_{c\sigma}\sigma$ and the effective transverse inertia

$$M_\perp(\delta) = B_{22} - m_{c\sigma}^{\mathsf{T}} M_{cc}^{-1} m_{c\sigma} = B_{22} - \frac{B_{12}^2 + \rho^2(B_{11} - 2B_{12})}{\Delta}. \tag{4.10}$$

Positive definiteness of the admissible kinetic energy implies $M_\perp > 0$ wherever M and M_{cc} are positive definite.

With the internal potential

$$U(\delta) = \frac{1}{2}k_2\delta^2 + \frac{1}{4}k_4\delta^4, \qquad k_2 = 1, \quad k_4 = 10, \tag{4.11}$$

the scalar transverse storage is

$$\boxed{E_\perp(\delta, \sigma) = \frac{1}{2}M_\perp(\delta)\sigma^2 + U(\delta).} \tag{4.12}$$

This is not the total energy of the locomotor. It is the kinetic-plus-potential storage left by the Schur complement after the carrier velocities have been eliminated.

4.2.2 The closed transverse field

The auxiliary carrier-closed field evolves (δ, σ) with $E_\perp$ conserved. Differentiating Equation (4.12) gives

$$\dot{E}_\perp = \sigma\left(M_\perp\dot\sigma + \frac{1}{2}M_\perp'\sigma^2 + U'\right). \tag{4.13}$$

The closed field is therefore

$$\dot\delta = \sigma, \qquad \dot\sigma = F_{\mathrm{cl}}(\delta, \sigma) = -\frac{U'(\delta) + \frac{1}{2}M_\perp'(\delta)\sigma^2}{M_\perp(\delta)}. \tag{4.14}$$

At a regular energy E, its two branches are

$$\sigma_\pm(\delta; E) = \pm\sqrt{\frac{2(E - U(\delta))}{M_\perp(\delta)}}, \tag{4.15}$$

between the turning points $U(\delta_\pm) = E$. Period and action follow from one-dimensional quadratures,

$$\frac{T_{\mathrm{cl}}(E)}{2} = \int_{\delta_-}^{\delta_+} \sqrt{\frac{M_\perp(\delta)}{2(E - U(\delta))}}\,\mathrm{d}\delta, \tag{4.16}$$

$$J_{\mathrm{cl}}(E) = \frac{1}{\pi}\int_{\delta_-}^{\delta_+} \sqrt{2M_\perp(\delta)(E - U(\delta))}\,\mathrm{d}\delta. \tag{4.17}$$

These quantities parameterize and seed the closed support. They do not yet describe an opened locomotor cycle. The regular level and the oriented crossing used below are shown in Figure 4.2.

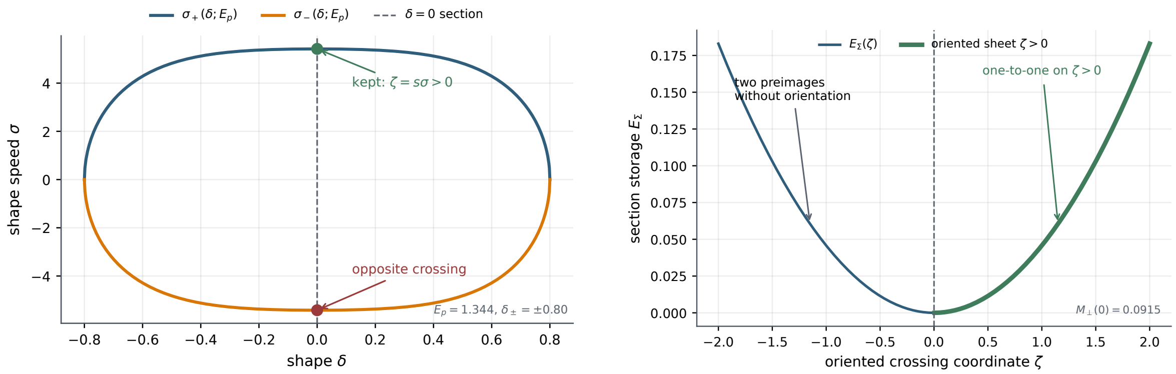

(a) A regular level of the closed transverse storage.

(b) Storage is one-to-one on the positive oriented crossing sheet.

Figure 4.2: The scalar geometry used by the return theorem. The closed level supplies a smooth annulus and an initial scale; the oriented section removes the half-period ambiguity and makes transverse storage one-to-one in the crossing speed.

4.3 Reopening the carrier channel

4.3.1 Canonical finite-speed field

The full reduced dynamics couples shape acceleration to the carrier through the product

$$q_y = v\omega. \tag{4.18}$$

Solving the reduced equations for $\dot{\sigma}$ gives the canonical opened field,

$$\boxed{F_{\mathrm{op}}(\delta,\sigma,v,\omega) = \frac{r(\delta)\big[q_y - \rho(\delta)(\sigma+\omega)^2\big] - U'(\delta)}{M_\perp(\delta)},} \tag{4.19}$$

where

$$r(\delta) = \frac{A_q(\delta)}{\Delta(\delta)} \tag{4.20}$$

and A_q is the coefficient obtained when the carrier block is eliminated from the raw equations. Appendix B records the remaining transport rows and the equation-to-code regression.

The distinction between Equations (4.14) and (4.19) fixes the convention used throughout this thesis. In particular, the metric derivative is part of F_{cl} but is not inserted into F_{op}. The exchange force is the difference of the two fields:

$$M_\perp(F_{\mathrm{op}} - F_{\mathrm{cl}}) = r\{q_y - \rho(\sigma+\omega)^2\} + \frac{1}{2}M_\perp'\sigma^2. \tag{4.21}$$

Thus closing the channel means replacing the opened field by the conservative field. It is not equivalent to setting only q_y or ω to zero in Equation (4.19).

Multiplication by the shape rate identifies the instantaneous transverse exchange power,

$$\boxed{P_{\mathrm{ex}} = \sigma M_\perp(F_{\mathrm{op}} - F_{\mathrm{cl}}) = \sigma\left[r\{q_y - \rho(\sigma+\omega)^2\} + \frac{1}{2}M_\perp'\sigma^2\right].} \tag{4.22}$$

Substitution of the opened field into the derivative of Equation (4.12) yields the exact identity

$$\boxed{\dot{E}_\perp = P_{\mathrm{ex}}.} \tag{4.23}$$

The integrated exchange along any regular opened segment is consequently

$$I_{\mathrm{ex}} = \int_0^T P_{\mathrm{ex}}(t)\,\mathrm{d}t = E_\perp(T) - E_\perp(0). \tag{4.24}$$

Because the transverse crossing-speed defect is omitted from the numerical residual, (4.24) supplies that scalar return row through the exchange balance.

4.3.2 Finite-speed and orientation chart

Let the prescribed nonzero mean speed be $\bar{v}$ and set

$$h = |\bar{v}|^{-1}, \qquad s = \operatorname{sgn}(\bar{v}), \qquad \nu = hv, qquadq_y = v\omega. \tag{4.25}$$

The inverse relations are

$$v = \frac{\nu}{h}, \qquad \omega = \frac{hq_y}{\nu}, \tag{4.26}$$

so the chart requires $\nu \neq 0$. It keeps q_y finite as $h \to 0$ and separates the large forward speed from the smaller yaw rate.

Positive and negative mean-speed branches are placed on one oriented sheet with

$$Y = (\delta, \zeta, u, Q), \qquad \sigma = s\zeta, \quad \nu = su, \quad q_y = sQ, \tag{4.27}$$

and oriented time ϑ defined by $\mathrm{d}/\,\mathrm{d}\vartheta = s\ \mathrm{d}/\,\mathrm{d}t$. Then $\mathrm{d}\delta/\,\mathrm{d}\vartheta = \zeta$, and both speed directions use the section

$$\Sigma = \{Y : \delta = 0,\ \zeta > 0,\ u > 0\}. \tag{4.28}$$

The full oriented field has the form

$$\frac{\mathrm{d}Y}{\mathrm{d}\vartheta} = \big(\zeta, F_{\mathrm{op}}, F_u, F_Q\big), \tag{4.29}$$

where F_u and F_Q are algebraic transforms of the raw carrier equations. Their equation-to-code comparison is reported in Appendix B.

4.4 Exact scalar exchange–return equivalence

Let $Y_0 = (0, \zeta_0, u_0, Q_0) \in \Sigma$ and let

$$Y^+ = (0, \zeta^+, u^+, Q^+) \tag{4.30}$$

be the next crossing of the same oriented section. The section storage depends on one coordinate:

$$E_\Sigma(\zeta) = E_\perp(0, s\zeta) = \frac{1}{2}M_\perp(0)\zeta^2 + U(0). \tag{4.31}$$

Since $M_\perp(0) > 0$ and $\zeta > 0$,

$$\frac{\mathrm{d}E_\Sigma}{\mathrm{d}\zeta} = M_\perp(0)\zeta > 0. \tag{4.32}$$

Orientation is essential: without it, the two crossing directions $\pm\zeta$ would have the same storage.

Assumption 4.1 (regular scalar return domain)**.** The opened orbit remains in a domain on which $\Delta > 0$, $M_\perp > 0$, u is bounded away from zero, and the finite-speed field is regular. The flow crosses Equation (4.28) transversely and has a well-defined next return on the same oriented sheet. The corresponding closed levels form a regular annulus with no separatrix or turning-point singularity.

Theorem 4.2 (scalar exchange–return equivalence)**.** *Under Assumption 4.1, the integrated exchange and the transverse crossing-speed defect are equivalent:*

$$I_{\mathrm{ex}} = 0 \quad \Longleftrightarrow \quad \zeta^{+} = \zeta_0. \tag{4.33}$$

Consequently, if $u^{+} = u_0$ *and* $Q^{+} = Q_0$ *are imposed directly, the residual row* $I_{\mathrm{ex}} = 0$ *completes the pose-reduced return on* Σ.

Proof. By Equation (4.24), $I_{\mathrm{ex}} = 0$ is equivalent to $E_{\perp}(T) = E_{\perp}(0)$. Both endpoints lie at $\delta = 0$ on the same oriented sheet, hence

$$E_{\Sigma}(\zeta^{+}) = E_{\Sigma}(\zeta_0). \tag{4.34}$$

The strict monotonicity of Equation (4.31) on $\zeta > 0$ gives $\zeta^{+} = \zeta_0$. Conversely, equality of the crossing speeds makes the endpoint transverse storages equal, so Equation (4.24) gives $I_{\mathrm{ex}} = 0$. □

The theorem identifies the zero set of one return row. The numerical roots below establish its realization on the tested finite-speed corridor; higher-dimensional sections require additional return information.

On a higher-dimensional section, equality of one storage value defines a level set rather than identifying the endpoint. Full vector return must then be imposed directly, and modal metrics separately classify the returned cycle.

4.5 A computable exchange residual

For fixed $\bar{v} \neq 0$, write the initial section point as

$$Y_0 = (0, e^{a}, e^{b}, Q_0). \tag{4.35}$$

The logarithmic coordinates enforce $\zeta_0 > 0$ and $u_0 > 0$. The opened field is integrated to the next event Equation (4.28), together with two accumulators,

$$\frac{\mathrm{d}I_{\mathrm{ex}}}{\mathrm{d}\vartheta} = sP_{\mathrm{ex}}, \qquad \frac{\mathrm{d}I_{u}}{\mathrm{d}\vartheta} = u. \tag{4.36}$$

The factor s expresses physical-time exchange power in oriented time. For $s = -1$ the numerical orbit represents a backward physical-time traversal; its cycle integral changes sign relative to the forward traversal but has the same zero set. The overdetermined shooting residual is

$$\boxed{\mathcal{R}_{\mathrm{ex}}(Y_0; \bar{v}) = \begin{bmatrix} I_{\mathrm{ex}}(T) \\ u(T) - u_0 \\ Q(T) - Q_0 \\ T^{-1} I_u(T) - 1 \end{bmatrix}.} \tag{4.37}$$

The first three rows close the reduced section state by Theorem 4.2; the fourth fixes the mean-speed gauge introduced by $h = |\bar{v}|^{-1}$. At fixed $\bar{v}$ there are three free initial coordinates and four reported rows, so the formulation is overdetermined. All four scaled rows are minimized simultaneously by nonlinear least squares, and every accepted root satisfies their common tolerance.

In the computation, a regular closed-support cycle supplies the initial scale. The carrier channel is restored, the opened field is integrated to the next oriented crossing, and the exchange and two carrier-return rows are solved simultaneously. Acceptance requires the section event, the regular-domain checks, and all four scaled residual rows to pass. Comparison with the continuation of Chapter 3 is then an independent test of branch placement, not part of the residual definition.

Table 4.1: Representative exchange-return rows and comparison with the independent continued family. Errors are absolute; the geometry column is a scaled RMS distance after cyclic phase and traversal alignment.

$\bar{v}$	$\lVert\mathcal{R}_{\mathrm{ex}}\rVert$	period error	$\delta_{\max}$ error	geometry RMS
-24.871	1.80×10^{-15}	4.72×10^{-6}	9.19×10^{-7}	3.07×10^{-3}
-10.162	9.72×10^{-15}	6.64×10^{-7}	5.13×10^{-6}	2.04×10^{-3}
-0.897	5.52×10^{-13}	3.85×10^{-7}	1.99×10^{-6}	1.90×10^{-3}
1.133	2.99×10^{-15}	6.02×10^{-7}	3.55×10^{-6}	1.99×10^{-3}
10.274	6.38×10^{-14}	8.19×10^{-6}	6.64×10^{-6}	2.06×10^{-3}
25.088	1.76×10^{-15}	1.50×10^{-5}	1.86×10^{-5}	2.81×10^{-3}

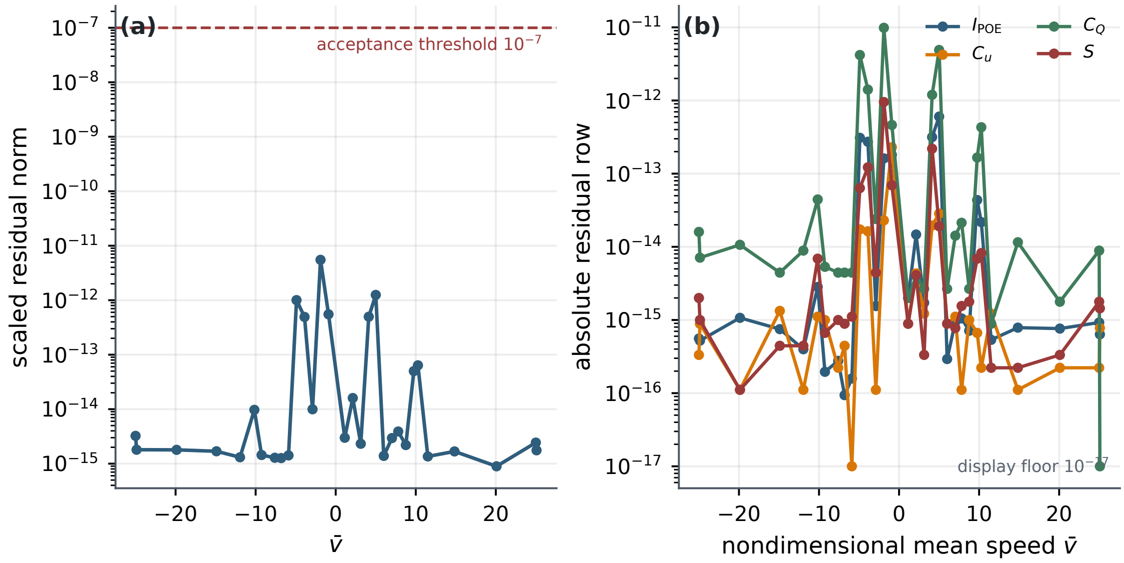

Figure 4.3: Closure of the exchange and carrier-return rows over the 29 accepted cycles. The left panel reports the scaled residual norm; the right panel separates its four absolute components.

4.6 Numerical realization

4.6.1 Returned family

The numerical data contain 29 accepted rows spanning both signs of the central finite-speed corridor. Every row closes Equation (4.37); the largest scaled residual norm is

$$5.51\times10^{-12}. \tag{4.38}$$

The largest mismatch between the requested $\bar{v}$ and the nearest independently continued reference speed is 7.35×10^{-11}. Representative rows are listed in Table 4.1; aggregate comparison bounds and independent event/domain checks are provided in Appendix B.

Across all 29 rows, the maximum absolute errors are 1.50×10^{-5} for period, 1.86×10^{-5} for maximum shape amplitude, and 8.36×10^{-4} for maximum yaw-rate amplitude. The maximum phase-aligned scaled RMS loop distance in the canonical comparison summary is 3.07×10^{-3}. Time-sample differences are not used because two representations of the same periodic orbit may choose different origins and traversal directions. Figures 4.3 and 4.4 show, respectively, the residual decomposition and representative phase-aligned loop comparisons.

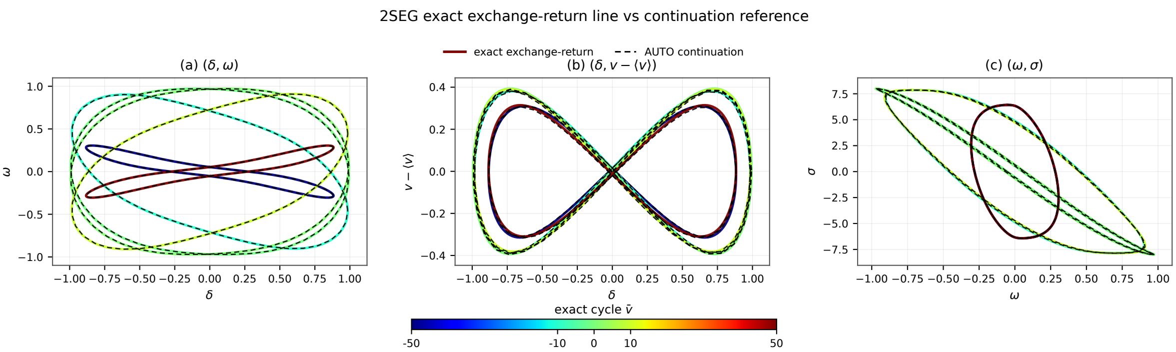

Figure 4.4: Exchange–return cycles (solid colored curves) and independently continued reference loops (black dashed curves) at representative mean speeds. Agreement is evaluated after cyclic-phase and traversal alignment.

4.7 Dimensional boundary of the scalar result

The closed–open operation itself extends beyond one transverse coordinate: one can eliminate carrier directions, construct a reduced storage or modal support, restore the carrier coupling, and evaluate return and exchange. The equivalence in Theorem 4.2 does not extend by notation alone. Its decisive step is the injective map

$$\zeta \mapsto E_\Sigma(\zeta) \tag{4.39}$$

on a one-dimensional oriented section.

For a transverse state $w \in \mathbb{R}^m$ with $m > 1$, the equation $E_\perp(w^+) = E_\perp(w_0)$ generally leaves an $(m-1)$-dimensional set of possible endpoints. Exchange still measures storage transfer between transverse and carrier directions. Full vector return then establishes exact reduced return, while modal metrics distinguish the returned organization in the three-segment model.

What the reader can now explain

The carrier-closed field is an auxiliary conservative transverse dynamics derived after carrier elimination; reopening restores the original coupled locomotor equations. Their difference gives the exact derivative of the transverse storage. On the regular positive scalar section, that storage is injective in the remaining crossing speed, so zero integrated exchange replaces that final return row once the carrier rows close. The argument depends on the one-dimensional section and therefore does not turn one scalar balance into a vector return theorem.

Chapter 5

Modal natural-locomotion families in the three-segment model

Closest antecedent. Chapter 4 established a scalar result for 2SEG: after the other return rows and an oriented crossing have been fixed, equality of a strictly monotone transverse storage identifies the remaining crossing coordinate. Integrated exchange can then replace that last scalar return row.
Precise boundary. The 3SEG mechanism has two transverse joint coordinates. One storage value defines a level set rather than one endpoint, so exchange cannot replace full return. Moreover, the population re-audit begins with the final opened cycle files; it does not reconstruct, for every archived row, the genealogy from a particular carrier-closed support through the state bridge.
Chapter delta. At one fixed numerical model-parameter vector, the opened calculation imposes six-component reduced return and yields two moving branch chains. Modal metrics evaluated after return classify them as in-phase (IP) and anti-phase (AP). Exchange is then an identity-based balance diagnostic. A matched straight $SE(2)$ decomposition further separates the reconstructed pose increment from a counterfactual with the same mean speed and period, without assigning a unique causal or energetic meaning to the residual.

5.1 Why one storage value cannot identify the endpoint

After the carrier rows have returned, let w collect the unresolved coordinates on an oriented section. In the scalar case, $w = \zeta > 0$, and strict monotonicity of the section storage makes endpoint storage injective. For $w \in \mathbb{R}^m$, $m > 1$,

$$E_\Sigma(w^+) = E_\Sigma(w_0) \quad \Longrightarrow \quad w^+ \in E_\Sigma^{-1}(E_\Sigma(w_0)) \,, \tag{5.1}$$

and a regular level set is generally $(m-1)$-dimensional. Equality of one scalar storage therefore constrains the endpoint but does not determine it.

For example,

$$E_\Sigma(w_1, w_2) = \frac{1}{2}\left(\kappa_1 w_1^2 + \kappa_2 w_2^2\right), \qquad \kappa_1, \kappa_2 > 0, \tag{5.2}$$

assigns the same value to $(a, 0)$ and $(0, a\sqrt{\kappa_1/\kappa_2})$, although the points lie on different modal axes. Choosing one crossing orientation removes a sign ambiguity; it does not collapse the ellipse to a point.

This dimensional obstruction fixes the order of the chapter's claims. Full vector return first qualifies a reduced cycle. Modal metrics subsequently classify the returned motion as IP or AP. Once return is known, equality of endpoint transverse storage makes zero cycle-mean exchange an identity and a numerical consistency check, not a third independent selector.

5.2 Mechanism and reduced conservative field

5.2.1 Configuration, state, and pose reconstruction

The 3SEG mechanism consists of a constrained carrier, a middle segment, and a distal segment. Its two relative angles are $\boldsymbol{\delta} = (\delta_1, \delta_2)^\mathsf{T}$: δ_1 is measured from the carrier to the middle segment and δ_2 from the middle to the distal segment.

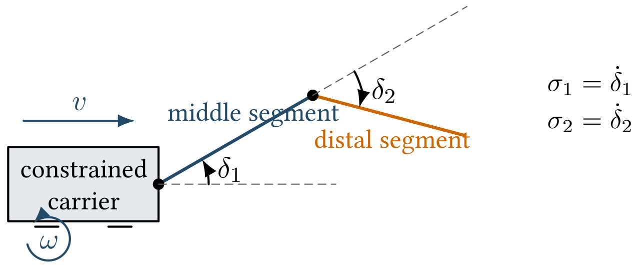

Figure 5.1: Coordinates of the 3SEG mechanism. Each joint angle is relative to the preceding segment. The carrier moves forward at speed v, yaws at rate ω, and cannot slip laterally. Complete centre-of-mass definitions are given in Appendix C.

The configuration, admissible velocity, and pose-reduced state are

$$q = (g, \boldsymbol{\delta}), \qquad g = (x, y, \theta) \in \mathrm{SE}(2), \qquad \xi = (v, \omega, \sigma_1, \sigma_2)^\mathsf{T}, \tag{5.3}$$

$$z = (\delta_1, \delta_2, v, \omega, \sigma_1, \sigma_2)^\mathsf{T}. \tag{5.4}$$

The no-side-slip constraint removes lateral carrier velocity. Once $z(t)$ has been computed, the planar pose is reconstructed from

$$\dot{x} = v\cos\theta, \qquad \dot{y} = v\sin\theta, \qquad \dot{\theta} = \omega. \tag{5.5}$$

Return is imposed on all six components of z; the pose is left open and reported through $\Delta g = g(0)^{-1}g(T)$.

5.2.2 Unforced equations and total energy

The joints have local quadratic–quartic springs and a weak quadratic coupling,

$$\begin{aligned} U(\boldsymbol{\delta}) = {}& \frac{1}{2}k_{2,1}\delta_1^2 + \frac{1}{4}k_{4,1}\delta_1^4 + \frac{1}{2}k_{2,2}\delta_2^2 + \frac{1}{4}k_{4,2}\delta_2^4 \\ & + \frac{1}{2}k_{12}(\delta_1 - \delta_2)^2. \end{aligned} \tag{5.6}$$

With $\sigma = (\sigma_1, \sigma_2)^\mathsf{T}$ and $\eta = (v, \omega)^\mathsf{T}$, the unforced reduced equations are

$$\dot{\boldsymbol{\delta}} = \sigma, \qquad M(\boldsymbol{\delta})\begin{bmatrix}\dot{\eta}\\ \dot{\sigma}\end{bmatrix} + c(\boldsymbol{\delta}, \eta, \sigma) + \begin{bmatrix}0\\0\\ \nabla U(\boldsymbol{\delta})\end{bmatrix} = 0. \tag{5.7}$$

The exact geometry, kinetic energy, mass matrix, and velocity-dependent vector are given in Appendix C. The ideal constraint does no total work, so

$$E(z) = \frac{1}{2}\xi^\mathsf{T} M(\boldsymbol{\delta})\xi + U(\boldsymbol{\delta}) \tag{5.8}$$

is conserved by this unforced field. The numerical parameter values used below are coordinates of one archived model and carry no assigned physical units.

5.3 Closed supports, modal seeds, and the state bridge

5.3.1 Carrier-closed transverse storage

Partition the mass matrix between carrier velocity η and joint velocity σ:

$$M = \begin{bmatrix} M_{GG} & M_{GS} \\ M_{SG} & M_{SS} \end{bmatrix}. \tag{5.9}$$

Eliminating the energy-minimizing carrier velocity gives the Schur-complement inertia and transverse storage

$$M_\perp = M_{SS} - M_{SG} M_{GG}^{-1} M_{GS}, \qquad E_\perp(\boldsymbol{\delta}, \sigma) = \frac{1}{2} \sigma^\mathsf{T} M_\perp(\boldsymbol{\delta}) \sigma + U(\boldsymbol{\delta}). \tag{5.10}$$

On the domain used here, $M_\perp$ is positive definite. The carrier-closed auxiliary system is the conservative two-joint Euler–Lagrange system generated by $E_\perp$. Its periodic solutions are called closed supports.

5.3.2 Local IP and AP seeds

At the straight configuration, the mass-normalized eigenproblem is

$$K_0 u_j = \Omega_j^2 M_0 u_j, \qquad u_i^\mathsf{T} M_0 u_j = \delta_{ij}, \qquad j \in \{\mathrm{IP}, \mathrm{AP}\}, \tag{5.11}$$

with $M_0 = M_\perp(0)$ and $K_0 = D^2 U(0)$. The entries of u_{IP} have the same sign; those of u_{AP} have opposite signs. These eigenvectors provide local tangent directions for the closed-support families, not finite-amplitude trajectories. Continuation is needed because period, waveform, and modal mixture change away from the straight configuration (Kerschen et al., 2009; Peeters et al., 2009).

5.3.3 Bridge into the opened state

The energy-minimizing carrier velocity and its complementary coordinate are

$$\eta_\perp = -M_{GG}^{-1} M_{GS} \sigma, \qquad q_c = \eta - \eta_\perp. \tag{5.12}$$

A closed support is lifted with $q_c = 0$, after which the opened correction allows q_c to vary and solves the full field Equation (5.7). Here $q_c = 0$ is a coordinate choice in the derived decomposition; it is not a physical clamp and is not obtained by naively setting one world velocity to zero.

The archived construction followed

$$\begin{aligned} &\text{linear seed} \longrightarrow \text{closed support} \longrightarrow \text{bridged candidate} \\ &\qquad\qquad \longrightarrow \text{corrected opened cycle} \longrightarrow \text{fixed-parameter branch.} \end{aligned} \tag{5.13}$$

Multiple shooting and collocation corrected the opened candidates, and pseudo-arclength continuation organized neighboring cycles. This chain describes how the archive was generated. The population audit used in this chapter independently reopens the final cycle files but does not contain the closed-support projection. It therefore does not establish a population-wide one-to-one genealogy from a particular closed support, through the bridge, to every final row.

5.4 Opened cycles: vector return, modal classification, and exchange

5.4.1 Qualification by the full reduced field and vector return

Let $\Phi_{p_*}^T$ be the flow of the opened unforced field at the common parameter vector p_*. A corrected relative-periodic cycle satisfies the six-component residual

$$R_z(z_0, T) = \Phi_{p_*}^T(z_0) - z_0 = 0 \in \mathbb{R}^6. \tag{5.14}$$

Pose does not appear in this equality; it is reconstructed afterwards. Full vector return is the exact reduced-return statement. Neither modal identity nor exchange replaces a component of R_z in this model.

The raw-field defect supplies an additional numerical check. A periodic spline is fitted through the sampled state, differentiated away from its seam, and compared with the exact right-hand side:

$$R_{\mathrm{rhs,int}} = \max_{\text{trimmed samples}} \left\| \dot{z}_{\mathrm{spl}} - f(z) \right\|_{\infty}. \tag{5.15}$$

This sampled consistency metric distinguishes a geometrically closed data curve from one that also follows the declared mechanical field to the reported tolerance.

5.4.2 Classification after return

The linear eigenvectors define modal coordinates on each complete finite-amplitude cycle,

$$Q_j(t) = u_j^{\mathsf{T}} M_0 \boldsymbol{\delta}(t), \qquad \widetilde{P}_j(t) = \frac{u_j^{\mathsf{T}} M_0 \sigma(t)}{\Omega_j}. \tag{5.16}$$

Their time-weighted activity is

$$A_j = \left[\frac{1}{T} \int_0^T \left(Q_j(t)^2 + \widetilde{P}_j(t)^2 \right) \mathrm{d}t \right]^{1/2}. \tag{5.17}$$

The classification uses the expected-sector share $A_j/(A_{\mathrm{IP}} + A_{\mathrm{AP}})$, the expected/opposite activity ratio, and time-weighted correlations of the two joint positions and rates. Positive correlations identify the IP sense; negative correlations identify the AP sense. The thresholds and exact modal vectors are listed in Appendix C.

These metrics describe the organization of a cycle that has already returned. They do not supply exact return, and they do not prove the existence of a global invariant modal manifold.

5.4.3 Exchange after full return

Along any opened trajectory,

$$P_{\mathrm{ex}} = \frac{\mathrm{d}E_{\perp}}{\mathrm{d}t}, \qquad \overline{P}_{\mathrm{ex}} = \frac{1}{T} \int_0^T P_{\mathrm{ex}}\, \mathrm{d}t = \frac{E_{\perp}(T) - E_{\perp}(0)}{T}. \tag{5.18}$$

Positive and negative instantaneous values record redistribution between the carrier and transverse storage under the derived decomposition. If the full state returns, then $(\boldsymbol{\delta}(T), \sigma(T)) = (\boldsymbol{\delta}(0), \sigma(0))$, so $\overline{P}_{\mathrm{ex}} = 0$ follows from the endpoint identity. Its reported numerical value tests storage consistency; it is not an independent qualification or classification row.

The cycle-mean body-forward speed,

$$\bar{v} = \frac{1}{T} \int_0^T v(t)\, \mathrm{d}t, \tag{5.19}$$

is used below to compare the two modal sectors and to construct a matched straight pose reference.

5.4.4 One returned cycle through the claim pipeline

Before counting archived rows, it is useful to follow the status of one final cycle. The carrier-closed support and state bridge explain how a candidate was generated. The retained opened cycle is then checked against the full field and vector return; only after that qualification are modal identity, exchange, and pose evaluated.

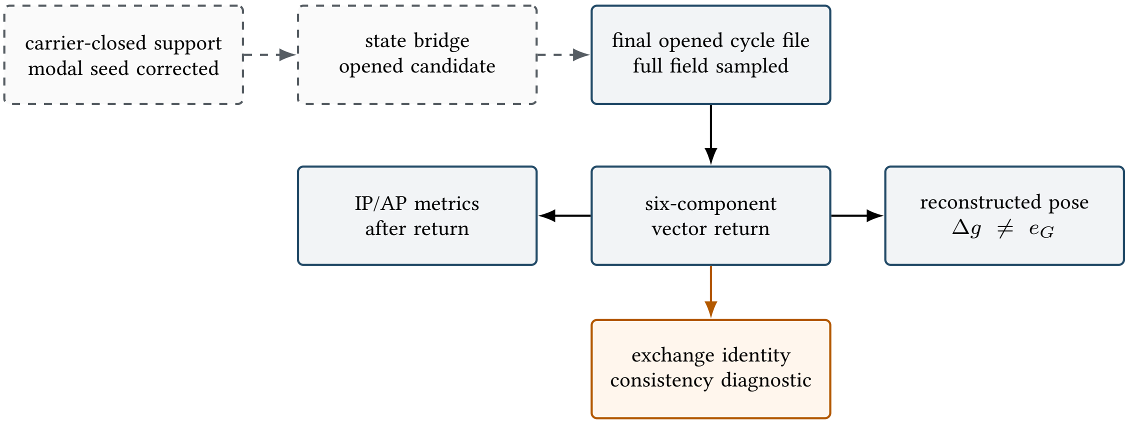

Figure 5.2: Status of a representative final cycle. Dashed boxes reproduce the archived generation route; their one-to-one genealogy was not re-audited for every population member. Solid boxes are the checks applied to final opened cycle files. Modal identity classifies an already-returned cycle, while exchange is a consequence and diagnostic of that return.

5.5 Same-parameter returned AP and IP populations

The two branch archives contain

$$N_{\mathrm{AP}} = 2278, \qquad N_{\mathrm{IP}} = 1358 \tag{5.20}$$

opened cycles at the same numerical model-parameter vector p_*. The AP chain has 1,139 rows on each signed continuation side; the IP chain has 679 on each side. These are dense samples along two computed branch chains, not independent replications.

Every final cycle file was reopened to recompute endpoint return, time-weighted modal identity, and pose reconstruction. Stored exchange and raw-field diagnostics were collected from the branch summary that generated the population. The resulting scope is precise: the rows below audit final opened cycles and their modal classification; they do not audit the entire closed-support-to-bridge genealogy for every population member.

Table 5.1: Audited properties of the two opened sectors at the same numerical parameter vector p_*. Endpoint zeros mean equality at the precision stored in the cycle files. Exchange is shown as a diagnostic after return.

Quantity	AP	IP
returned cycle files	2,278	1,358
maximum endpoint defect	0	0
time-weighted sector-identity passes	2,278/2,278	1,358/1,358
maximum interior raw-field defect	1.102×10^{-3}	1.502×10^{-3}
maximum $\lvert \overline{P}_{\mathrm{ex}} \rvert$	1.692×10^{-8}	2.764×10^{-8}
reconstructed displacement-magnitude range	$[3.038 \times 10^{-3},\ 79.923]$	$[5.563 \times 10^{-2},\ 143.562]$
maximum reconstructed $\lvert \Delta\theta \rvert$	5.96×10^{-9}	2.48×10^{-7}
mean-speed span	$[-126.956,\ 122.793]$	$[-155.563,\ 166.114]$

The population establishes coexistence of returned, moving AP and IP branch chains at p_*. All stored cycles pass their declared sector gates, and their reconstructed pose increments are nonzero at the resolution reported. The statement does not include stability, exhaustive branch classification, a global manifold theorem, or a hardware-identification result.

5.6 Finite-amplitude contrast between the sectors

A fixed display sample of 72 cycles from each sector covers both speed signs and several scales of $|\bar{v}|$. It is an illustration of the archived branches, not a population-weighted statistic. Internal activity is the largest peak-to-peak range among $\delta_1, \delta_2, \omega, \sigma_1, \sigma_2$, excluding forward speed.

Table 5.2: Finite-amplitude contrast in the fixed 72-cycle display sample from each sector.

Quantity	AP sample	IP sample
period	0.5563–0.6295	0.8452–0.8642
internal peak-to-peak activity	52.23–84.43	4.915–5.388
time-weighted expected-sector share	0.6925–0.8136	0.9633–0.9670
expected/opposite activity ratio	2.252–4.364	26.284–29.275
joint-position correlation	−0.99991–−0.99959	0.9147–0.9293
joint-rate correlation	−0.99915–−0.99630	0.5642–0.6141

AP is the shorter-period, higher-activity organization. Its two joints remain almost perfectly opposed, while the finite-amplitude motion has more activity in the opposite linear coordinate than the IP sector does. IP is longer-period, lower-activity, and more concentrated near its same-direction linear seed. Representative traces make the distinction visible.

5.7 Matched-straight pose decomposition

A nonzero pose increment shows that a returned cycle moves the mechanism, but it does not isolate the effect of its internal oscillation. A carrier with the same nonzero mean speed would already translate during the same period. The matched-straight ablation separates these two group increments without modifying the archived reduced trajectory.

For every cycle, pose is reconstructed from Equation (5.5) with $g(0) = e_G$. The counterfactual is the straight relative equilibrium with the same sampled time-weighted mean speed and period:

$$\Delta g_{\text{base}} = \mathrm{Exp}_{\mathrm{SE}(2)}\left(T[\bar{v}, 0, 0]^{\mathsf{T}}\right), \qquad \Delta g_{\text{inc}} = \Delta g_{\text{base}}^{-1} \Delta g_{\text{cycle}}. \tag{5.21}$$

The multiplication order expresses the residual in the carrier frame at the beginning of the cycle. Let

$$\mathrm{Log}_{\mathrm{SE}(2)}(\Delta g_{\text{inc}}) = (\rho_{\text{inc}}, \phi_{\text{inc}}), \qquad \rho_{\text{inc}} \in \mathbb{R}^2, \tag{5.22}$$

where the principal logarithm is guarded against rotational windings. Every archived 3SEG cycle lies on its reliable principal branch.

The normalized quantity

$$r_{\text{inc}} = 100\,\frac{\|\rho_{\text{inc}}\|}{|\bar{v}|\,T} \quad (\%) \tag{5.23}$$

is reported only for $|\bar{v}| \geq 1$. This threshold is a numerical reporting guard: as the matched straight displacement tends to zero, the ratio becomes ill-conditioned. The absolute residual $\|\rho_{\text{inc}}\|$ remains defined for every cycle, including the 58 AP and 8 IP rows inside the guard.

Figure 5.4 shows the resulting absolute and guarded relative residuals for both complete populations.

Population medians and upper quantiles are more informative here than extrema alone. For AP, the median absolute log-translation residual is 1.28793×10^{-3}. Among the 2,220 guarded AP cycles, the median normalized fraction is 0.007499%, the 95th percentile is 0.02807%, and every value is below 0.1%. For IP, the median absolute residual is 2.50858×10^{-3}. Among 1,350 guarded IP cycles,

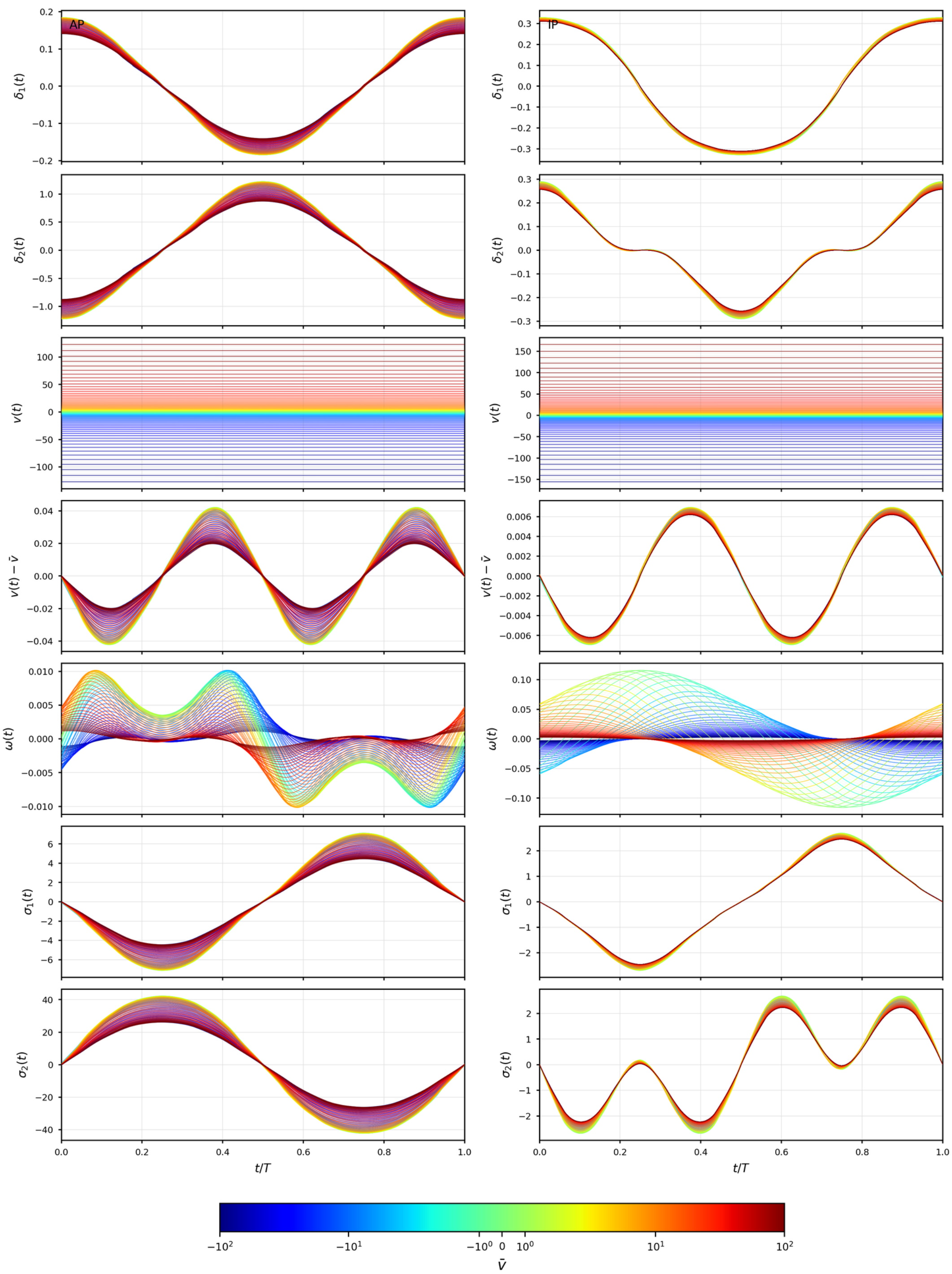

Figure 5.3: Representative time signals from the fixed 72+72 display sample. AP exhibits rapid opposed joint motion; IP exhibits slower same-direction motion. The traces illustrate finite-amplitude sector identity after return and are not evidence of stability or attraction.

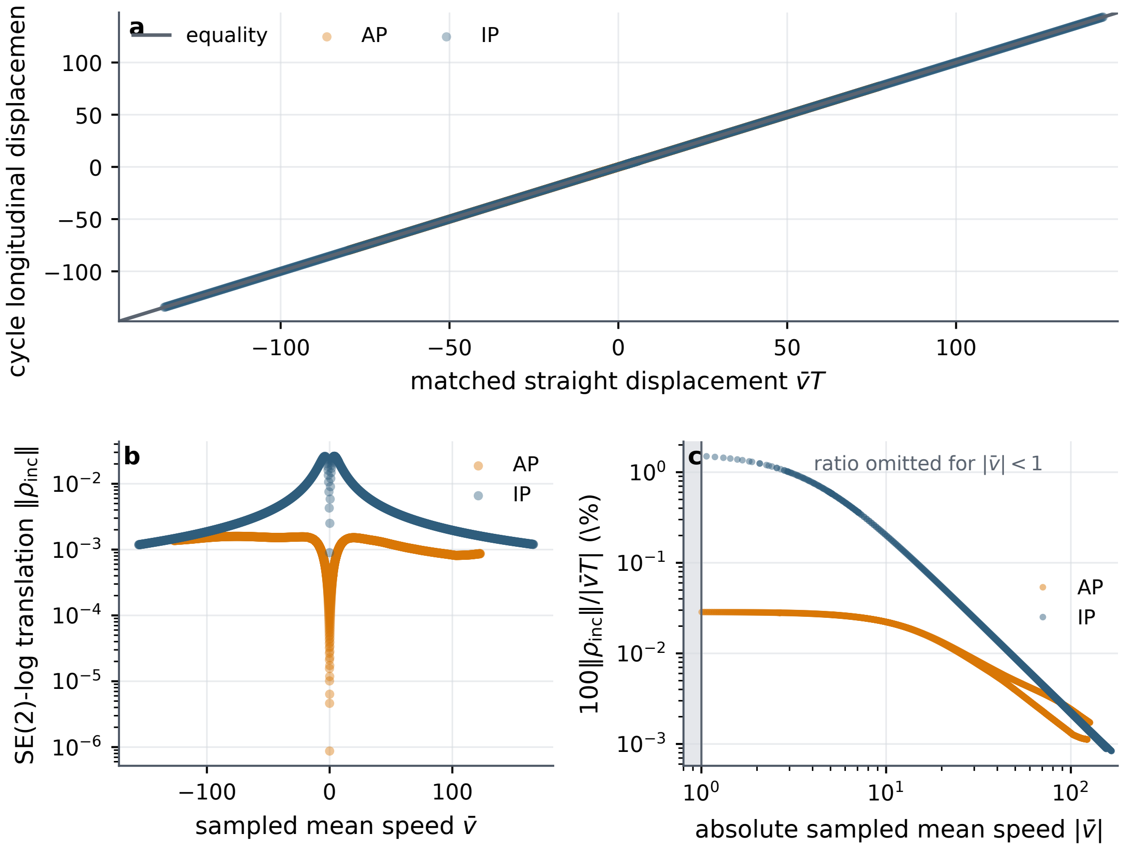

Figure 5.4: Matched-straight pose decomposition for all returned AP and IP cycles. Panel (a) compares reconstructed longitudinal displacement with the straight reference $\bar{v}T$. Panel (b) reports the translational component $\|\rho_{\mathrm{inc}}\|$ of the principal $SE(2)$ logarithm of Δg_{inc}. Panel (c) normalizes this residual only where $|\bar{v}| \geq 1$; the grey band is omitted from ratio claims. The residual is a group-theoretic matched counterfactual, not a causal label or an energetic definition of propulsion.

the normalized median is 0.003776%, the 95th percentile is 0.5921%, 98.37% lie below 1%, and the maximum is 1.497%.

At the nearest recorded pair to $\bar{v} = -8$, the AP cycle has $\bar{v} = -7.99366$ and $r_{\text{inc}} = 0.02414\%$; the IP cycle has $\bar{v} = -8.06400$ and $r_{\text{inc}} = 0.2906\%$. This comparison quantifies different path modulation at nearly matched mean speed. It does not establish which internal coordinate caused the displacement or how much energetic propulsion should be assigned to it.

Away from the near-zero guard, the matched straight term therefore dominates translation for most cycles, especially in AP, with the quantified IP tail above. No normalized dominance statement is made for $|\bar{v}| < 1$; absolute residuals must be read there. Repeating the reconstruction with every second archived sample changed the incremental log translation by less than 0.1% relative in the recorded decimation check.

5.8 What transfers from the scalar construction

The carrier-closed auxiliary system, Schur-complement storage, local modal seeds, state bridge, opened correction, and pose reconstruction all transfer from the scalar construction as useful organizing devices. The scalar exchange–return equivalence does not. In 3SEG, one storage value leaves a set of possible endpoints, so the opened state must return as a vector. Modal metrics classify the already-returned cycle, and exchange records the associated transverse-storage balance.

The numerical result is coexistence at one parameter vector: a faster, higher-activity AP branch chain and a slower, lower-activity IP branch chain, both consisting of returned moving cycles of the same unforced field. The population audit supports the opened return, modal, field-consistency, exchange, and pose rows that it explicitly recomputed or collected. It does not supply a population-wide closed-support genealogy, stability, completeness, or a claim that internal oscillation alone causes propulsion.

What the reader can now explain

The reader can now explain why the scalar theorem of Chapter 4 stops at one transverse degree of freedom: an oriented storage ellipse still contains multiple endpoints. The reader can also distinguish the three roles used here. Six-component return qualifies a relative-periodic solution; full-cycle modal metrics classify it as AP or IP; zero cycle-mean exchange follows as a balance identity once that state has returned.

The reconstructed pose establishes moving branch chains, while the matched-straight $SE(2)$ ablation shows that their translation is usually dominated by the same-speed straight contribution outside the declared near-zero guard. The remaining group residual measures path modulation, not a unique causal or energetic contribution of internal oscillation.

The conservative cycles can repeat without maintained input if initialized exactly on them; no attraction has been established. Chapter 6 next changes the energy equation by adding dissipation and periodic input, so exact work balance replaces conservative energy preservation.

Part III

Losses and accompaniment

Chapter 6

From conservative recurrence to resonantly maintained locomotion

Closest antecedent. Nonlinear vibration theory explains how conservative backbone motions can, under perturbative hypotheses, organize nearby forced–damped responses. Cycle work balance, force appropriation, quadrature diagnostics, nonlinear frequency-response continuation, folds, and isolated response curves are all established tools (Cenedese and Haller, 2020a,b; Peeters et al., 2011; Kuether et al., 2015).
Precise boundary. Those results do not identify the large forced-response archive used below with the conservative families of Chapters 3– 5. The archive uses the same kinematic type of two-segment locomotor but different inertial, elastic, damping, and forcing parameters. It is therefore an independent forced analogue. Moreover, periodicity implies an exact cycle work identity, whereas quadrature is only a signal-dependent empirical marker; neither statement supplies stability, attraction, or optimality.
Chapter delta. The chapter contributes two deliberately separate numerical results. First, one verified conservative 2SEG cycle is continued through a declared same-mechanics homotopy that adds damping and synchronized joint torque. This supplies one local numerical connection, not a persistence result for the whole conservative family. Second, the parameter-distinct forced archive is organized as a Resonant Locomotion Map (RLM): a map from computed period-matched responses to phase, waveform, speed, and reconstructed pose. Its positive-peak-speed ridge is aligned with quadrature on one audited segment and ceases to be so at larger forcing.

6.1 What losses change

The energy preview in Chapter 2 can be made concrete with the scalar forced oscillator

$$m\ddot{x} + c\dot{x} + kx + \alpha x^3 = F\cos(\Omega t). \tag{6.1}$$

With $F = 0$ and $c > 0$, the mechanical energy decreases as $\dot{E} = -c\dot{x}^2$ and a non-equilibrium oscillation decays. With forcing,

$$\dot{E} = F\cos(\Omega t)\dot{x} - c\dot{x}^2 = P_{\text{in}} - P_{\text{diss}}. \tag{6.2}$$

If a response returns after the excitation period $T_{\text{exc}} = 2\pi/\Omega$, then its stored energy also returns and

$$\boxed{\int_0^{T_{\text{exc}}} P_{\text{in}}\ \mathrm{d}t = \int_0^{T_{\text{exc}}} P_{\text{diss}}\ \mathrm{d}t.} \tag{6.3}$$

This equality is necessary for a periodic response. It does not determine the response waveform, phase, existence, or stability.

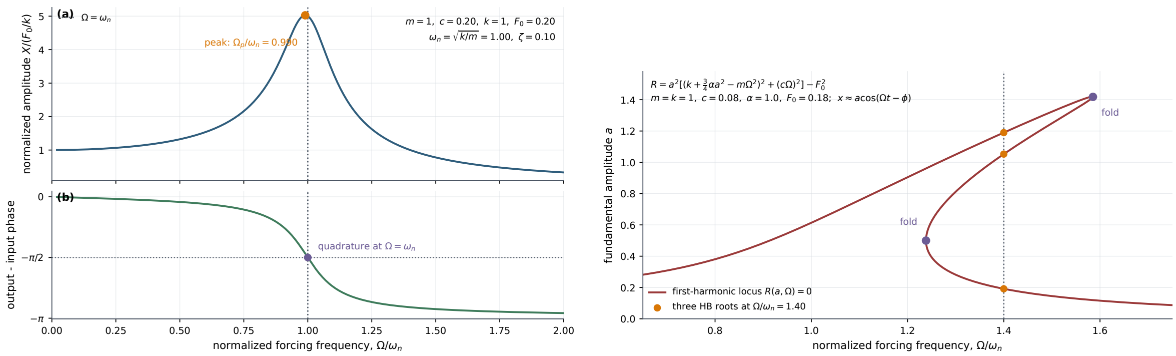

(a) Linear amplitude and output-minus-input phase.

(b) A generic finite-amplitude fold.

Figure 6.1: The one-coordinate reference. In the lightly damped linear case, the response peak lies near a quarter-period displacement lag. At finite amplitude, a response projection can bend and become multivalued. These panels teach the diagnostic and the fold; they are not predictions for the locomotor models below.

Sampling at one fixed phase of the input gives the stroboscopic map $P_{T_{\mathrm{exc}}}$. A period-matched response is a fixed point,

$$P_{T_{\mathrm{exc}}}(z_0) = z_0. \tag{6.4}$$

The forcing clock removes the free choice of time origin present on an autonomous orbit. Equation (6.4) states return at the same forcing phase; it does not state that the fixed point attracts nearby initial conditions.

The linear panel explains why quadrature is useful: when displacement lags force by a quarter period, velocity is in phase with force and receives positive mean power. The nonlinear panel explains why that intuition must be checked rather than assumed. Several responses may coexist at the same input, and a phase condition need not identify the same observable maximum on every part of a folded response set.

6.2 A same-mechanics bridge for one conservative cycle

The first calculation retains exactly the geometry, inertia, nonholonomic constraint, and quadratic–quartic potential of the conservative 2SEG model in Chapter 3. Starting from (3.9), it adds only isotropic viscous loss and a joint torque through the homotopy

$$M(\delta)\dot{\eta} + c(\delta, \eta) + \begin{bmatrix} 0 & 0 & U'(\delta) \end{bmatrix}^{\mathsf{T}} + \lambda c_\star \eta = B_\delta \lambda A_\star \sin\left(\frac{2\pi t}{T_\lambda} + \phi_\lambda\right), \qquad B_\delta = \begin{bmatrix} 0 & 0 & 1 \end{bmatrix}^{\mathsf{T}}. \tag{6.5}$$

Here $c_\star = 10^{-3}$ and $A_\star = 0.0371395$. Thus $\lambda = 0$ is the original unforced conservative field. For $\lambda > 0$, damping and forcing are ramped together, while the response period T_λ and input phase ϕ_λ are corrected with the orbit. The time origin is fixed by the oriented section $\delta(0) = 0$, $\sigma(0) > 0$.

The anchor is the repolished conservative cycle RG327 at

$$\bar{v} = 10.43581096, \qquad T_0 = 0.67499472, \qquad \|z(T_0) - z(0)\|_\infty = 2.22 \times 10^{-14}. \tag{6.6}$$

At each positive λ, four reduced-return rows and the same fixed mean speed are imposed. Nineteen declared values connect $\lambda = 0$ to $\lambda = 1$. The maximum strict return residual is 7.11×10^{-10} and the maximum mean-speed error is 1.08×10^{-12}. At the first positive point, $\lambda = 10^{-4}$, the normalized waveform distance from the conservative anchor is 4.66×10^{-5}; the period and joint excursion differ by only $-2.07 \times 10^{-3}\%$ and $2.42 \times 10^{-3}\%$, respectively.

At $\lambda = 1$, the period is 0.60392282, a 10.529% decrease from the anchor, and the joint peak-to-peak excursion has increased by 13.724%. The input work and dissipated work are, respectively,

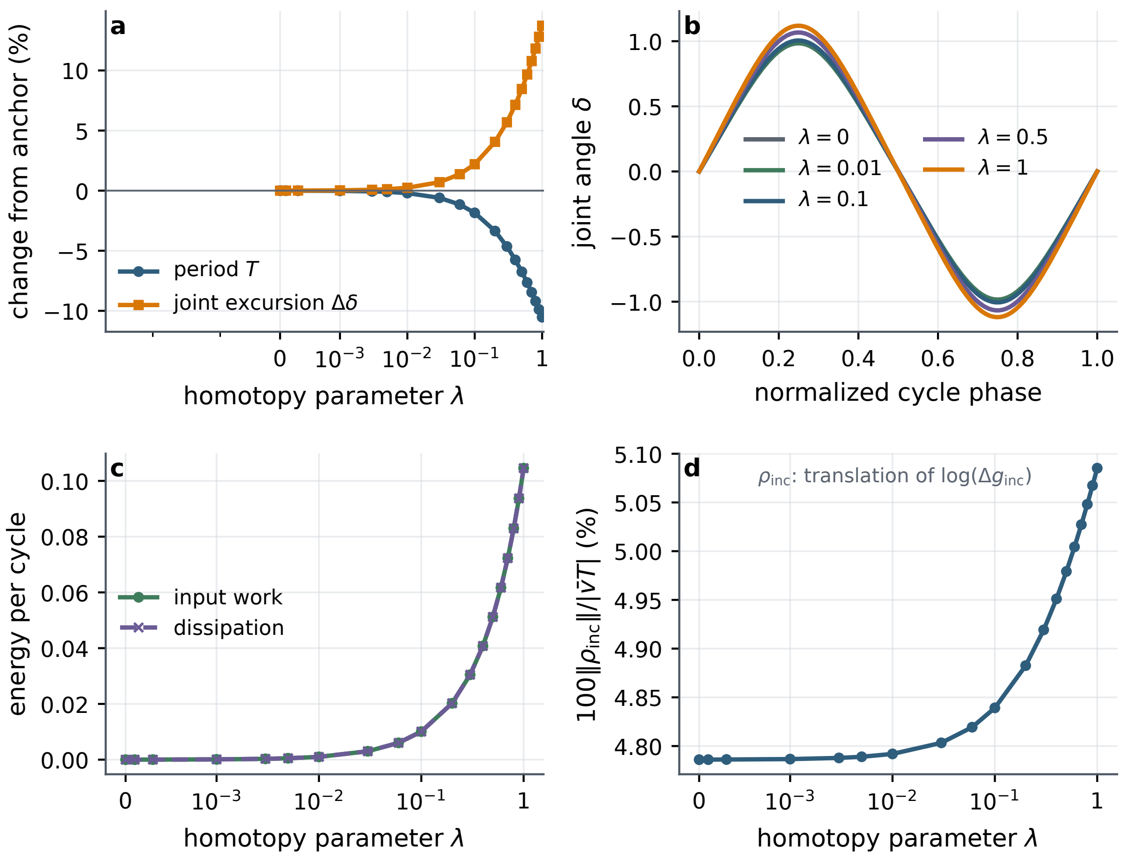

Figure 6.2: One same-mechanics conservative-to-forced bridge at fixed mean speed. (a) Period and joint excursion vary continuously from the conservative anchor. (b) Phase-aligned joint waveforms approach the anchor as $\lambda \to 0$. (c) Input work and viscous dissipation coincide on the returned branch. (d) The translational component of $\log(\Delta g_{\text{inc}})$ is normalized by the matched straight translation. This last quantity is a reference-dependent pose residual, not an additive or causal attribution of propulsion.

0.104563190334 and 0.104563190336; their relative difference is 2.60×10^{-11}. Across the audit, the mechanical energy identity has absolute error below 4.12×10^{-13}.

This calculation demonstrates a synchronized numerical deformation of one cycle under the same mechanical core. It does not prove persistence of the whole conservative family, uniqueness of the forced branch, orbital stability, or attraction. The physical input phase also becomes unidentifiable as $\lambda \to 0$ because the input vanishes. The complete homotopy, conditioning, mesh, and tolerance audits are recorded in Appendix D.

6.3 A separate parameter-distinct forced model

The large response archive answers a different question: how does a related two-segment locomotor organize finite-amplitude responses over a broad forcing domain? It is associated with the OCEANS study (Rajaomarosata et al., 2025b), but the scientific object used here is the declared model and its computed response set, not the archive name.

The configuration and reduced state are

$$q_f = (g, \delta), \qquad g = (x, y, \theta) \in \mathrm{SE}(2), \qquad z_f = (\delta, v, \omega_b, \sigma)^{\mathsf{T}}, \tag{6.7}$$

with carrier-forward velocity v, body-yaw rate $\omega_b = \dot{\theta}$, and joint rate $\sigma = \dot{\delta}$. The same wheel-like row removes lateral carrier velocity.

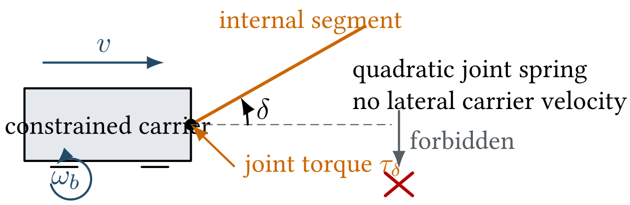

Figure 6.3: Architecture of the parameter-distinct forced model. Its kinematic pattern matches 2SEG, but its design vector and elastic law do not match the conservative reference or the bridge in Section 6.2.

Table 6.1: The local bridge and the large forced archive answer separate questions.

Feature	Same-mechanics bridge	Large forced archive
Kinematics	Same 2SEG constraint and reconstruction	Same kinematic type
Elastic and inertial design	Exactly the Chapter 3 design	Different design vector and quadratic potential
Forced object	One branch from one conservative anchor at fixed $\bar{v}$	Broad independently computed response set
Permitted inference	Local numerical same-mechanics connection	Model-specific RLM; no lineage from the conservative archive

Its projected equations use the audited sign convention

$$M_f(\delta)\dot{\eta}_f + F_f(\delta,\eta_f) + D_f\eta_f = B_\delta\tau_\delta(t), \qquad \eta_f = \begin{bmatrix} v & \omega_b & \sigma \end{bmatrix}^\mathsf{T}, \qquad D_f = c_d I_3, \qquad c_d = 10^{-3}. \tag{6.8}$$

The nondimensional potential is $V_f(\delta) = \delta^2$, so its restoring torque is -2δ. The design vector is $\varepsilon_f = 0.73170844$, $\gamma_f = 0.73680149$. Exact coefficients, scaling, and sign checks are given in Appendix D.

The imposed torque and its mechanical power are

$$\tau_\delta(t) = A_{\text{exc}} \sin(\Omega t + \varphi_{\text{in}}), \qquad \Omega = \frac{2\pi}{T_{\text{exc}}}, \qquad P_{\text{in}} = \tau_\delta \sigma. \tag{6.9}$$

All reported amplitudes are nondimensional. The archived display coordinate is $10^3 A_{\text{exc}}$; it is an N mm value only under the optional scaling $k_0 = 1\,\text{N m}$. Viscous dissipation is

$$P_{\text{diss}} = c_d\left(v^2 + \omega_b^2 + \sigma^2\right). \tag{6.10}$$

For any exact periodic solution of (6.8), these two powers satisfy (6.3). This is an analytical consequence of periodicity, not a second independent response condition.

The pose remains open and is reconstructed from

$$\dot{x} = v\cos\theta, \qquad \dot{y} = v\sin\theta, \qquad \dot{\theta} = \omega_b. \tag{6.11}$$

Thus a forced locomotor response can close in z_f while accumulating a pose increment $\Delta g = g(0)^{-1} g(T_{\text{exc}})$.

6.4 Period-matched responses and the RLM

At a fixed input phase, a synchronized response solves

$$\mathcal{R}_{\text{per}}(z_0; A_{\text{exc}}, T_{\text{exc}}) := \Phi^{A,T}_{T_{\text{exc}}}(z_0) - z_0 = 0. \tag{6.12}$$

An autonomous forcing lift and a scalar numerical phase gauge allow the same object to be solved as a periodic boundary-value problem. Their exact implementation is recorded in Appendix D; the gauge must not be confused with the measured output–input phase below.

The archive was assembled by continuation in excitation period at fixed amplitude, followed by continuation in amplitude from selected responses. Pseudo-arclength correction follows the zero set of (6.12) through a fold, as introduced in Chapter 2. The result is an orbit-valued response set, not the single asymptotic trace produced by one initial condition.

For every computed response, retain the observable tuple

$$\mathcal{O} = (A_{\text{exc}}, T_{\text{exc}}, v_{\text{pk}}, \bar{v}, \phi_{\delta\tau}, \text{THD}_{\delta}, \Delta g)\,, \tag{6.13}$$

where v_{pk} is the sampled positive within-cycle maximum, $\bar{v}$ is mean forward speed, $\phi_{\delta\tau}$ is the deformation phase relative to torque, and THD_{δ} summarizes deformation harmonics. The *Resonant Locomotion Map* (RLM) is the image of the computed period-matched response set under (6.13). The word “map” denotes this observable organization. It asserts neither a manifold structure nor a deformation of the conservative natural-locomotion family.

6.4.1 The offline phase convention

The archive phase uses joint deformation as output and applied torque as input. Each adaptive-mesh cycle is first interpolated periodically onto a uniform grid with the duplicated endpoint removed. Centered analytic signals are then used to form the circular mean of their pointwise phase difference. The convention is

$$\phi_{\delta\tau} = \text{phase}_{\text{H}}(\delta) - \text{phase}_{\text{H}}(\tau_{\delta}) \quad \text{wrapped to } [-\pi, \pi), \qquad \phi_{\delta\tau}^{Q} = -\frac{\pi}{2}. \tag{6.14}$$

Here phase_{H} is shorthand for the audited Hilbert analytic-signal statistic, not a pointwise phase on an arbitrary transient. The resampling, circular-mean formula, and harmonic extraction are specified in Appendix D. Chapter 7 uses a different online fundamental estimator with the same signal order and target.

6.5 What the large response archive shows

The central observation is not the number of files but the geometry of the response projection. At fixed amplitude, the positive peak speed varies with excitation period, and the curves bend enough that the same input coordinates can correspond to several period-matched responses.

The archive contains 13 782 stored cycles in 25 amplitude groups over $A_{\text{exc}} = 0.00205$–0.07357. All saved first and last samples agree in the four mechanical and two forcing-lift states at exported precision. The original collocation residuals were not archived, so this endpoint check is not presented as an independent reconstruction of every boundary-value solve.

At the straight rest state, eliminating yaw gives the effective shape inertia $M_{\text{lin}} = 0.02582240489$. Since $V_f = \delta^2$, the linear period is

$$T_{\text{lin}} = 2\pi\sqrt{\frac{M_{\text{lin}}}{2}} = 0.7139424640. \tag{6.15}$$

The observed peak-period shift is finite and non-monotone: 3.7940% at rank 15, 4.4691% at rank 16, and 3.8114% at rank 25. The data establish this response-level departure from the linear reference; they do not isolate which inertial or dissipative term causes it.

A fold means that a vertical line in Figure 6.4 can meet one fixed-amplitude curve more than once. These intersections are distinct periodic solutions of the boundary-value problem at the same forcing coordinates. They need not share waveform, mean speed, phase, or pose increment. Their coexistence does not imply that every solution is attracting or reachable from the same initial condition.

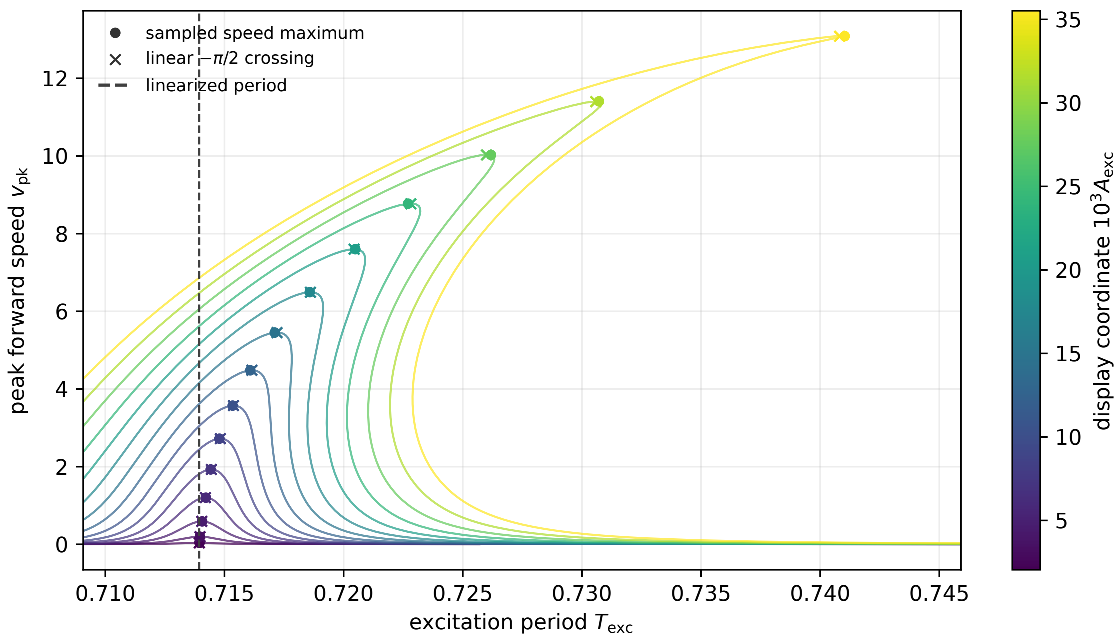

Figure 6.4: Positive peak-forward-speed responses for forcing ranks 1–15. Each colored curve is a continued set at fixed nondimensional amplitude. Circles mark sampled speed maxima, crosses mark piecewise-linearly interpolated $-\pi/2$ phase crossings, and the dashed line is the exact linearized period. Color denotes the display coordinate $10^3 A_{\rm exc}$.

6.6 Exact cycle work and a local quadrature marker

The exact and empirical statements must remain separate. For every exact periodic response of the forced model, full-cycle work balance is

$$\int_0^T \tau_\delta \sigma \, \mathrm{d}t = \int_0^T c_d(v^2 + \omega_b^2 + \sigma^2) \, \mathrm{d}t. \tag{6.16}$$

It includes the complete waveform and all three dissipative pseudo-velocity channels.

Quadrature has a narrower role. If the torque and deformation fundamentals are

$$\tau_1(t) = \hat{\tau}\cos(\Omega t), \qquad \delta_1(t) = \hat{\delta}\cos(\Omega t - \pi/2), \tag{6.17}$$

then $\dot{\delta}_1$ is in phase with the torque and

$$\frac{1}{T}\int_0^T \tau_1 \dot{\delta}_1 \, \mathrm{d}t = \frac{1}{2}\Omega\hat{\tau}\hat{\delta} > 0. \tag{6.18}$$

This calculation motivates the sign and the use of phase; it does not make the Hilbert phase in (6.14) equivalent to the complete work identity.

For each forcing group, the audit compares the sampled maximum $(T_{\rm r}, v_{\rm r})$ with the piecewise-linearly interpolated $-\pi/2$ crossing (T_Q, v_Q). Every rank from 1 through 15 contains such a crossing, and

$$\boxed{\max_{1\le i\le 15} 100\frac{|v_Q - v_{\rm r}|}{v_{\rm r}} = 0.0635625\% < 0.064\%, \qquad \max_{1\le i\le 15} 100\frac{|T_Q - T_{\rm r}|}{T_{\rm r}} = 0.0289515\%.} \tag{6.19}$$

The largest phase distance from a sampled speed maximum to quadrature on this range is $0.0452127\,\mathrm{rad}$. These bounds concern one estimator, one sampled domain, and the positive peak-speed observable.

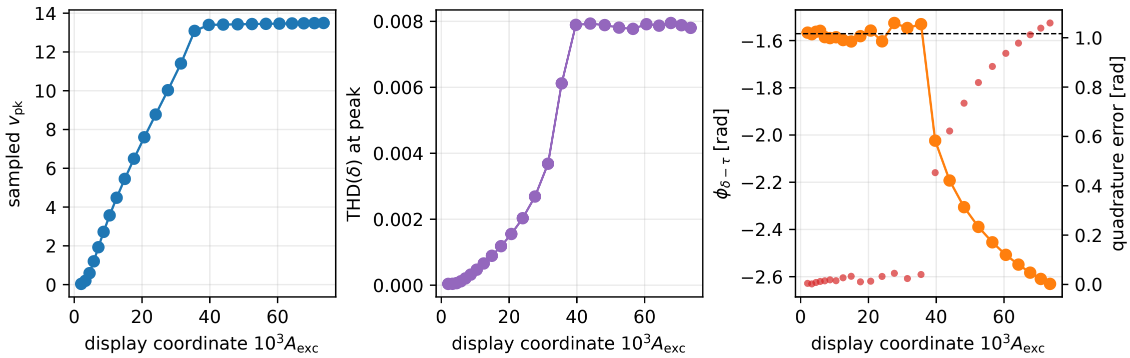

Figure 6.5: Observables at the sampled speed maximum of all 25 forcing groups. Peak speed grows and plateaus (left), deformation harmonic content changes (center), and the output-minus-input Hilbert phase remains near $-\pi/2$ only on the lower-amplitude segment (right). The horizontal coordinate is the nondimensional display value $10^3 A_{\mathrm{exc}}$.

The behavior changes after rank 15. Ranks 16–20 contain a sampled quadrature crossing on a branch whose peak speed is approximately 59–72% below the group maximum. Ranks 21–25 contain no sampled $-\pi/2$ crossing; this is absence from the audited sample, not proof of global nonexistence.

The same figure also shows why an imposed sinusoidal torque does not prescribe a sinusoidal locomotor state. The joint waveform acquires harmonics, and the relation among shape, carrier speed, and yaw changes over the response set. Quadrature is therefore a useful local coordinate on ranks 1–15, not a global definition of resonance or locomotor performance.

6.7 Reconstructed locomotor output and the missing coordinate

Peak velocity alone does not establish net motion: an oscillatory velocity can integrate to zero. The pose equation (6.11) supplies the required test. The three displayed responses close in z_f and accumulate finite forward pose increments.

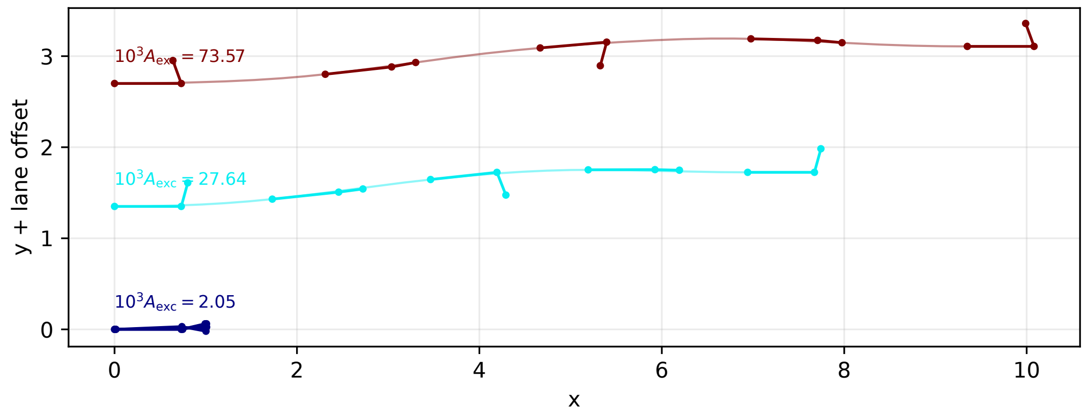

Figure 6.6: Pose reconstructions for peak-speed responses at forcing ranks 1, 13, and 25. Artificial vertical offsets separate the paths. Each displayed reduced response returns over one forcing period while the reconstructed carrier advances. The figure establishes transport for these examples, not for every archived response.

The positive-peak-speed ridge is not automatically an optimum of mean translation, input work per distance, actuator effort, or stability. Nor does phase alone locate a response on a folded map: two responses can have similar phase and different mean speeds. This ambiguity motivates the two coordinates used in Chapter 7: phase adjusts forcing frequency on the fast loop, while mean forward speed adjusts amplitude on the slower loop.

What the reader can now explain

The reader can now explain why dissipation changes the repeatable object: stored energy returns only when cycle input work replaces cycle loss. The same-mechanics homotopy demonstrates this change for one conservative 2SEG cycle, while the large RLM archive belongs to a separate parameter-distinct model and cannot be treated as that bridge's continuation.

The reader can also distinguish the two phase statements. Work balance is an exact identity for an exact periodic response. Output-minus-input quadrature is a local empirical marker of the positive-peak-speed ridge on ranks 1–15; it moves to a slower branch on ranks 16–20 and is absent from the sampled curves on ranks 21–25. Folds make phase insufficient to locate a response, so the next chapter adds mean speed and demonstrates local chart traversal, without claiming stabilization of the conservative natural-locomotion family.

Chapter 7

Local phase-locked navigation of a forced-response chart

Phase-locked loops (PLLs) already provide established ways to track nonlinear backbones and forced-response curves, while control-based continuation uses feedback to follow responses that open-loop sweeps may miss (Peter et al., 2016; Peter and Leine, 2017; Denis et al., 2018; Renson et al., 2016; Barton, 2017; Abeloos et al., 2022; Tang et al., 2020). Their precise boundary in the present locomotor is that phase lock regulates one local timing relation. It does not uniquely identify a coexisting locomotor response, provide global acquisition, or control or stabilize a conservative natural-locomotion family.

Chapter 6 supplied the missing model-specific setting: a forced and damped two-segment locomotor, a chart of period-matched responses, and a lower-amplitude segment on which output-minus-input phase remains close to quadrature. This chapter adds a locomotor coordinate to the established PLL idea. A fast frequency loop regulates phase, a slower amplitude loop uses mean forward speed to move the response, and observable guards decide whether a completed stage is retained. The result is a numerical local traversal from two named starts.

7.1 Why phase is an ambiguous coordinate

Phase measures timing, not the complete response. Two periodic motions can place the fundamental deformation nearly one quarter period behind the torque while differing in deformation amplitude, basin, harmonics, and mean translation. In a folded response set, the same phase value may therefore occur on several dynamically distinct responses.

The forced-model data expose this ambiguity directly. An amplitude-staircase experiment attempted to reach offline response rank 10 while retaining the PLL. Fifteen trials used several low-response starts and target-phase settings. None reached the target-speed neighborhood: all 15 settled on a low-speed response, even though their largest phase-error RMS was only $0.07138\,\mathrm{rad}$. A small phase error can consequently indicate lock to a response without indicating lock to the intended response.

Let Γ denote a settled forced response. The two observables used here are

$$\Gamma \longmapsto \big(\phi(\Gamma), \bar{v}(\Gamma)\big), \qquad \bar{v}(\Gamma) = \frac{1}{T}\int_0^T v(t)\ \mathrm{d}t. \tag{7.1}$$

The first component compares response timing with the applied torque. The second measures the locomotor output accumulated per unit time. On the sampled rising segment, ranks 1–14 have increasing stored pairs

$$(A, \bar{v}) : (0.0020496, 0.021457) \longrightarrow (0.0314870, 10.876395),$$

and every adjacent sampled slope is positive. Mean speed is therefore a usable local coordinate on this sampled segment: it separates responses whose phases are almost indistinguishable. Rank 15, at $(A, \bar{v}) = (0.0355189, 12.364852)$, is used only as a numerical endpoint and an a posteriori label. The flatter response region beyond it is not navigated with this coordinate.

The two measurements now answer different questions. Phase asks whether the current timing is near the local quadrature marker. Mean speed asks where the settled motion lies on the useful locomotor segment.

7.2 Online phase and the locally tested frequency sign

The controller observes the internal deformation δ relative to the applied joint torque

$$\tau_\delta(t) = A \sin \varphi_{\mathrm{exc}}(t), \qquad \dot{\varphi}_{\mathrm{exc}} = \Omega. \tag{7.2}$$

On a rolling window, a three-harmonic least-squares fit absorbs waveform distortion. Only its fundamental phases enter feedback:

$$\phi = \mathrm{wrap}_{[-\pi,\pi)}\big(\phi_\delta - \phi_\tau\big), \qquad e_\phi = \mathrm{wrap}_{[-\pi,\pi)}\left(\phi + \frac{\pi}{2}\right). \tag{7.3}$$

The order is output minus input. A deformation fundamental delayed by one quarter period has $\phi = -\pi/2$ and hence $e_\phi = 0$, as illustrated in Figure 7.1. Estimator algebra and conditioning diagnostics are recorded in Chapter E.

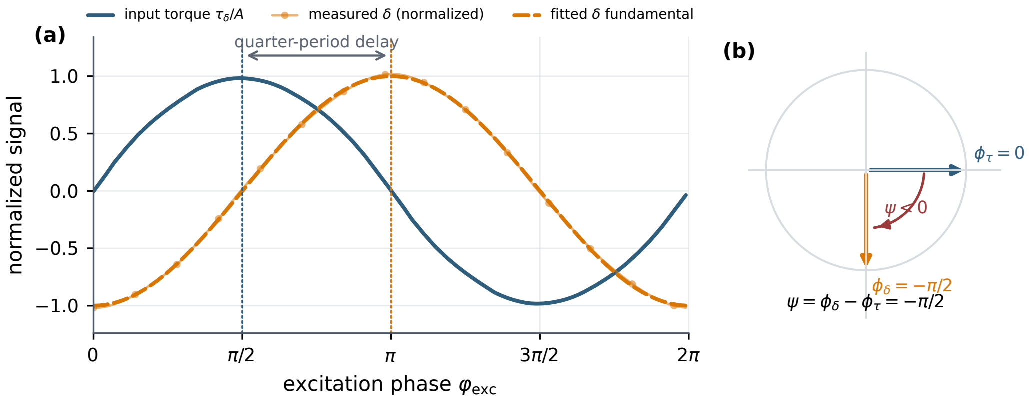

Figure 7.1: Online phase convention. The applied torque provides the excitation clock, and a rolling harmonic fit extracts the fundamental deformation phase. In the output-minus-input convention, the displayed quarter-period delay is $-\pi/2$. Higher fitted harmonics absorb waveform distortion; they are not additional feedback coordinates.

This online observable is not numerically identical to the offline Hilbert phase used to build the response map in Section 6.4.1. Both use the same output-minus-input order and quadrature target, but transients, windows, and waveform distortion affect them differently. The feedback sign was therefore tested on the online observable rather than inferred from the offline plot.

Around stored response rank 10, a positive e_ϕ must increase Ω. With that sign, initial detunings of -0.5%, $+0.5\%$, and -3% ended with phase-error RMS below 4.2×10^{-3} rad and mean frequency close to the reference. With the opposite sign and the same -0.5% detuning, the phase-error RMS remained 1.2452 rad and the mean frequency fell to 0.874 of the reference. This establishes the sign and locking behavior in the tested rank-10 neighborhood; it does not map an acquisition basin.

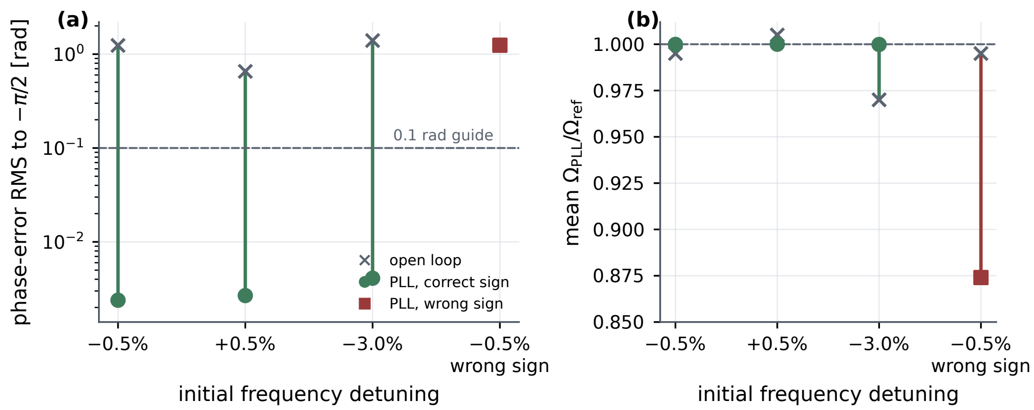

Figure 7.2: Local sign experiment around rank 10. Correct-sign feedback reduces the phase error for the three tested frequency detunings and returns the mean frequency near its reference. Reversing the sign under the same -0.5% detuning moves away from that neighborhood.

7.3 Fast phase loop, slow speed loop, and guards

The two-loop architecture follows from the two-coordinate problem:

$$\underbrace{e_\phi \longmapsto \Omega}_{\text{fast phase loop}}, \qquad \underbrace{e_v = \bar{v}_{\text{des}} - \bar{v} \longmapsto A}_{\text{slow speed loop}}. \tag{7.4}$$

Changing Ω corrects the response–forcing timing near the current periodic motion. Changing A slowly changes which settled response is maintained. The second loop is therefore not an instantaneous velocity servo: it estimates mean speed over several forcing periods and moves the operating point while the faster loop attempts to preserve phase lock.

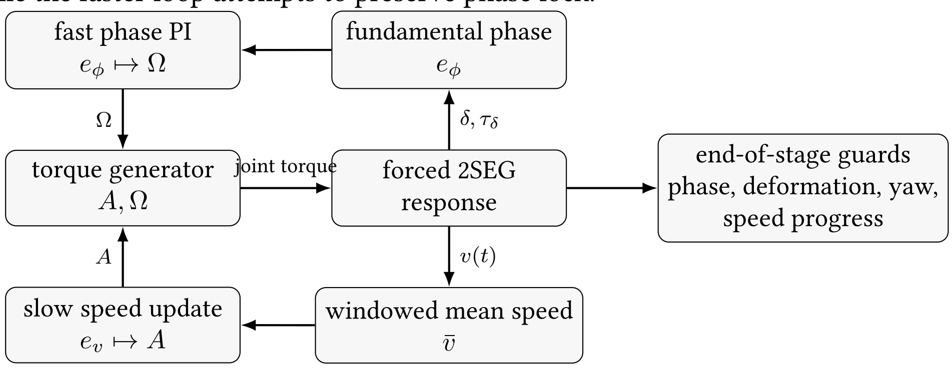

Figure 7.3: Observable-level architecture. Frequency is the fast phase actuator; amplitude is the slow locomotor-coordinate actuator. Guards inspect completed stages and decide which terminal states are retained. The offline response rank is not an online input.

A component ablation at desired mean speed $\bar{v}_{\text{des}} = 6$ makes the separation concrete.

Table 7.1: Component ablation at the speed-6 command.

Active layers	Achieved $\bar{v}$	Phase-error RMS	Observed role
Phase and speed loops	5.594	8.14×10^{-3}	Moves upward while retaining phase lock
Fixed-amplitude PLL	1.798	7.07×10^{-4}	Locks phase at the starting response
Speed loop without PLL	3.001	0.812	Moves speed but loses the phase marker

The phase loop can preserve the wrong locomotor operating point, while the speed loop alone can leave the local resonant marker.

The slow update is enabled only when phase remains sufficiently coherent. After each finite-duration stage, the supervisor checks phase-error RMS, deformation peak-to-peak, mean yaw, backward speed progress, and high-speed proximity to the command. A passing stage retains its terminal plant and controller state. A failing stage would restore the last accepted state and reduce the proposed speed increment; fixed attempt and minimum-step limits allow the software to abort rather than promise arrival. Exact gains, thresholds, stage durations, and rollback rules are collected in Chapter E.

These guards bound which simulated stages the algorithm would retain; they do not define the response coordinate. Nor does the supervisor query the offline response map. Continuation rank is attached only after a run for interpretation.

7.4 Observed traversal of the tested chart

The nominal campaign used two starts: rest, supplied with the rank-1 forcing coordinates, and the stored rank-1 periodic state. Each run accepted 21 stages and reached desired-speed command 12. The terminal mean speeds were 12.068039 and 12.067794, with terminal phase-error RMS 1.119×10^{-3} and 1.106×10^{-3} rad, respectively. Figure 7.4 shows the two recorded stage sequences.

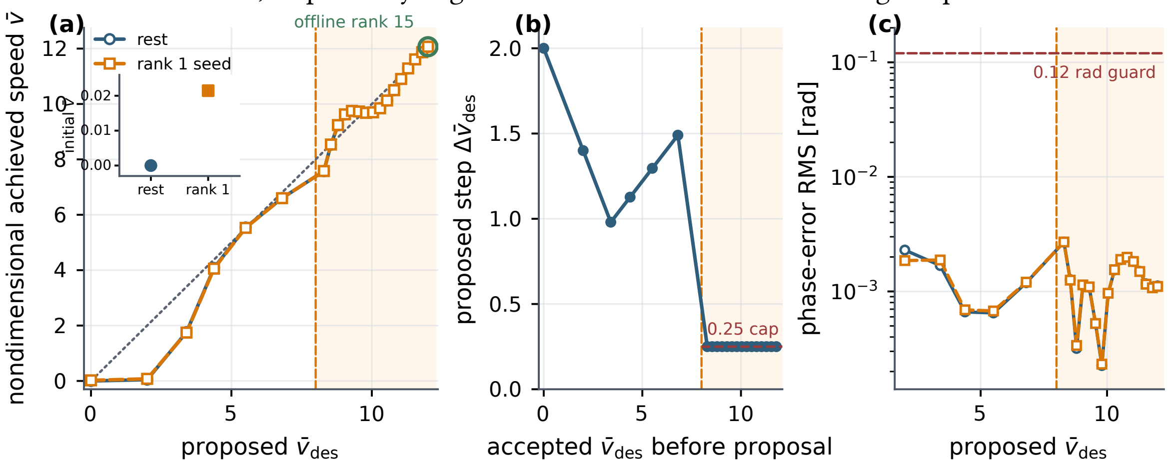

Figure 7.4: Nominal local traversal from rest and from the stored rank-1 seed. Both runs contain 21 accepted stages and terminate near mean speed 12.068. Once the accepted target reaches 8, the proposed increment is capped at 0.25. All recorded phase-error RMS values remain below the implemented guard; the rank-15 label is assigned offline.

All 42 recorded stage trials were accepted. The two runs therefore demonstrate a nominal traversal of this finite chart under this fixed guard-equipped schedule, but they do not test rejection, rollback, or recovery. The similar endpoints show consistency across the two named starts; they do not imply global acquisition, arbitrary-target tracking, or a finite-arrival theorem.

7.5 Sampled reduced-order evidence

A separate calculation projects each sampled forced response onto $K_G = 5$ harmonics of its four reduced-state components, giving 44 coordinates, and linearizes the phase-only and two-loop closures under the tested gains. The spectral abscissa is the largest real part among a matrix's eigenvalues; a negative value means asymptotic stability of that finite linear model. This Galerkin order is unrelated to the online estimator order $K_{\text{est}} = 3$.

Table 7.2: Spectral-abscissa ranges of the sampled $K_{\mathrm{G}} = 5$ Galerkin controller matrices.

Augmented model	Spectral-abscissa range	Negative samples	Domain
PLL frequency loop	$[-1.81848, -1.00100] \times 10^{-3}$	14/14	ranks 1–14
PLL and slow speed loop	$[-8.93731, -2.95865] \times 10^{-4}$	14/14	ranks 1–14

All 14 stored matrices have negative spectral abscissa. This is sampled local evidence for the $K_{\mathrm{G}} = 5$ approximation, not a certificate for the exact nonlinear plant. No bound transfers the discarded harmonics and projection residual to the full dynamics, and rank 15 is not one of the 14 linearized samples. The construction and residual comparison are given in Chapter E.

7.6 What the reader can now explain

The reader can now explain why phase is a timing coordinate, why mean speed distinguishes locomotor responses, and how fast frequency regulation, slow amplitude adaptation, and guards interact. The supported endpoint is nominal local traversal plus sampled reduced-order evidence on the declared ranges. Chapter 8 now places this local demonstration beside the conservative results and separates established links from the remaining research programme.

Part IV

Scope

Chapter 8

Synthesis, limits, and research programme

8.1 A direct answer

A mechanism's own dynamics does not generally prescribe one joint trajectory. It may instead admit families of motions compatible with a specified mechanical field. In the conservative models studied here, a member qualifies as a natural-locomotion cycle when three conditions hold together: it is a nontrivial exact solution of the unforced equations, its reduced state returns under a declared phase convention, and reconstruction gives the declared nonidentity pose increment. Continuation then organizes qualified cycles into branches, while modal observables distinguish coherent organizations within them. Here *natural* means only compatibility with the ideal unforced conservative field; it implies neither stability, attraction, optimality nor experimental persistence.

The roles of the main ingredients are consequently distinct. Linear and nonlinear modes provide local seeds and finite-amplitude organization. Reduced return makes the internal and carrier motion repeatable without closing the pose directions needed for transport. Reconstruction evaluates the resulting pose increment but does not certify the trajectory that produced it. Finally, the carrier-closed/carrier-open decomposition interprets return mechanically: in the scalar case, integrated exchange can replace the last return coordinate under explicit hypotheses; with several transverse coordinates, it remains one balance diagnostic and full vector return is indispensable.

This answer concerns moving families, not motion created solely by internal oscillation. The matched-straight comparison of Chapters 3 and 5 shows that, away from near-zero drift, the straight relative-equilibrium term usually dominates the reconstructed translation. The oscillatory cycle modulates that moving baseline in a model- and speed-dependent way.

8.2 Four insufficiencies and their resolution

The construction resolves four successive insufficiencies.

1. **A linear mode does not specify the finite motion.** It supplies a frequency and eigendirection only near an equilibrium. The continued two- and three-segment branches instead contain complete nonlinear waveforms whose period, harmonics and inter-coordinate phase relations vary along the family.

2. **Periodicity of the full locomotor configuration suppresses transport.** Closing pose together with the mechanical variables would make the body increment the identity. Symmetry reduction imposes periodicity only on the reduced state; pose remains open and is reconstructed after one reduced period. This is the relative-periodic object appropriate to locomotion.

3. **A closed internal loop does not establish naturality.** Many prescribed loops can reconstruct a displacement, and the same geometric loop with a different timing need not solve the same field. The qualification test therefore acts on the time-parameterized reduced trajectory. In 2SEG, once the other return rows hold on the oriented scalar section, the exchange–return theorem makes $I_{\text{ex}} = 0$ equivalent to the last scalar return row. In 3SEG, one storage value leaves a continuum of possible section endpoints; vector return must be solved first and IP/AP metrics classify the cycles afterwards.

4. **A conservative cycle cannot persist unchanged under positive loss.** A maintained periodic response must satisfy stroboscopic vector return and equality of input work and dissipation over a cycle. These conditions replace neither one another nor the need to distinguish coexisting forced responses. Phase supplies a local timing observable; mean speed supplies a second local chart coordinate.

The common thread is thus not a preferred sinusoid. It is a hierarchy of conditions that first qualifies a motion dynamically, then organizes it, and only afterwards interprets its locomotor output.

8.3 Established claims and observed evidence

Analytical statement. The exchange–return equivalence is the theorem-level result. Its scope is one effective transverse degree of freedom, a finite-speed chart, an oriented transverse section, closure of the other return rows, and injectivity of the section storage in the remaining coordinate. Ideal constraints do no total work; exchange describes redistribution induced by the derived closed–open decomposition. The result interprets a return row and does not prove existence or stability of a periodic family.

Audited conservative constructions. The corrected 2SEG branch and the coexisting 3SEG IP/AP branch chains are model-specific numerical constructions. The three-segment claim is coexistence of returned moving modal populations at one fixed parameter vector, not completeness or a population-wide carrier-closed genealogy. The matched $\mathrm{SE}(2)$ audit further establishes a counterfactual pose residual relative to straight motion with the same sampled mean speed and period. Its normalized value is deliberately omitted for $|\bar{v}| < 1$. It measures path modulation relative to that reference, not a unique causal or energetic share of propulsion.

One local same-model bridge. A separate audit introduces damping and harmonic joint input into one verified 2SEG conservative model while keeping its geometry, inertia, constraint and elastic potential fixed:

$$\mu_{\text{visc}}(\lambda) = \lambda c_\star, \qquad u(t;\lambda) = \lambda A_\star \sin(2\pi t/T_\lambda + \phi_\lambda)\,. \tag{8.1}$$

At fixed mean speed, a synchronized branch was followed through 19 declared values from $\lambda = 0$ to 1. Its maximum strict return residual is 7.11×10^{-10}, and the largest positive-λ relative mismatch between input work and viscous loss is 2.95×10^{-4}. At $\lambda = 10^{-4}$, the normalized waveform distance from the conservative anchor is 4.66×10^{-5}. These data demonstrate a local numerical deformation of one cycle; the forcing phase becomes unidentifiable as $\lambda \to 0$, and no whole-family persistence, uniqueness or stability follows.

Parameter-distinct forced map and local navigation. The RLM of Chapter 6 remains a separate forced-response computation with different inertial and elastic parameters. Its exact energetic statement is cycle work balance. Quadrature marks the sampled speed crest on ranks 1–15; ranks 16–20 cross quadrature on a slower branch, and ranks 21–25 contain no sampled crossing. No link between the same-model branch above and this parameter-distinct response map is asserted.

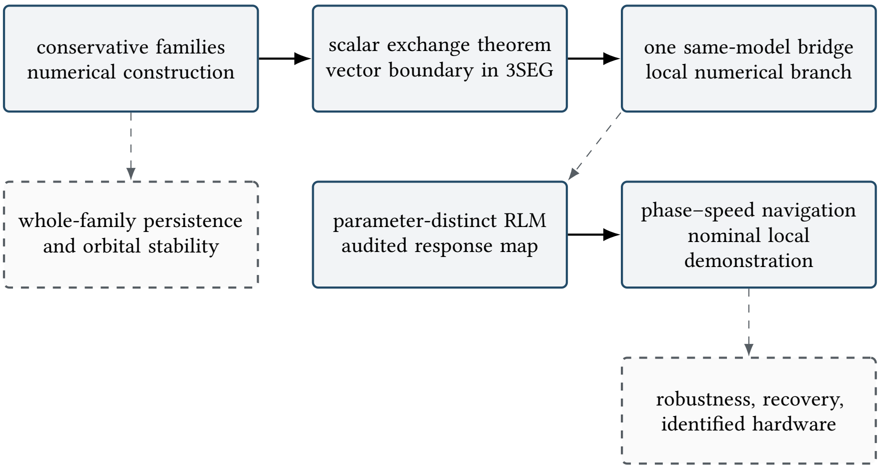

Figure 8.1: Evidence topology at the end of the thesis. Solid boxes are established at the evidence level written inside them. Dashed boxes and arrows are missing links in the programme. In particular, Gate B connects one conservative cycle to one maintained branch; it does not identify that branch with the parameter-distinct RLM archive.

The phase–speed controller of Chapter 7 demonstrates nominal local traversal from two named initializations. All 42 archived stage trials were accepted, so rejection, rollback and recovery remain untested. The negative spectral abscissae of the sampled $K_{\mathrm{G}} = 5$ matrices cover ranks 1–14 and support only those reduced-order linearizations; they do not certify the exact nonlinear plant. The supported claim is therefore local navigation of a forced-response chart, not stabilization of conservative natural-locomotion families.

8.4 Limits and research programme

The mechanical evidence comes from smooth ideal nonholonomic models with fixed nondimensional parameters. Conservative orbital stability, basins and robustness to parameter uncertainty were not established. The 2SEG archive is a numerical precursor rather than a residual certificate for every stored member; the 3SEG population audit covers the explicitly reported return, modal, exchange and pose rows but not every member's complete genealogy. The same-model bridge contains one anchored branch at one fixed mean speed, and the forced/controller archive has no experimental validation. Accordingly, the acronym NLM names the research framework; mathematical statements here use *family* or *branch*, without a global manifold theorem.

Three links define the next programme. First, the local bridge should be continued over conservative family coordinates and parameters, with folds, branch loss and any relation to the OCEANS response sheets tested rather than assumed. Second, Floquet multipliers, perturbed integrations and acquisition basins should accompany controller trials that deliberately trigger rejection, saturation and recovery. Third, identified hardware must replace ideal coefficients; hybrid contact and fluid interaction will add impact or environmental work terms, while the number of unresolved return coordinates will still determine what a scalar balance can certify.

8.5 Scientific conclusion

Natural locomotion is a nontrivial repeatable reduced motion admitted by the mechanism and accompanied by a declared reconstructed pose increment, not a choreography imposed in advance. Its finite-amplitude organization may be modal, its transport is revealed by reconstruction, and its mechanical closure is scalar only when the unresolved return information is scalar. With losses, the same principle becomes accompaniment: supply the work required by a returned response and regulate only the local coordinates needed to remain on its chart.

Appendix A

Two-segment model and conventions

This appendix gives the dimensional origin of the reduced equations used in Chapters 3–4. Its purpose is traceability: the main text works with the compact dimensionless system, while the equations below show which physical balance produces each coefficient and which sign convention is being used.

A.1 Geometry, velocities, and ideal constraint

Let m_1, I_1 be the mass and planar yaw inertia of the carrier and let m_2, I_2 denote the corresponding quantities for the internal segment. The distance from the contact point to the carrier centre of mass is l_1; the distance from the joint to the internal-segment centre of mass is l_2. The configuration and admissible velocity coordinates are

$$q = (x, y, \theta, \delta), \qquad \eta = (v, \omega, \sigma)^\top, \qquad \dot{q} = H(\theta)\eta, \tag{A.1}$$

with H given in Equation (3.3). Thus v is positive along the carrier heading, $\omega = \dot{\theta}$, and $\sigma = \dot{\delta}$. The absolute angular speed of the internal segment is $\omega + \sigma$. This last convention fixes the signs of all mixed inertia terms.

Let $r_C = (x, y)^\top$ be the constrained contact point and define

$$e(\varphi) = \begin{bmatrix} \cos\varphi \\ \sin\varphi \end{bmatrix}, \qquad e_\perp(\varphi) = \begin{bmatrix} -\sin\varphi \\ \cos\varphi \end{bmatrix}. \tag{A.2}$$

In the geometry used by the reduced model, the carrier centre of mass and the joint are co-located at

$$r_1 = r_J = r_C + l_1 e(\theta), \qquad r_2 = r_J + l_2 e(\theta + \delta), \tag{A.3}$$

where r_2 is the internal-segment centre of mass. Since $\dot{r}_C = v e(\theta)$,

$$\dot{r}_1 = v e(\theta) + l_1 \omega e_\perp(\theta), \tag{A.4}$$

$$\dot{r}_2 = \dot{r}_1 + l_2(\omega + \sigma) e_\perp(\theta + \delta). \tag{A.5}$$

These positions remove any ambiguity about the reference points of l_1 and l_2.

The constrained Lagrange–d'Alembert equation is

$$\frac{\mathrm{d}}{\mathrm{d}t}\frac{\partial L}{\partial \dot{q}} - \frac{\partial L}{\partial q} = A(\theta)^\top \lambda, \qquad L = T - U(\delta). \tag{A.6}$$

Because $A(\theta)H(\theta) = 0$, multiplication by $H^\top$ eliminates the reaction multiplier. The ideal lateral reaction consequently performs no work on an admissible velocity. The projected balance is

$$M_{\mathrm{dim}}(\delta)\dot{\eta} + h_{\mathrm{dim}}(\delta, \eta) + \begin{bmatrix} 0 & 0 & U'(\delta) \end{bmatrix}^\top = 0. \tag{A.7}$$

A.2 Dimensional reduced equations

Set $M_{\text{tot}} = m_1 + m_2$ and $D = \omega + \sigma$. The kinetic energy is

$$T = \frac{1}{2}m_1 \|\dot{r}_1\|^2 + \frac{1}{2}I_1\omega^2 + \frac{1}{2}m_2 \|\dot{r}_2\|^2 + \frac{1}{2}I_2 D^2. \tag{A.8}$$

Direct evaluation and projection give

$$M_{\text{dim}}(\delta) = \begin{bmatrix} M_{\text{tot}} & -m_2 l_2 \sin\delta & -m_2 l_2 \sin\delta \\ -m_2 l_2 \sin\delta & I_1 + I_2 + M_{\text{tot}} l_1^2 + m_2 l_2^2 + 2m_2 l_1 l_2 \cos\delta & I_2 + m_2 l_2^2 + m_2 l_1 l_2 \cos\delta \\ -m_2 l_2 \sin\delta & I_2 + m_2 l_2^2 + m_2 l_1 l_2 \cos\delta & I_2 + m_2 l_2^2 \end{bmatrix}. \tag{A.9}$$

The quadratic inertial vector is

$$h_{\text{dim}} = \begin{bmatrix} -M_{\text{tot}} l_1 \omega^2 - m_2 l_2 \cos\delta\, D^2 \\ (M_{\text{tot}} l_1 + m_2 l_2 \cos\delta) v\omega - m_2 l_1 l_2 \sin\delta\, (D^2 - \omega^2) \\ m_2 l_2 \cos\delta\, v\omega + m_2 l_1 l_2 \sin\delta\, \omega^2 \end{bmatrix}. \tag{A.10}$$

The first row is the longitudinal balance, the second is the carrier-yaw balance, and the third is the internal-joint balance. In particular, the finite-speed product $v\omega$ is present in the mechanical model before the change of variables $q_y = v\omega$ used in Chapter 4.

The signs in Equations (A.9) and (A.10) can be checked without redoing the full variational calculation. At $\delta = 0$ the translation–rotation inertia terms proportional to $\sin\delta$ vanish. At $\omega = \sigma = 0$ the entire drift vector vanishes. Hence every state $(0, v, 0, 0)$ is a reduced equilibrium, exactly as required by Equation (3.16).

A.3 Dimensionless dictionary and energy check

Let

$$L = l_1 + l_2, \qquad \alpha = \frac{l_1}{L}, \qquad \beta = \frac{l_2}{L}, \qquad \alpha + \beta = 1, \tag{A.11}$$

and let t_* be the reference time. Hats denote dimensionless variables:

$$\widehat{x} = \frac{x}{L}, \quad \widehat{t} = \frac{t}{t_*}, \quad \widehat{v} = \frac{t_* v}{L}, \quad \widehat{\omega} = t_*\omega, \quad \widehat{\sigma} = t_*\sigma, \quad \widehat{E} = \frac{t_*^2 E}{M_{\text{tot}} L^2}. \tag{A.12}$$

Because the joint angle δ is already dimensionless, dimensional spring coefficients in $U_{\text{dim}} = \frac{1}{2}k_{2,\text{dim}}\delta^2 + \frac{1}{4}k_{4,\text{dim}}\delta^4$ become

$$\widehat{k}_2 = \frac{t_*^2 k_{2,\text{dim}}}{M_{\text{tot}} L^2}, \qquad \widehat{k}_4 = \frac{t_*^2 k_{4,\text{dim}}}{M_{\text{tot}} L^2}. \tag{A.13}$$

The numerical chapters drop hats after this normalization. Their periods, velocities, and energies are therefore dimensionless unless an explicit dimensional calibration is supplied; in particular, the reported period range and the values $k_2 = 1$, $k_4 = 10$ belong to this numerical scale. When $k_{2,\text{dim}} > 0$, choosing $t_* = \sqrt{M_{\text{tot}} L^2 / k_{2,\text{dim}}}$ sets $\widehat{k}_2 = 1$; the computations may equivalently be read as fixing that reference clock.

The remaining design ratios are

$$\mu = \frac{m_2}{M_{\text{tot}}}, \qquad j_i = \frac{I_i}{M_{\text{tot}} L^2}, \tag{A.14}$$

and the design used in the conservative computations specializes to

$$\alpha = \varepsilon, \qquad \beta = 1 - \varepsilon, \mu = 1 - \varepsilon, \qquad j_1 = \gamma\alpha^3, \qquad j_2 = \gamma\beta^3. \tag{A.15}$$

Dividing Equation (A.9) by the common mass–length scales then produces

$$\frac{m_2 l_2}{M_{\text{tot}} L} = \mu\beta, \qquad \frac{I_1}{M_{\text{tot}} L^2} = j_1, \qquad \frac{I_2}{M_{\text{tot}} L^2} = j_2, \tag{A.16}$$

and hence the functions $\rho, B_{11}, B_{12}, B_{22}$ in Equation (3.11). The common minus sign in the first row and column of Equation (3.10) is inherited from the chosen positive direction of δ; it is not absorbed into the definition of ρ.

For the unforced conservative model, the projected energy is

$$E = \frac{1}{2}\eta^{\mathsf{T}} M(\delta)\eta + U(\delta). \tag{A.17}$$

Differentiating and substituting Equation (3.9) gives

$$\dot{E} = \eta^{\mathsf{T}}\left(M\dot{\eta} + h + \begin{bmatrix}0 & 0 & U'\end{bmatrix}^{\mathsf{T}}\right) = 0, \tag{A.18}$$

where the quadratic vector is the one induced by the configuration-dependent kinetic metric. This identity was also checked numerically along the reduced flows used for continuation. It concerns total mechanical energy. The Schur-complement storage $E_\perp$ in Chapter 4 is a different scalar: its derivative need not vanish after the carrier channel is reopened.

A.4 Conventions carried into the numerical chapters

The calculations use the following conventions throughout:

1. exact reduced return is imposed on $(\delta, v, \omega, \sigma)$, while (x, y, θ) is reconstructed afterward;
2. a full-cycle section at $\delta = 0$ includes a prescribed sign of σ;
3. $\bar{v} = T^{-1}\int_0^T v \, \mathrm{d}t$ is a branch observable, not a replacement for pose reconstruction;
4. the scalar theorem uses $q_y = v\omega$ only on a chart where the forward speed stays away from zero;
5. damping and joint torque are absent in Chapters 3 and 4; when introduced later, their power terms appear explicitly in the energy balance.

Appendix B

Scalar field, proof details, and numerical protocol

This appendix records the finite-speed equations and numerical gates used for the 29 exchange–return rows of Chapter 4. The metric derivative is retained in the exchange power and is not inserted into the integrated opened shape field.

B.1 Coefficient functions and opened field

For the dimensionless parameters introduced in Chapters 3–4, define

$$c_{\mathrm{geom}}(\delta) = \alpha + \mu\beta\cos\delta, \tag{B.1}$$

$$A_q(\delta) = \alpha j_2 + \alpha\beta^2\mu(1-\mu) - \mu\beta j_1\cos\delta, \tag{B.2}$$

$$r(\delta) = \frac{A_q(\delta)}{\Delta(\delta)}, \tag{B.3}$$

$$E_{\mathrm{geom}}(\delta) = B_{11}(\delta)\big(c_{\mathrm{geom}}(\delta) - \alpha\big) + \alpha\rho(\delta)^2. \tag{B.4}$$

With the scaled state

$$y = (\delta, \sigma, \nu, q_y), \qquad h = |\bar{v}|^{-1}, \qquad \nu = hv, \qquad q_y = v\omega, \tag{B.5}$$

the physical velocities are

$$v = \frac{\nu}{h}, \qquad \omega = \frac{hq_y}{\nu}. \tag{B.6}$$

The chart requires $h > 0$ and $\nu \neq 0$. The shape acceleration is

$$F_\sigma = \frac{r\{q_y - \rho(\sigma+\omega)^2\} - U'}{M_\perp}. \tag{B.7}$$

The two transport rows are evaluated in a fixed dependency order. First set

$$\lambda_{\mathrm{tr}} = \frac{c_{\mathrm{geom}}}{\Delta}\left(\nu - 2h\rho\sigma\right), \tag{B.8}$$

$$\phi_{\mathrm{tr}} = \nu\left[-\frac{B_{12}-\rho^2}{\Delta}F_\sigma + \frac{\rho c_{\mathrm{geom}}}{\Delta}\sigma^2\right], \tag{B.9}$$

$$R_{\mathrm{tr}} = \frac{\rho(B_{11}-B_{12})F_\sigma + E_{\mathrm{geom}}(2\omega\sigma+\sigma^2) + B_{11}c_{\mathrm{geom}}\omega^2}{\Delta}. \tag{B.10}$$

Then

$$F_q = \frac{\phi_{\mathrm{tr}} + h^2\nu^{-1}q_yR_{\mathrm{tr}} - \lambda_{\mathrm{tr}}q_y}{h}, \tag{B.11}$$

and

$$F_\nu = \frac{h\rho F_\sigma + h(c_{\mathrm{geom}} - \alpha)\sigma^2 + h^2\rho\nu^{-1}F_q + 2h^2(c_{\mathrm{geom}} - \alpha)\nu^{-1}q_y\sigma + h^3 c_{\mathrm{geom}}\nu^{-2}q_y^2}{1 + h^2\rho\nu^{-2}q_y}. \tag{B.12}$$

The denominator

$$D_{\mathrm{fs}} = 1 + h^2\rho\nu^{-2}q_y \tag{B.13}$$

is monitored along every returned orbit.

The exact scaled system is

$$\dot{y} = (\sigma, F_\sigma, F_\nu, F_q). \tag{B.14}$$

For $s = \mathrm{sgn}(\bar{v})$, the oriented variables

$$Y = (\delta, \zeta, u, Q), \qquad (\sigma, \nu, q_y) = (s\zeta, su, sQ) \tag{B.15}$$

and time change $\mathrm{d}/\,\mathrm{d}\vartheta = s\ \mathrm{d}/\,\mathrm{d}t$ give

$$\frac{\mathrm{d}Y}{\mathrm{d}\vartheta} = (\zeta, F_\sigma, F_\nu, F_q), \tag{B.16}$$

where the three field components on the right are evaluated at the signed scaled state. This is an exact conjugacy, not a large-speed approximation.

B.2 Exchange identity in the implemented convention

The conservative transverse field is

$$F_{\mathrm{cl}} = -\frac{U' + \frac{1}{2}M_\perp'\sigma^2}{M_\perp}, \tag{B.17}$$

whereas the opened field is Equation (B.7). Their difference is

$$M_\perp(F_\sigma - F_{\mathrm{cl}}) = r\{q_y - \rho(\sigma+\omega)^2\} + \frac{1}{2}M_\perp'\sigma^2. \tag{B.18}$$

Consequently,

$$P_{\mathrm{ex}} = \sigma M_\perp(F_\sigma - F_{\mathrm{cl}}) = \sigma\left[r\{q_y - \rho(\sigma+\omega)^2\} + \frac{1}{2}M_\perp'\sigma^2\right]. \tag{B.19}$$

Direct differentiation of

$$E_\perp = \frac{1}{2}M_\perp(\delta)\sigma^2 + U(\delta) \tag{B.20}$$

along the opened field gives

$$\frac{\mathrm{d}E_\perp}{\mathrm{d}t} = \sigma\left(M_\perp F_\sigma + U' + \frac{1}{2}M_\perp'\sigma^2\right) = P_{\mathrm{ex}}. \tag{B.21}$$

Under the oriented time transformation, the accumulator uses

$$\frac{\mathrm{d}I_{\mathrm{ex}}}{\mathrm{d}\vartheta} = sP_{\mathrm{ex}}, \tag{B.22}$$

so it integrates exchange along the physical-time traversal represented by the oriented orbit. For $s = +1$ this is the forward-period integral. For $s = -1$, increasing ϑ traverses physical time backward, and the result is the backward-period integral. Reversing a complete periodic traversal changes its sign but not its zero set; this is the only orientation-invariant fact used by the return theorem.

B.3 Event integration and nonlinear solve

For each requested $\bar{v}$, a regular closed-support cycle supplies a period scale and a section seed. The numerical unknowns are

$$p = (a, b, Q_0), \qquad Y_0(p) = (0, e^a, e^b, Q_0). \tag{B.23}$$

The integration state appends the exchange and speed accumulators,

$$\widehat{Y} = (Y, I_{\mathrm{ex}}, I_u), \qquad \frac{\mathrm{d}I_u}{\mathrm{d}\vartheta} = u. \tag{B.24}$$

After an initial dead interval equal to 5% of the support-period scale, event detection terminates at the next crossing $\delta = 0$ with positive direction. The packaged continuation producer defaults to DOP853, relative tolerance 2×10^{-9}, absolute tolerance 2×10^{-11}, and a maximum step equal to one support period divided by 500. The integration window extends to eight support periods. No command manifest records whether the archived 29-row run overrode those defaults, so these values document the available producer rather than an unrecorded historical command.

At return, the residual is

$$\mathcal{R}_{\mathrm{ex}} = \begin{bmatrix} I_{\mathrm{ex}}(T)/e_{\mathrm{sc}} \\ \{u(T) - u_0\}/u_{\mathrm{sc}} \\ \{Q(T) - Q_0\}/Q_{\mathrm{sc}} \\ I_u(T)/T - 1 \end{bmatrix}, \tag{B.25}$$

with

$$e_{\mathrm{sc}} = \max(1, |I_{\mathrm{ex}}|, |\Delta E_\perp|), \quad u_{\mathrm{sc}} = \max(1, |u_0|), \quad Q_{\mathrm{sc}} = \max(1, |Q_0|). \tag{B.26}$$

The four rows are retained for three free initial coordinates; the solve is therefore deliberately overdetermined and tests their simultaneous compatibility. The continuation driver permits at most 120 function evaluations and four initial starts. The nominal acceptance threshold is

$$\|\mathcal{R}_{\mathrm{ex}}\|_2 \le 10^{-8}. \tag{B.27}$$

The reported rows are substantially below that threshold.

B.4 Domain and evidence gates

A small algebraic residual is accepted only together with the following checks:

1. the next oriented event exists and has $\zeta > 0$;
2. u stays away from zero and D_{fs} stays away from zero;
3. $\Delta(\delta) > 0$ and $M_\perp(\delta) > 0$ along the orbit;
4. the integration remains finite and inside the declared regular corridor;
5. the returned orbit has the requested mean-speed gauge;
6. comparison with the independent continuation uses phase-invariant closed-loop geometry rather than pointwise time alignment.

The field implementation was checked against the raw four-dimensional model on nine states. The largest right-hand-side mismatch was

$$5.6843 \times 10^{-14}, \tag{B.28}$$

Table B.1: Independent re-integration and regular-domain checks for the 29 exchange–return rows. State defects compare the re-integrated terminal state with the archived initial state.

Quantity	Observed bound or range
successful intended returns	$29/29$
$\max\lvert\delta(T)\rvert$	4.84×10^{-15}
terminal ζ	$[7.31799,\ 7.99433]$
u over all trajectories	$[0.562472,\ 1.438482]$
D_{fs} over all trajectories	$[0.963830,\ 1.101637]$
$\max\lvert\delta\rvert$ over all trajectories	0.993057
$\min\Delta$ over all trajectories	1.43675
$\min M_\perp$ over all trajectories	0.0914364
maximum terminal-state defect	9.86×10^{-12}

and the largest raw–scaled coordinate round-trip error was

$$5.5511 \times 10^{-17}. \tag{B.29}$$

An independent directional-derivative audit of the exchange identity gave

$$\max\left|\frac{\mathrm{d}E_\perp}{\mathrm{d}t} - P_{\mathrm{ex}}\right| = 6.94 \times 10^{-10}. \tag{B.30}$$

The archived initial states were also re-integrated independently with a stricter DOP853 configuration. All 29 integrations reached the intended section. The finite margins in Table B.1 verify the chart and positivity assumptions on this computed corridor; they do not prove them on a larger domain.

The public family contains 29 comparison rows. Its aggregate metrics are

Quantity	Maximum over the 29 rows
scaled exchange-return residual	5.5074×10^{-12}
absolute reference-speed mismatch	7.3499×10^{-11}
absolute period error	1.4984×10^{-5}
absolute maximum-shape error	1.8554×10^{-5}
absolute maximum-yaw-rate error	8.3610×10^{-4}
phase-aligned scaled loop RMS	3.0698×10^{-3}

These numbers establish the local numerical realization used in Chapter 4. The accepted corridor is not an exhaustive annulus, a classification of physical designs, or a stability certificate.

Appendix C

Three-segment construction and population audit

This appendix records the population-level checks supporting Chapter 5. The audit starts from the stored AP and IP branch-chain summary and opens every referenced cycle file. It therefore checks the promoted population, rather than extrapolating from selected plots. The closed-support projection used earlier in the construction is not contained in those cycle files and is explicitly outside this re-audit.

C.1 Exact mechanical model

Let

$$e(\varphi) = \begin{bmatrix} \cos\varphi \\ \sin\varphi \end{bmatrix}, \qquad e^{\perp}(\varphi) = \begin{bmatrix} -\sin\varphi \\ \cos\varphi \end{bmatrix}. \tag{C.1}$$

The configuration is $q = (x, y, \theta, \delta_1, \delta_2)$, where $r_C = (x, y)^{\mathsf{T}}$ is the no-side-slip contact point. The constraint and an admissible velocity basis are

$$\begin{bmatrix} -\sin\theta & \cos\theta & 0 & 0 & 0 \end{bmatrix} \dot{q} = 0, \qquad \dot{q} = N(q)\xi, \qquad N(q) = \begin{bmatrix} \cos\theta & 0 & 0 & 0 \\ \sin\theta & 0 & 0 & 0 \\ 0 & 1 & 0 & 0 \\ 0 & 0 & 1 & 0 \\ 0 & 0 & 0 & 1 \end{bmatrix}, \tag{C.2}$$

with $\xi = (v, \omega, \sigma_1, \sigma_2)^{\mathsf{T}}$. Thus $\dot{x} = v\cos\theta$, $\dot{y} = v\sin\theta$, $\dot{\theta} = \omega$, and $\dot{\delta}_i = \sigma_i$.

Set $\ell_2 = L_2/2$ and $\ell_3 = L_3/2$. The three body centers are

$$\begin{aligned} r_1 &= r_C + l_1 e(\theta), \\ r_2 &= r_1 + \ell_2 e(\theta + \delta_1), \\ r_3 &= r_1 + L_2 e(\theta + \delta_1) + \ell_3 e(\theta + \delta_1 + \delta_2), \end{aligned} \tag{C.3}$$

and their velocities are

$$\begin{aligned} \dot{r}_1 &= v e(\theta) + l_1 \omega e^{\perp}(\theta), \\ \dot{r}_2 &= \dot{r}_1 + \ell_2(\omega + \sigma_1) e^{\perp}(\theta + \delta_1), \\ \dot{r}_3 &= \dot{r}_1 + L_2(\omega + \sigma_1) e^{\perp}(\theta + \delta_1) \\ &\quad + \ell_3(\omega + \sigma_1 + \sigma_2) e^{\perp}(\theta + \delta_1 + \delta_2). \end{aligned} \tag{C.4}$$

The corresponding angular rates are $\Omega_1 = \omega$, $\Omega_2 = \omega + \sigma_1$, and $\Omega_3 = \omega + \sigma_1 + \sigma_2$. The kinetic energy used in the calculation is exactly

$$\mathcal{T} = \frac{1}{2}\sum_{i=1}^{3} m_i \|\dot{r}_i\|^2 + \frac{1}{2}\sum_{i=1}^{3} I_i\Omega_i^2 = \frac{1}{2}\xi^\top M(\boldsymbol{\delta})\xi. \tag{C.5}$$

Together with

$$\begin{aligned} U(\boldsymbol{\delta}) = {} & \frac{1}{2}k_{2,1}\delta_1^2 + \frac{1}{4}k_{4,1}\delta_1^4 + \frac{1}{2}k_{2,2}\delta_2^2 + \frac{1}{4}k_{4,2}\delta_2^4 \\ & + \frac{1}{2}k_{12}(\delta_1 - \delta_2)^2, \end{aligned} \tag{C.6}$$

this defines the Lagrangian $L = \mathcal{T} - U$ without an implicit geometric convention. The projected Lagrange–d'Alembert equations are

$$N(q)^\top \left[\frac{\mathrm{d}}{\mathrm{d}t}\frac{\partial L}{\partial \dot{q}} - \frac{\partial L}{\partial q} - Q\right] = 0, \qquad Q = (0, 0, 0, u_1, u_2)^\top. \tag{C.7}$$

Equivalently,

$$M(\boldsymbol{\delta})\dot{\xi} + c(\boldsymbol{\delta}, \xi) + \begin{bmatrix} 0 \\ 0 \\ \partial_{\delta_1} U \\ \partial_{\delta_2} U \end{bmatrix} = \begin{bmatrix} 0 \\ 0 \\ u_1 \\ u_2 \end{bmatrix}. \tag{C.8}$$

For completeness, the velocity-dependent vector in Equation (C.8) can be written compactly by defining

$$m_\Sigma = m_1 + m_2 + m_3, \quad a = \ell_2 m_2 + L_2 m_3, \quad D_1 = \omega + \sigma_1, \quad D_2 = \omega + \sigma_1 + \sigma_2, \tag{C.9}$$

and $c_i = \cos\delta_i$, $s_i = \sin\delta_i$, $c_{12} = \cos(\delta_1 + \delta_2)$, and $s_{12} = \sin(\delta_1 + \delta_2)$. Its four components are

$$\begin{aligned} c_v = {} & -l_1 m_\Sigma \omega^2 - a c_1 D_1^2 - \ell_3 m_3 c_{12} D_2^2, \\ c_\omega = {} & \omega v(l_1 m_\Sigma + a c_1 + \ell_3 m_3 c_{12}) - l_1 a(2\omega\sigma_1 + \sigma_1^2)s_1 \\ & - L_2\ell_3 m_3(2\omega\sigma_2 + 2\sigma_1\sigma_2 + \sigma_2^2)s_2 \\ & - l_1\ell_3 m_3\left[2\omega(\sigma_1 + \sigma_2) + (\sigma_1 + \sigma_2)^2\right] s_{12}, \\ c_{\sigma_1} = {} & \omega v(a c_1 + \ell_3 m_3 c_{12}) + \omega^2(l_1 a s_1 + l_1\ell_3 m_3 s_{12}) \\ & - L_2\ell_3 m_3(2\omega\sigma_2 + 2\sigma_1\sigma_2 + \sigma_2^2)s_2, \\ c_{\sigma_2} = {} & \ell_3 m_3\left(L_2 D_1^2 s_2 + l_1\omega^2 s_{12} + \omega v c_{12}\right). \end{aligned} \tag{C.10}$$

In the state order used by the cycle files,

$$\dot{z} = \begin{bmatrix} \sigma_1 \\ \sigma_2 \\ M(\boldsymbol{\delta})^{-1}\left(\begin{bmatrix} 0 \\ 0 \\ u_1 \\ u_2 \end{bmatrix} - c(\boldsymbol{\delta}, \xi) - \begin{bmatrix} 0 \\ 0 \\ \partial_{\delta_1} U \\ \partial_{\delta_2} U \end{bmatrix}\right) \end{bmatrix}. \tag{C.11}$$

For the AP/IP population, $u_1 = u_2 = 0$, and the energy in Equations (C.5) and (C.6) is conserved by the exact field.

Table C.1: Numerical model-parameter vector shared by the AP and IP branch chains. The archive assigns no dimensional units to these coordinates.

Parameter	Value	Parameter	Value
m_1	6.0000000000	I_1	0.4186424184
m_2	0.3945707003	I_2	0.0060806994
m_3	0.2765544867	I_3	0.0003142956
l_1	0.2800000000	L_2	0.1500760073
L_3	0.1051882290	k_{12}	0.0011873112
$k_{2,1}$	0.6524353546	$k_{2,2}$	0.3008047507
$k_{4,1}$	5.2584240084	$k_{4,2}$	0.4491426471
u_1	0	u_2	0

C.2 One numerical model-parameter vector

All promoted AP and IP rows use the same parameter dictionary. The values are listed in Table C.1; comparison of every source summary against the IP reference dictionary produced no differing entry at the audit tolerance.

These values define the single numerical model-parameter vector used for the coexistence construction reported in Chapter 5.

The continuation equations admitted an auxiliary isotropic damping coordinate μ_{aux}, which is not part of p_*. Its largest absolute stored value is 2.68×10^{-12} on AP and 1.24×10^{-10} on IP. All reported raw-field defects are evaluated against the conservative field $\mu_{\text{aux}} = 0$; the stored cycles are finite-precision approximations to conservative relative-periodic solutions.

C.3 Modal coordinates and numerical construction

At p_*, the carrier-closed linear matrices are

$$\begin{aligned} M_0 &= \begin{bmatrix} 0.01806210949 & 0.002942788035 \\ 0.002942788035 & 0.001025996728 \end{bmatrix}, \\ K_0 &= \begin{bmatrix} 0.6536226658 & -0.001187311181 \\ -0.001187311181 & 0.3019920619 \end{bmatrix}. \end{aligned} \tag{C.12}$$

The mass-normalized modal vectors and frequencies are

$$u_{\text{IP}} = \begin{bmatrix} 6.99370047 & 2.65567809 \end{bmatrix}^{\mathsf{T}}, \qquad \Omega_{\text{IP}} = 5.835719714, \tag{C.13}$$

$$u_{\text{AP}} = \begin{bmatrix} 7.41765930 & -42.69238689 \end{bmatrix}^{\mathsf{T}}, \qquad \Omega_{\text{AP}} = 24.230934379. \tag{C.14}$$

Their signs define the local same-direction and opposite-direction choreographies. The large Euclidean entries result from normalization in the small effective-inertia metric.

Closed-support continuation starts from one of these two vectors and solves four-component transverse return together with a phase row and an amplitude coordinate. The support is lifted with the energy-minimizing carrier velocity in Equation (5.12). Multiple shooting limits accumulated endpoint error; Hermite–Simpson collocation supplies a local defect representation when the AP curve becomes strongly deformed. Pseudo-arclength continuation then follows the returned opened curves at fixed p_*, including through folds of a displayed coordinate.

The final interior field defect is not the collocation residual. A periodic cubic spline is fitted to the exported physical state, differentiated after trimming five percent of the samples at each end, and compared with the exact field in Equation (C.11). This is the value used by the population gate below.

C.4 Cycle qualification and modal identity

The branch-chain assembly retained a row only when two tests passed. First, the maximum interior raw-field defect had to satisfy

$$\epsilon_{\mathrm{rhs}} < 5 \times 10^{-3}. \tag{C.15}$$

Second, the sampled cycle had to remain in its declared modal sector. For $j \in \{\mathrm{IP}, \mathrm{AP}\}$, define

$$Q_j(t) = u_j^{\mathsf{T}} M_0 \boldsymbol{\delta}(t), \qquad \widetilde{P}_j(t) = \frac{u_j^{\mathsf{T}} M_0 \sigma(t)}{|\Omega_j|}, \tag{C.16}$$

$$A_j = \left[\frac{1}{T} \int_0^T \left(Q_j^2 + \widetilde{P}_j^2 \right) \, \mathrm{d}t \right]^{1/2}. \tag{C.17}$$

The expected-sector share and ratio are

$$S_j = \frac{A_j}{A_{\mathrm{IP}} + A_{\mathrm{AP}}}, \qquad R_j = \frac{A_j}{A_{j'}}, \quad j' \neq j. \tag{C.18}$$

For either position or rate signals $x(t), y(t)$, the reported correlation is the time-weighted Pearson coefficient

$$\mathrm{corr}_T(x, y) = \frac{\int_0^T (x - \bar{x})(y - \bar{y}) \, \mathrm{d}t}{\sqrt{\int_0^T (x - \bar{x})^2 \, \mathrm{d}t \int_0^T (y - \bar{y})^2 \, \mathrm{d}t}}, \qquad \bar{x} = \frac{1}{T} \int_0^T x \, \mathrm{d}t. \tag{C.19}$$

The IP gate requires both correlations to be at least 0.5, $S_{\mathrm{IP}} \geq 0.65$, and $R_{\mathrm{IP}} \geq 2$. The AP gate uses correlations at most -0.5, $S_{\mathrm{AP}} \geq 0.65$, and $R_{\mathrm{AP}} \geq 2$. Recalculation by trapezoidal time integration gives 2,278/2,278 AP passes and 1,358/1,358 IP passes. The ratio condition already implies a share of at least $2/3$, so the share row records the implemented gate rather than adding an independent restriction.

These tests classify the sampled modal content; they are not a proof that an entire invariant modal manifold exists. The linear parent vectors supply the coordinates, while the activity and correlation metrics are evaluated on the finite-amplitude cycles themselves.

C.5 Population audit

Each CSV file referenced by the branch summary is read independently. For a stored state sequence z_k at strictly increasing times t_k, the audit evaluates

$$\epsilon_{\mathrm{ret}} = \left\| z_N - z_0 \right\|_\infty, \tag{C.20}$$

$$\Delta\theta = \sum_{k=0}^{N-1} \frac{\omega_k + \omega_{k+1}}{2} (t_{k+1} - t_k), \tag{C.21}$$

$$\Delta x = \int_0^T v(t) \cos\theta(t) \, \mathrm{d}t, \qquad \Delta y = \int_0^T v(t) \sin\theta(t) \, \mathrm{d}t. \tag{C.22}$$

The trapezoidal pose reconstruction uses $\theta(0) = 0$; a different initial pose rigidly transforms the path but does not change whether the translation is zero. File existence, sample count, time monotonicity, endpoint return, and pose reconstruction, and time-weighted modal identity are recomputed. Cycle-mean exchange, transverse-energy drift, and interior raw-field defect are collected from the branch summary that generated the population.

The zero endpoint and stored-energy entries in Table C.2 mean equality at the precision written in the cycle files. They should not be interpreted as exact arithmetic statements. The raw-field defect is a sampled differentiation consistency metric, and its maximum remains below the historical 5×10^{-3} gate in both sectors.

Table C.2: Population audit over all branch-chain cycle files. Parenthetical labels distinguish recomputed quantities from stored branch diagnostics.

Quantity	AP	IP
cycle files	2,278	1,358
time samples	2,189,158	1,247,630
missing files	0	0
non-monotone time grids	0	0
maximum endpoint defect (recomputed)	0	0
time-weighted identity passes (recomputed)	2,278/2,278	1,358/1,358
minimum expected-sector share (recomputed)	0.69246	0.96335
minimum expected/opposite ratio (recomputed)	2.2516	26.2838
smallest required-sign correlation magnitude (recomputed)	0.99630	0.56425
maximum absolute cycle-mean exchange (stored)	1.692×10^{-8}	2.764×10^{-8}
maximum transverse-energy drift (stored)	0	0
maximum interior raw-field defect (stored)	1.102×10^{-3}	1.502×10^{-3}
minimum reconstructed displacement magnitude	3.038×10^{-3}	5.563×10^{-2}
maximum reconstructed displacement magnitude	79.923	143.562

Table C.3: Finite controls on activity, modal identity, period representation, and exchange-assisted construction.

Control	Observed signal	Missing property
large activity	AP-oriented internal activity reached 570.31	no moving AP branch; identity or raw-field quality could fail
modal identity	7/9 sector passes in the isolated-lever panel	0/9 moving branches
cycle representation	AP support remained numerically representable	ordinary one- and three-cover charts gave 0/4 moving trials each
exchange omitted from lift solve	one IP recipe gave ten moving identity-preserving points	raw-field mismatch $\simeq 1.04 \times 10^{-1}$; no moving AP pair

C.6 Finite construction controls

Four finite panels vary one ingredient of the construction. They do not survey all 3SEG parameter choices; they identify which shortcut failed within the recorded recipes.

Table C.3 separates internal excursion, modal choreography, numerical chart, raw-field consistency, and reconstructed displacement. Exchange is valuable during construction even though its cycle mean is a consequence of exact full return.

C.7 Observable convention and scope

The AP continuation stores the mean-speed observable in its active continuation coordinate. The corresponding field is inactive and constant in the IP export, so IP speed statements use the mean of $v(t)$ recomputed from each cycle file. Treating the inactive IP field as a physical speed would produce discrepancies as large as 161.1 in the model coordinates.

The population therefore combines

$$\begin{aligned}&\text{same numerical model parameters} \ \wedge\ \text{declared modal identity} \ \wedge\ \text{recomputed endpoint return}\\ &\quad \wedge\ \text{field consistency} \ \wedge\ \text{small exchange} \ \wedge\ \text{nonzero reconstructed displacement.}\end{aligned} \tag{C.23}$$

This is the finite numerical AP/IP coexistence statement used in Chapter 5. The closed-support association is not reconstructed for all 3,636 rows, and stability is not part of the audit.

Appendix D

Forced-response equations and reproduction protocol

This appendix documents the two forced calculations in Chapter 6. The first is the local same-mechanics homotopy from one conservative 2SEG cycle. The second is the independent, parameter-distinct response population containing 13,782 continued cycles in 25 forcing-amplitude groups. For the latter, reported peaks are observed samples and quadrature locations use only piecewise-linear interpolation between adjacent continued responses.

For all 13,782 archived cycles, the first and last stored samples agree exactly for δ, v, ω_b, σ, a, and b at exported precision. This is a check of the saved cycles, not a reconstruction of the collocation residual used by the original boundary-value solve.

D.1 Same-mechanics local bridge protocol

The bridge retains the mechanical parameters

$$\varepsilon = 0.681, \qquad \gamma = 2.504, \qquad k_2 = 1, \qquad k_4 = 10 \tag{D.1}$$

of Chapter 3. Only the declared viscous and input terms are added:

$$\mu_{\mathrm{visc}}(\lambda) = \lambda c_\star, \qquad u(t;\lambda) = \lambda A_\star \sin\left(\frac{2\pi t}{T_\lambda} + \phi_\lambda\right), \qquad c_\star = 10^{-3}. \tag{D.2}$$

On the repolished conservative anchor, the first-order forcing amplitude that can balance isotropic viscous loss is 0.03376316109. The computation uses a 10% margin,

$$A_\star = 0.03713947719, \tag{D.3}$$

and selects the lower of the two work-balancing phase branches. At $\lambda = 0$ the input vanishes, so its physical phase is undefined.

Time zero is fixed by $\delta(0) = 0$, $\sigma(0) > 0$. For every positive λ, the unknowns are $(v_0, \omega_0, \sigma_0, T_\lambda, \phi_\lambda)$; the equations are the four synchronized reduced-return rows and the fixed time-weighted mean-speed row $\bar{v} = 10.435810958679$. The drive frequency $2\pi/T_\lambda$ therefore changes with the corrected response. Nineteen prescribed homotopy values are used:

$$\lambda \in \{0, 10^{-4}, 3\times10^{-4}, 10^{-3}, 3\times10^{-3}, 5\times10^{-3}, 10^{-2}, 3\times10^{-2}, 0.06, 0.1, 0.2, \ldots, 1\}. \tag{D.4}$$

Every declared point was reached. The maximum strict reduced-return residual is 7.102×10^{-10}, the maximum mean-speed error is 1.075×10^{-12}, and the maximum absolute defect in the differential energy identity is 4.112×10^{-13}. The largest relative cycle work imbalance is 2.940×10^{-4} at

$\lambda = 10^{-4}$, where both work terms are approximately 10^{-5}; at $\lambda = 1$ the relative imbalance is 2.60×10^{-11}. Meshes from 501 to 4001 points and three independent integration tolerances were compared. The largest strict–ultra endpoint difference is 5.405×10^{-14}.

The normalized waveform distance compares phase-aligned $(\delta, v, \omega, \sigma)$ traces after scaling each coordinate by an anchor amplitude. It is 4.658×10^{-5} at $\lambda = 10^{-4}$ and 0.28708 at $\lambda = 1$. This establishes numerical approach to the conservative anchor along the computed branch. It is not a whole-family persistence, uniqueness, or stability result. The full row-level branch, waveform, mesh, and tolerance tables are generated by the Gate-B reproduction script recorded with the V3 evidence package.

D.2 Parameter-distinct archive: exact reduced field and sign convention

Let $\eta_f = (v, \omega_b, \sigma)^{\mathsf{T}}$. The response computation uses

$$M_f(\delta) = \begin{bmatrix} 1 & -(\varepsilon_f - 1)^2 \sin\delta & -(\varepsilon_f - 1)^2 \sin\delta \\ -(\varepsilon_f - 1)^2 \sin\delta & M_{22} & M_{23} \\ -(\varepsilon_f - 1)^2 \sin\delta & M_{23} & M_{33} \end{bmatrix}, \tag{D.5}$$

where

$$\begin{aligned} M_{22} &= \varepsilon_f^3 \gamma_f + \varepsilon_f^3 - \gamma_f(\varepsilon_f - 1)^3 \\ &\quad + (1 - \varepsilon_f)\left[-2\varepsilon_f^2 \cos\delta + 2\varepsilon_f^2 + 2\varepsilon_f \cos\delta - 2\varepsilon_f + 1\right], && \text{(D.6)} \\ M_{23} &= (\varepsilon_f - 1)^2 \left[-\varepsilon_f \gamma_f + \varepsilon_f \cos\delta - \varepsilon_f + \gamma_f + 1\right], && \text{(D.7)} \\ M_{33} &= -(\varepsilon_f - 1)^3 (\gamma_f + 1). && \text{(D.8)} \end{aligned}$$

The continued data use $\varepsilon_f = 0.7317084397592031$ and $\gamma_f = 0.736801492464307$. A numerical minimization over one full period, $\delta \in [-\pi, \pi]$, gives minimum eigenvalue 0.02561150819; the matrix is therefore uniformly positive in the tested interval to the reported numerical precision.

The code evaluates the acceleration in right-hand-side form,

$$M_f(\delta)\dot{\eta}_f = b_f(\delta, \eta_f) + B_\delta \tau_\delta - c_d \eta_f, \qquad B_\delta = \begin{bmatrix} 0 & 0 & 1 \end{bmatrix}^{\mathsf{T}}, \tag{D.9}$$

with

$$b_f = \begin{bmatrix} \varepsilon_f \omega_b^2 + (1 - \varepsilon_f)^2 (\sigma + \omega_b)^2 \cos\delta \\ \varepsilon_f (1 - \varepsilon_f)^2 (\sigma + 2\omega_b)\sigma \sin\delta - \omega_b v \left[\varepsilon_f + (1 - \varepsilon_f)^2 \cos\delta\right] \\ -\varepsilon_f (1 - \varepsilon_f)^2 \omega_b^2 \sin\delta - (1 - \varepsilon_f)^2 \omega_b v \cos\delta - 2\delta \end{bmatrix}. \tag{D.10}$$

Thus the left-hand-side convention of Equation (6.8) is exact when

$$F_f = -b_f, \qquad D_f = c_d I_3. \tag{D.11}$$

In particular, the third component of F_f ends in $+2\delta$. The factor two follows from the implemented potential $V_f(\delta) = \delta^2$, for which the spring torque is -2δ. Writing the vector b_f on the left with a plus sign would reverse every conservative acceleration term and is not the implemented model.

The autonomous forcing lift is

$$\dot{a} = -\Omega b + a(1 - a^2 - b^2), \qquad \dot{b} = \Omega a + b(1 - a^2 - b^2), \qquad \tau_\delta = A_{\mathrm{exc}} b. \tag{D.12}$$

On $a^2 + b^2 = 1$, the last expression is a unit-amplitude sinusoid scaled by A_{exc}. The implementation uses $A_{\mathrm{exc}} b$ directly; it does not divide by $\sqrt{a^2 + b^2}$.

All variables in this computation are nondimensional. For reference mass M_0, length l_0, and the coefficient k_0 in the dimensional potential $V = k_0 \delta^2$, the time scale and torque-amplitude conversion are

$$t_c = \sqrt{\frac{M_0 l_0^2}{k_0}}, \qquad A_{\mathrm{exc}} = \frac{\tau_{\mathrm{amp}} t_c^2}{M_0 l_0^2} = \frac{\tau_{\mathrm{amp}}}{k_0}. \tag{D.13}$$

Consequently, $\tau_{\mathrm{amp}} = k_0 A_{\mathrm{exc}}$. The numerical group labels used in the response plots equal $1000 A_{\mathrm{exc}}$ rounded to two decimals; they are equivalent N mm values only for $k_0 = 1\,\mathrm{N\,m}$.

D.3 Offline phase convention

The response map stores the phase of joint deformation relative to applied joint torque. The exported AUTO mesh is not uniform in time. Each cycle is first interpolated periodically onto 1,000 uniformly spaced times in $[0, T)$; the duplicated endpoint is excluded. For a resampled signal y, the extractor removes its mean and forms the analytic signal

$$a_y(t) = y(t) - \langle y \rangle + \mathrm{i}\,\mathcal{H}[y - \langle y \rangle](t), \tag{D.14}$$

where $\mathcal{H}$ denotes the discrete Hilbert transform. The cycle phase is

$$\phi_{\delta\tau} = \mathrm{Arg}\left[\frac{1}{N}\sum_{k=1}^{N} \exp\bigl\{\mathrm{i}\bigl(\arg a_\delta(t_k) - \arg a_\tau(t_k)\bigr)\bigr\}\right]. \tag{D.15}$$

Thus the signal order is output minus input, the wrap interval is $[-\pi, \pi)$, and quadrature is $\phi_{\delta\tau} = -\pi/2$. This is a Hilbert analytic-signal statistic. A Fourier-coefficient phase can approximate it on a nearly harmonic response, but the two definitions are not identical on a distorted waveform.

D.4 Observed peak and linear crossing

For each amplitude group r, let

$$v_{\mathrm{pk},rj} = \max_k v_{rj}(t_k), \qquad j_{p,r} \in \arg\max_j v_{\mathrm{pk},rj}, \qquad (T_{p,r}, v_{p,r}) = (T_{rj_{p,r}}, v_{\mathrm{pk},rj_{p,r}}) \tag{D.16}$$

where k indexes the exported within-cycle samples and j follows continuation order. Thus the stated peak is a sampled positive maximum, not a spline estimate between nodes. A quadrature crossing is accepted only when two consecutive responses bracket $-\pi/2$. If

$$d_j = \phi_{rj} + \frac{\pi}{2}, \qquad d_j d_{j+1} < 0, \tag{D.17}$$

the interpolation fraction and crossing speed are

$$\lambda_j = \frac{|d_j|}{|d_j| + |d_{j+1}|}, \tag{D.18}$$

$$T_{q,r} = (1 - \lambda_j) T_{rj} + \lambda_j T_{r,j+1}, \tag{D.19}$$

$$v_{q,r} = (1 - \lambda_j) v_{\mathrm{pk},rj} + \lambda_j v_{\mathrm{pk},r,j+1}. \tag{D.20}$$

When several crossings occur, the first in continuation order is used. No crossing is inferred when the target is absent.

Table D.1: Transparent quadrature audit by response-map region.

Groups	Crossing status	Relation to the observed speed peak
ranks 1–15	all 15 cross $-\pi/2$	maximum linearly interpolated speed gap 0.0635625%; maximum period gap 0.0289515%
ranks 16–20	all five cross	crossing belongs to a much slower part of the continued response, 59.19–71.84% below the observed peak
ranks 21–25	no sampled crossing	nearest available sample is not promoted as an exact quadrature point

The reported proximity metric is

$$\epsilon_{v,r} = 100\frac{|v_{q,r} - v_{p,r}|}{|v_{p,r}|}, \tag{D.21}$$

with the corresponding period gap defined analogously. Both numerical values are reported in percent.

As summarized in Table D.1, the compact statement in the main text rounds the rank-1–15 bound upward to 0.064%. The largest phase error evaluated at an observed speed peak on those ranks is 0.0452127 rad. Near-equality of peak speed and quadrature speed is therefore a local property of the rising branch, not a property of all 25 forcing groups.

D.5 Amplitude-dependent period

At $\delta = v = \omega_b = \sigma = 0$, the effective shape inertia after eliminating the yaw coordinate is

$$M_{\text{lin}} = M_{33}(0) - \frac{M_{23}(0)^2}{M_{22}(0)} = 0.0258224048916. \tag{D.22}$$

Since the linear restoring coefficient is 2,

$$T_{\text{lin}} = 2\pi\sqrt{M_{\text{lin}}/2} = 0.7139424640185. \tag{D.23}$$

The nearby value 0.7139425323 stored in the earlier response analysis is the period of a finite seed cycle, not the result of this linearization. At the observed speed maximum of rank 15, $T_{p,15} = 0.7410295954$, giving

$$100\frac{T_{p,15} - T_{\text{lin}}}{T_{\text{lin}}} = 3.7940\%. \tag{D.24}$$

At rank 25 the observed peak period is 0.7411539715, a 3.8114% shift. The period shift depends only on the archived periods and the mechanical linearization; it is independent of the Hilbert-phase and THD extraction rules.

D.6 Scope

The response population supports the model-specific map and local quadrature statement above. Uniqueness, global stability, and experimental robustness remain separate questions.

Appendix E

Harmonic estimators and tracking tests

This appendix records the estimator, supervisory thresholds, and numerical checks used in Chapter 7. It separates termination of the implemented experiment from successful arrival: the supervisor has finite trial and step limits, but the available data do not prove that an arbitrary rejected trial will recover before those limits are reached.

E.1 Windowed harmonic estimator

For samples y_i recorded at excitation phases φ_i, define the design matrix

$$X_{K_{\text{est}}} = \begin{bmatrix} 1 & \sin\varphi_1 & \cos\varphi_1 & \cdots & \sin K_{\text{est}}\varphi_1 & \cos K_{\text{est}}\varphi_1 \\ \vdots & \vdots & \vdots & & \vdots & \vdots \\ 1 & \sin\varphi_N & \cos\varphi_N & \cdots & \sin K_{\text{est}}\varphi_N & \cos K_{\text{est}}\varphi_N \end{bmatrix}. \tag{E.1}$$

The implementation obtains

$$\widehat{\beta}_y = X^{\dagger}_{K_{\text{est}}}\boldsymbol{y} = \begin{bmatrix} \widehat{c}_{y,0} & \widehat{a}_{y,1} & \widehat{b}_{y,1} & \cdots \end{bmatrix}^{\mathsf{T}}, \tag{E.2}$$

using a linear least-squares solve. The dagger notation emphasizes that the numerical routine uses a stable least-squares solution rather than explicitly forming $(X^{\mathsf{T}}_{K_{\text{est}}} X_{K_{\text{est}}})^{-1}$. The tracking calculation uses $K_{\text{est}} = 3$. The phase passed to feedback is

$$\phi_y = \operatorname{atan2}(\widehat{b}_{y,1}, \widehat{a}_{y,1}), \qquad e_\phi = \operatorname{wrap}_{[-\pi,\pi)}\left(\phi_\delta - \phi_\tau + \frac{\pi}{2}\right). \tag{E.3}$$

Thus the convention is response phase minus torque phase, with the target $-\pi/2$. A phase computed from a Hilbert transform with an unstated reference or from input minus output would require a different controller sign.

The estimator is well conditioned only when the window covers the excitation phase adequately and the fitted fundamental amplitude is nonzero. Higher harmonics absorb waveform distortion, but only the fundamental pair enters Equation (E.3).

E.2 Local sign tests

The rank-10 tests compare the implemented sign with the opposite sign under the same -0.5% frequency detuning. The correct sign reduced the final-tail phase-error RMS from 1.2386 to 2.391×10^{-3} rad and returned the mean frequency from 8.7002 to 8.7431, near the 8.7439 reference. The opposite sign left a phase-error RMS of 1.2452 rad and moved the mean frequency to

Table E.1: Recorded guarded-traversal outcomes.

Quantity	Start from rest	Start from rank 1
proposed stages	21	21
accepted / rejected	21/0	21/0
terminal mean speed	12.0680391251	12.0677941731
terminal phase-error RMS [rad]	$1.11897244 \times 10^{-3}$	$1.10605507 \times 10^{-3}$
terminal a-posteriori rank	15	15
online use of response map	none	none

7.6425. Additional correct-sign starts at $+0.5\%$ and -3% detuning ended with phase-error RMS 2.679×10^{-3} and 4.103×10^{-3} rad, respectively.

These tests establish the sign and local locking behavior around one operating point. They do not map the acquisition basin. A separate amplitude staircase obtained phase lock in all 15 runs but selected the low branch in all 15 and never acquired the requested target ranks. This negative control is why phase is used as a resonance coordinate but not as the locomotor branch coordinate.

E.3 Supervisor and finite execution

Each stage is simulated for 150 model-time units with sample interval 0.006. The default phase and slow speed gains are

$$K_P = 0.04, \qquad K_I = 0.08, \qquad K_v = 2.5 \times 10^{-5}. \tag{E.4}$$

A proposal is accepted when

$$\mathrm{RMS}(e_\phi) \le 0.12, \tag{E.5}$$

$$\mathrm{ptp}(\delta) \le 8.5, \tag{E.6}$$

$$|\langle\omega\rangle| \le 0.08, \tag{E.7}$$

$$\bar{v}_{\text{new}} \ge \bar{v}_{\text{old}} - \max(0.75, 0.12|\bar{v}_{\text{old}}|), \tag{E.8}$$

and, for requested speeds at least 8,

$$|\bar{v}_{\text{new}} - \bar{v}_{\text{des}}| \le \max(0.65, 0.14|\bar{v}_{\text{des}}|). \tag{E.9}$$

The high-speed proposed step is capped at 0.25. A rejected proposal halves the next step. The run stops if the step falls below 0.125 or after 40 attempts per initial condition.

These caps make each execution finite. They also permit failure before the target is reached. No rejection occurred in the reported campaign, so the halving and recovery path was not exercised.

Across the 42 accepted stages reported in Table E.1, the maximum phase-error RMS was 2.7012×10^{-3} rad, the maximum deformation peak-to-peak was 3.5383, and the maximum absolute mean yaw rate was 4.5720×10^{-3}. The smallest recorded margins to the five acceptance boundaries were positive. This shows that the nominal schedule stayed well inside the monitored thresholds; it does not show that the thresholds caused a recovery.

E.4 Sampled harmonic linearizations

For each reference response, the full reduced state is represented by $K_{\mathrm{G}} = 5$ harmonics,

$$z(\varphi) = \bar{z} + \sum_{k=1}^{K_{\mathrm{G}}} \big[a_k \sin(k\varphi) + b_k \cos(k\varphi)\big]. \tag{E.10}$$

With four state components, the response chart has $4(1 + 2K_{\mathrm{G}}) = 44$ coordinates. Finite-difference Galerkin linearization gives a response matrix A_G, a frequency-input vector p_G, an amplitude-input vector q_G, and phase and speed rows c_G, c_v. Appending the filtered phase, phase integral, and slow amplitude state produces the two closed matrices tested in Chapter 7.

For ranks 1–14, every stored $K_{\mathrm{G}} = 5$ linearization has negative spectral abscissa with the declared gains. The phase-only closed values range from -1.81848×10^{-3} to -1.00100×10^{-3}; after adding the speed loop they range from -8.93731×10^{-4} to -2.95865×10^{-4}. Rank 15 is not part of this table.

The check is finite-dimensional and sampled. The discarded-harmonic error, normal hyperbolicity, and nonlinear basin sizes are not bounded. The largest stored projected-residual RMS is 2.44015×10^{-2}, while the smallest speed-loop spectral margin is 2.95865×10^{-4}; no perturbation estimate relates those quantities. Negative eigenvalues of the 14 reduced matrices therefore support local controller design but do not prove stability of the exact nonlinear forced system.

E.5 Conditions missing from a finite-arrival theorem

A general guarded-arrival result would require, at minimum, an initial set inside a verified branch tube; a uniform bound guaranteeing that all sufficiently small trials settle and pass the guard; a positive minimum accepted progress step; and uniform guard margins and contraction bounds. The rank interval would also need to stop at 14 unless a separate stability argument were provided at rank 15. None of these uniform conditions is established by the present files.

Accordingly, the supported result is a finite numerical traversal from two named starts plus sampled reduced-order local stability. Guard recovery, global acquisition, arbitrary-target tracking, and general finite arrival remain open.

Bibliography

Gaëtan Abeloos, Felix Müller, Emre Ferhatoglu, Matthias Scheel, Christophe Collette, Gaëtan Kerschen, Matthew R. W. Brake, Paolo Tiso, Ludovic Renson, and Malte Krack. A consistency analysis of phase-locked-loop testing and control-based continuation for a geometrically nonlinear frictional system. *Mechanical Systems and Signal Processing*, 170:108820, 2022. doi: 10.1016/j.ymssp.2022.108820.

Vladimir I. Arnold. *Mathematical Methods of Classical Mechanics*. Springer, 2 edition, 1989. doi: 10.1007/978-1-4757-2063-1.

David A. W. Barton. Control-based continuation: Bifurcation and stability analysis for physical experiments. *Mechanical Systems and Signal Processing*, 84:54–64, 2017. doi: 10.1016/j.ymssp.2015.12.039.

Anthony M. Bloch. *Nonholonomic Mechanics and Control*. Springer, 2 edition, 2015. doi: 10.1007/978-1-4939-3017-3.

Davide Calzolari, Cosimo Della Santina, and Alin Albu-Schäffer. Exciting families of passive gaits in an elastic quadruped via natural motion manifold control. *The International Journal of Robotics Research*, page 02783649251347305, 2025. doi: 10.1177/02783649251347305.

Mattia Cenedese and George Haller. How do conservative backbone curves perturb into forced responses? a Melnikov function analysis. *Proceedings of the Royal Society A*, 476(2234):20190494, 2020a. doi: 10.1098/rspa.2019.0494.

Mattia Cenedese and George Haller. Stability of forced–damped response in mechanical systems from a Melnikov analysis. *Chaos*, 30(8):083103, 2020b. doi: 10.1063/5.0012480.

Vincent Denis, Marc Jossic, Christophe Giraud-Audine, Benoît Chomette, Alexandre Renault, and Olivier Thomas. Identification of nonlinear modes using phase-locked-loop experimental continuation and normal form. *Mechanical Systems and Signal Processing*, 106:430–452, 2018. doi: 10.1016/j.ymssp.2018.01.014.

Jaap Eldering and Henry O. Jacobs. The role of symmetry and dissipation in biolocomotion. *SIAM Journal on Applied Dynamical Systems*, 15(1):24–59, 2016. doi: 10.1137/140970914.

Francesco Fasso, Simone Passarella, and Marta Zoppello. Control of locomotion systems and dynamics in relative periodic orbits. *Journal of Geometric Mechanics*, 12(3):395–420, 2020. doi: 10.3934/jgm.2020022.

Zhenyu Gan, Yevgeniy Yesilevskiy, Petr Zaytsev, and C. David Remy. All common bipedal gaits emerge from a single passive model. *Journal of the Royal Society Interface*, 15(146):20180455, 2018. doi: 10.1098/rsif.2018.0455.

George Haller and Sten Ponsioen. Nonlinear normal modes and spectral submanifolds: Existence, uniqueness and use in model reduction. *Nonlinear Dynamics*, 86(3):1493–1534, 2016. doi: 10.1007/s11071-016-2974-z.

Scott D. Kelly and Richard M. Murray. Geometric phases and robotic locomotion. *Journal of Robotic Systems*, 12(6):417–431, 1995. doi: 10.1002/rob.4620120607.

Gaëtan Kerschen, Maxime Peeters, Jean-Claude Golinval, and Alexander F. Vakakis. Nonlinear normal modes, part i: A useful framework for the structural dynamicist. *Mechanical Systems and Signal Processing*, 23(1):170–194, 2009. doi: 10.1016/j.ymssp.2008.04.002.

Robert J. Kuether, Ludovic Renson, Thibaut Detroux, Chiara Grappasonni, Gaëtan Kerschen, and Matthew S. Allen. Nonlinear normal modes, modal interactions and isolated resonance curves. *Journal of Sound and Vibration*, 351:299–310, 2015. doi: 10.1016/j.jsv.2015.04.035.

Yuri A. Kuznetsov. *Elements of Applied Bifurcation Theory.* Springer, 3 edition, 2004. doi: 10.1007/978-1-4757-3978-7.

Mirado Mortel, Luc Jaulin, Lionel Lapierre, and Simon Rohou. Natural locomotion: Principle and method, 2026.

Jim P. Ostrowski and Joel W. Burdick. The geometric mechanics of undulatory robotic locomotion. *The International Journal of Robotics Research*, 17(7):683–701, 1998. doi: 10.1177/027836499801700701.

Maxime Peeters, Régis Viguié, Guillaume Sérandour, Gaëtan Kerschen, and Jean-Claude Golinval. Nonlinear normal modes, part ii: Toward a practical computation using numerical continuation techniques. *Mechanical Systems and Signal Processing*, 23(1):195–216, 2009. doi: 10.1016/j.ymssp.2008.04.003.

Maxime Peeters, Gaëtan Kerschen, and Jean-Claude Golinval. Dynamic testing of nonlinear vibrating structures using nonlinear normal modes. *Journal of Sound and Vibration*, 330(3):486–509, 2011. doi: 10.1016/j.jsv.2010.08.028.

Simon Peter and Remco I. Leine. Excitation power quantities in phase resonance testing of nonlinear systems with phase-locked-loop excitation. *Mechanical Systems and Signal Processing*, 96:139–158, 2017. doi: 10.1016/j.ymssp.2017.04.011.

Simon Peter, Robin Riethmüller, and Remco I. Leine. Tracking of backbone curves of nonlinear systems using phase-locked-loops. In *Nonlinear Dynamics, Volume 1*, pages 107–120. Springer, 2016. doi: 10.1007/978-3-319-29739-2_11.

Maximilian Raff, Nelson Rosa, and C. David Remy. Connecting gaits in energetically conservative legged systems. *IEEE Robotics and Automation Letters*, 7(3):8407–8414, 2022. doi: 10.1109/LRA.2022.3186500.

Mirado Rajaomarosata, Luc Jaulin, Lionel Lapierre, and Simon Rohou. Natural efficient gaits from nonholonomic locomotion nonlinear normal mode (NL-NNM): The pendrivencar case. *Mechatronics*, 110:103366, 2025a. doi: 10.1016/j.mechatronics.2025.103366.

Mirado Rajaomarosata, Luc Jaulin, Lionel Lapierre, and Simon Rohou. Energy-efficient nonholonomic fish robot: Nonlinear forced oscillations. In *OCEANS 2025 Brest*, pages 1–7. IEEE, 2025b. doi: 10.1109/OCEANS58557.2025.11104676.

C. David Remy. *Optimal Exploitation of Natural Dynamics in Legged Locomotion.* PhD thesis, ETH Zurich, 2011.

Ludovic Renson, Alicia Gonzalez-Buelga, David A. W. Barton, and Simon A. Neild. Robust identification of backbone curves using control-based continuation. *Journal of Sound and Vibration*, 367:145–158, 2016. doi: 10.1016/j.jsv.2015.12.035.

Robert M. Rosenberg. On nonlinear vibrations of systems with many degrees of freedom. In *Advances in Applied Mechanics*, volume 9, pages 155–242. Elsevier, 1966. doi: 10.1016/S0065-2156(08)70008-5.

Steven W. Shaw and Christophe Pierre. Normal modes for non-linear vibratory systems. *Journal of Sound and Vibration*, 164(1):85–124, 1993. doi: 10.1006/jsvi.1993.1198.

Min Tang, Christian Stéphan, and Marc Böswald. Phase resonance method for nonlinear mechanical structures with phase locked loop control. In *Proceedings of ISMA 2020*, pages 1805–1818, 2020.